Aplicacions del CPTU en Geociències Marines: estudi de casos de la Mediterrània

Sara Lafuerza Colas

Universitat de Barcelona
Departament d'Estratigrafia, Paleontologia i Geociències Marines

Aplicacions del CPTU en Geociències Marines: estudi de casos de la Mediterrània

Memòria de Tesi Doctoral realitzada per
Sara Lafuerza

Sota la direcció del
Dr. Miquel Canals i Artigas

Barcelona, Novembre del 2009

La doctoranda, El director,

Sara Lafuerza Miquel Canals

CAPÍTOL 5

RESULTATS

5.1. Characterization of deltaic sediment bodies based on in situ CPT/CPTU profiles: A case study on the Llobregat delta plain, Barcelona, Spain

S. Lafuerza (1), M. Canals (1), J-L. Casamor (1), J-M. Devincenzi (2)

(1) GRC Geociències Marines, Departament d'Estratigrafia, Paleontologia i Geociències Marines, Universitat de Barcelona, Spain
(2) IGEOTEST, Spain

Abstract

This article describes a preliminary study on the Llobregat delta, Spain, which includes the construction of a 3D model from cone penetration tests (CPT) and piezocone tests (CPTU) in order to establish the architectural stacking pattern of deltaic sediment bodies. The sediment facies identified from boreholes have been characterized by using their mechanical behaviour and have been used to identify the depositional sequence of the Llobregat delta.

Within the general architectural frame, flood plain silts and silty sands, crevasse sands, fluvial channel sands, sand ridges, delta front silts and clays, and prodelta silts and clays have been characterized as a function of cone tip resistance (q_c) and sleeve friction (f_s). From the sediment facies characterization, a depositional sequence constituted by three systems tracts is proposed. The sequence is divided into: a lowstand systems tract (LST) represented by fluvial gravels, a transgressive systems tract (TST) constituted by a fining-upward sequence with a thin sand sheet below silts and clays, and the highstand systems tract (HST) represented by three prograding wedges displaying coarsening-upward sequences.

We emphasize the simplicity, speed, high spatial resolution and low cost of CPT/CPTU grids as a new tool enabling us to reconstruct the three-dimensional structure of deltaic environments for sedimentological and stratigraphical purposes.

Keywords: cone penetration test, piezocone test, 3D geometry, sequence stratigraphy, delta facies, Llobregat delta

2005, Marine Geology, Vol. 222-223, p. 497-510.
Doi: 10.1016/j.margeo.2005.06.043

5.1.1. Introduction

Most of the modern deltas throughout the Mediterranean Sea developed as a response to the deceleration in post-glacial sea level rise during the Holocene. In terms of sequence stratigraphy, the majority of Mediterranean deltas contain: (i) a basal sequence, namely the lowstand systems tract (LST), constituted by late Pleistocene fluvial deposits, (ii) a transgressive systems tract (TST), made of shallow marine transgressive early Holocene deposits, and (iii) an overlying highstand systems tract (HST), resulting from the accumulation of Holocene deltaic aggradational to progradational deposits (Stanley and Warne, 1994). The internal structure of HST deltaic deposits has been related to high frequency (fifth- and six-order) sea level oscillations (Somoza et al., 1998; Ridente and Trincardi, 2002; Fernández -Salas, 2003).

Deltas represent an historical record of environmental changes since they are subject to continuous physical changes (river migration, floods, regressions-transgressions and subsidence) at different time-scales. On a millennial scale, the effects of climatic changes modify deltas by ice cap contraction and expansion controlling the sediment supply. On a centennial to decadal scale, human activities have generated shifts in the balance between coastal sedimentation and erosion by changes in land use and/or flooding frequency because of river damming and regulation. Deltas can be considered as quite unstable sedimentary systems so humans, who are increasingly exploiting and altering them, remain vulnerable to these physical changes. Therefore, to implement potentially successful plans and protection strategies, understanding the architecture of deltas and the factors involved on their formation becomes essential.

Cone penetration (CPT) and piezocone (CPTU) tests are widely used in geotechnical subsuperficial studies because of their excellent potential for in situ continuous vertical profiling in non-cemented soils at fast rate and low cost. Piezocones are CPT cones that incorporate a pore pressure element thus allowing us to perform the so-called CPTU tests. Both types of tests are used to measure the mechanical behaviour of soils and estimate physical properties such as soil density, overconsolidation ratio and in situ horizontal stress, amongst others. CPT tests provide accurate data, most often yielding one measurement or "signal" per cm of downhole penetration. CPT/CPTU tests provide high resolution estimates of grain size vertical variations in a way that the resulting logs can be directly compared with sedimentary successions in terms of coarsening and thickening sequences and cyclicities (Moran et al., 1989). This allows characterizing sedimentological trends and sequence boundaries, both aspects highly relevant to sedimentology and sequence stratigraphy as shown by Campanella et al. (1983), Moran et al. (1989), Robertson (1990), Robertson et al. (1996), Amorosi and Marchi (1999) and Devincenzi et al. (2003). In addition, distributed grids of CPT/CPTU profiles allow the 3D reconstruction of the geometry of sediment bodies. Finally, boreholes are essential for groundtruthing purposes.

In this paper, we aim to demonstrate the utility of CPT/CPTU data to the study of the sedimentology and stratigraphy of Holocene deltas, applied to the Llobregat delta, in the NE section of the Iberian Peninsula. Scattered CPT/CPTU data have been transformed into a regularly spaced three-dimensional grid depicting the geometry of sediment bodies constituting the Llobregat delta.

5.1.2. Regional setting

The study area covers 1.43 x 3.3 km on the right bank of the Llobregat river delta plain, nearby the city of Barcelona (Fig. 5.1.1). The subaqueous part of Llobregat delta lies on an 8 km wide, 0.3º to 0.7º slope continental shelf, the southern edge of which is incised by the Foix Canyon. The delta plain spreads over 95 km^2 with 23 km of shoreline length. North-

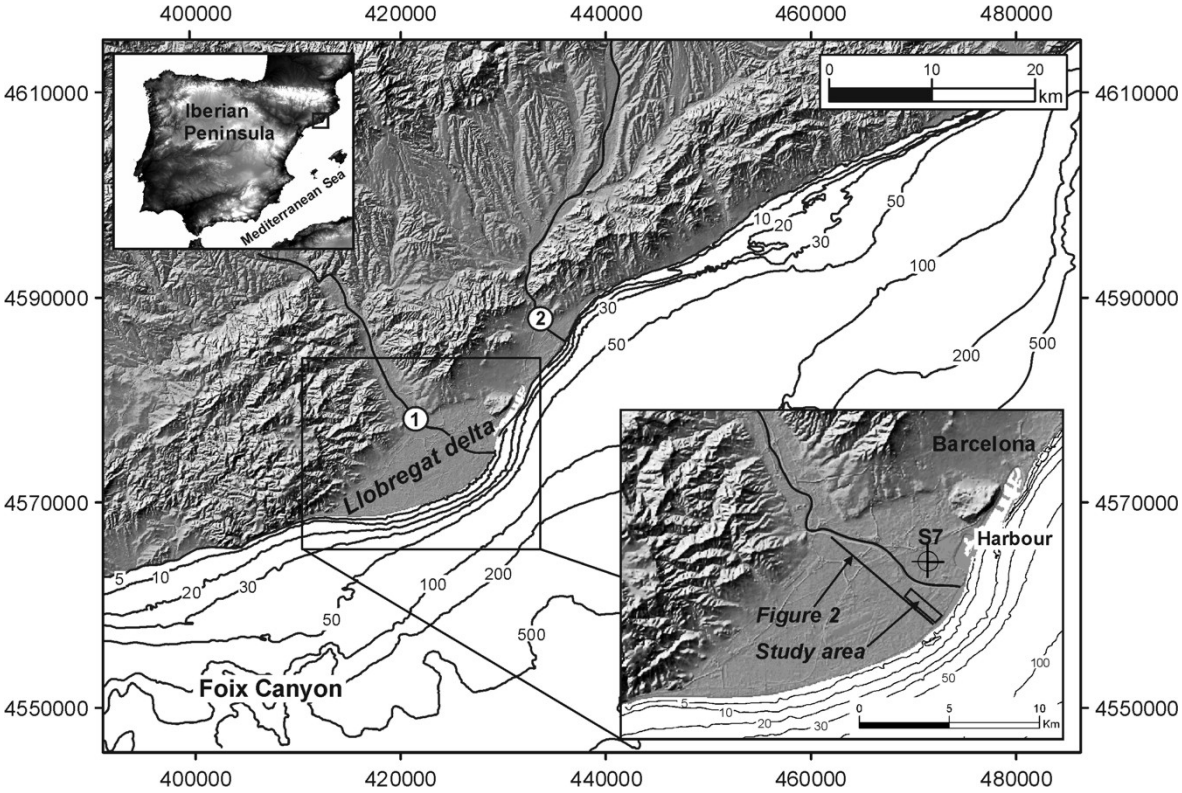

Figure 5.1.1. Location of the study area in the Llobregat delta near Barcelona harbour, northeast Spain. Location of the S7 borehole from where dated samples were available is also shown. Main rivers and submarine canyons are indicated: (1) Llobregat river, (2) Besós river and (3) Foix Canyon. See also location of Figure 5.1.2. UTM coordinates.

westwards, the Llobregat prodelta interfingers with the prodelta of the Besós river. Altogether, the Llobregat-Besós prodelta system covers an area of 165 km^2 along the inner and mid-shelf (Checa et al., 1988).

The Llobregat continental shelf is dominated by a low-energy wave regime, with a strong southward geostrophic flow (30 cm·s^{-1}) on the outer shelf (La Violette et al., 1990). The Foix Canyon likely funnels most of the fine material escaping from the continental shelf as suggested by a well preserved ^{137}Cs signal. This is further supported by the fact that centennial to modern sedimentation rates show higher values in the canyon upper course than off the Llobregat river mouth where rates from 5.8 ± 0.3 to 3.7 ± 0.12 mm·yr^{-1} have been measured from ^{137}Cs and ^{210}Pb dating methods (Sánchez-Cabeza et al., 1999).

The thickness of Holocene deposits in the Llobregat delta ranges from 20 m close to the delta apex 8 km landward from the present coastline to 60 m at the present coastline, with a thickness of 64 m near the present river mouth (Marquès, 1974; Manzano, 1986). Two radiocarbon dates from prodelta silts (unit E in Fig. 5.1.2) at 58.5 m and 37.5 m below the present delta plain surface obtained from a borehole having its top at 3.5 m above sea level yielded 10 900 ± 140 yrBP and 2300 ± 1200 yrBP, which represent sedimentation rates between 5.3 and 5.4 mm·yr^{-1}, and 10.7 and 34 mm yr^{-1}, respectively (Marquès, 1974; Manzano, 1986). These values are in good agreement with those from Sánchez-Cabeza et al. (1999).

The general architecture of the Llobregat delta consists of six lithological units (Fig. 5.1.2), which from bottom to top are: (i) a lower unit of Pliocene blue clays and shales with shell fragments (A in Fig. 5.1.2); (ii) Pleistocene fluvial gravels probably younger than 18 000-15 000 yrBP, forming a lower aquifer, that grade

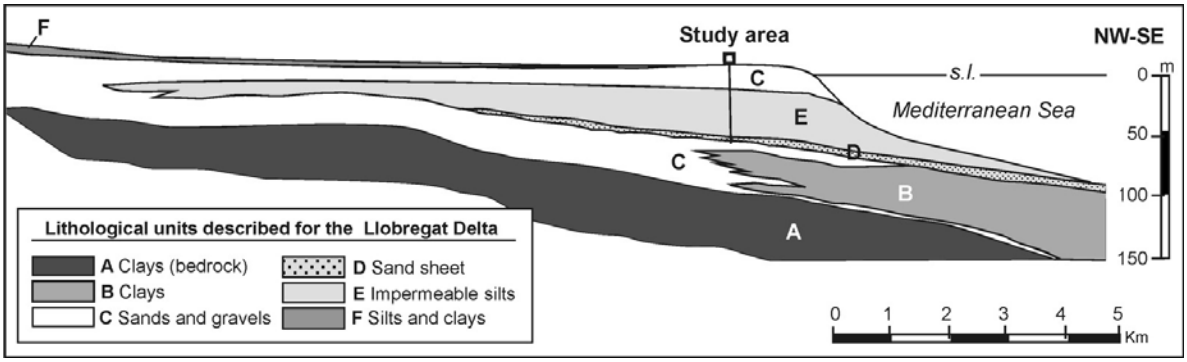

Figure 5.1.2. NW-SE geological cross-section showing the general architecture of the Llobregat delta (see location on Fig. 5.1.1). Main lithological units are shown: Unit A corresponds to lower Pliocene blue clays, unit B to Pleistocene clays; the lower part of C is made of ravinement and fluvial sands and gravels; unit D is constituted by transgressive sands; unit E is represented by Holocene prodelta deposits; the upper part of C are gravels, sands and some silts from delta front and delta plain environments; and unit F corresponds to the superficial level with flood plain fine sediments. Modified from Marquès (1974), Bayó (1985) and Ventayol (2003).

to offshore clays (lower part of C and B in Fig. 5.1.2); (iii) transgressive sands (D in Fig. 5.1.2); (iv) Holocene prodelta deposits made of impermeable clayey silts (E in Fig. 5.1.2); (v) delta front and delta plain gravels, sands and some silts, forming an upper aquifer (upper part of C in Fig. 5.1.2); and (vi) an uppermost unit made of flood plain fine sands, silts, clays and marsh clays (F in Fig. 5.1.2) (Marquès 1974; Bayó 1985; Ventayol, 2003).

According to Checa et al. (1988), a relict delta formed at the end of the Versilian transgression from 10 900 to 6000 yrBP, both ages corresponding to sea level stabilizations at 65 and 22 m below present sea level, respectively. During that period, the Llobregat mouth migrated 30 km northeastwards from a former location close to the head of the Foix Canyon to its current location as a response to sea level rise. This was a local effect of a synchronous reorganization of sedimentary systems detected along the continental shelves in the entire Northwestern Mediterranean (Aloïsi, 1978).

5.1.3. Material and methods

Data from 19 CPT and 47 CPTU tests and 18 boreholes performed in direct relation and prior to the construction of a large new sewage treatment plant on the delta plain of the Llobregat river have been used in this study (Fig. 5.1.3). Most of the boreholes reach subsurface depths between 40 and 66 m. The sediment facies in the boreholes used for groundtruthing purposes are described in Domínguez (2002). The penetration depth of the CPT/CPTU tests varies from 26 to 63.8 m. As related to the size of the study area (1430 m x 330 m = 471 900 m^2), this represents one CPT/CPTU tests for each 7150 m^2 and one borehole for each 26217 m^2, approximately. However, while the number of in situ tests and boreholes can be considered high, their spatial distribution was not perfectly regular, as shown in Figure 5.1.3. This required applying specific interpolation techniques in order to construct a 3D model of the study area (see Section 5.1.3.2).

5.1.3.1. CPT/CPTU tests: measurements and procedures

CPT and CPTU testing tools consist of a cone (60º of cone opening angle, 3 cm of height and 10 cm^2 of basal area) located at the lower end of a succession of metallic cylinders pushed down at constant speed by the force of a push engine located on a truck or platform. The thrust capacity for the equipment used was 20 tonnes (200 KN). A conducting cable through the cylinders links the cone tip to the recording units so that data are acquired and could be displayed on line.

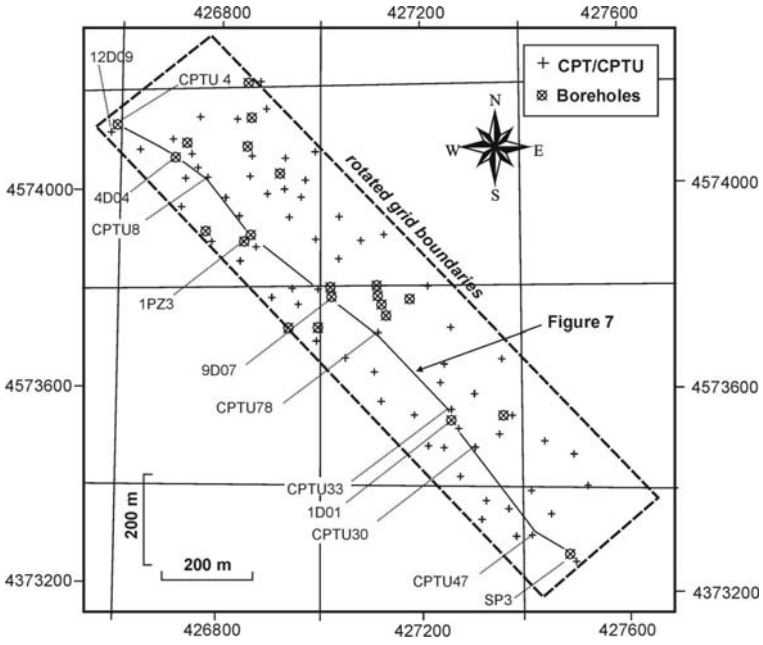

Figure 5.1.3. Sampling location. Rotated gridding boundaries correspond to a regular grid orientated parallel (135º) to the modern Llobregat river course (see in Fig. 5.1.1). See also location of Figure 5.1.7. UTM coordinates .

The tested parameters are (i) cone resistance (q_c, measured in MPa), corresponding to the soil resistance per unit area to penetration at the cone penetrometer tip, (ii) the friction (f_s, measured in MPa) of the sediment per unit area along the 150 cm^2 sleeve of the tool and (iii) the pore pressure at the tip (u, measured in MPa), which can be assessed only with piezocones (CPTU). These parameters are measured at a constant speed of 2 $cm \cdot s^{-1}$, visualized and recorded in real time. Equipment and procedures were in accordance with ASTMD 5778-95 (2000).

Cone tip resistance, q_c, is an indicator of density and consistency of soil changes. The most often used parameter for friction is the friction ratio (FR, measured in %), which has been found to be indicative of grain size and texture. FR and f_s, are related by (1):

$$FR\ (\%) = f_s / q_c \times 100 \qquad [1]$$

When q_c is plotted against FR, every soil can be classified as an expression of grain size and consistency, where increasing FR corresponds to increasing fine content. The most often used q_c/FR plot is known as Robertson's classification chart from Robertson et al. (1986).

When the cone is subjected under an all-around water pressure during a CPTU test, there is usually a shift in the zero for both friction sleeve and cone tip resistance measurements. In this case, the cone tip records a stress that is less than the applied all-around pressure because of the unequal area at the tip. Because of this effect, often referred as the "unequal area effect", it is recommended for q_c values to be reported as total resistance q_t whenever possible (Campanella et al., 1983). This correction [2] is important in soft clays and silts where q_c is generally low and the excess pore pressure is very high:

$$q_t = q_c + u\ (1\text{-}a) \qquad [2]$$

where u is the pore pressure acting behind the cone and a is the cone area ratio (Robertson, 1990). The measured pore pressure changes are a function of in-situ pore pressure, stress state, sediment permeability, density, plasticity and stress history. Therefore, pore pressure is considered to be a more reliable parameter than q_c in resolving unit boundaries so the differentiation of lithological units by the cone is made using the excess pore-pressure

A *Soil behaviour type identification from Robertson et al. 1986*

q_c/FR	Soil behaviour type
1	Sensitive fine grained
2	Organic material
3	Clay
4	Silt clay to clay
5	Clayey silt to silty clay
6	Sandy silt to silty clay
7	Silty sand to sandy silt
8	Sand to silty sand
9	Sand
10	Gravelly sand to sand
11	Very stiff fine grained*
12	Sand to clayey sand*

(*overconsolidate or cemented)

B *Sediment facies characterization from the study area*

Facies	q_c (MPa)	FR (%)
Delta plain facies		
Flood plain silts and silty sands	2 - 4	0.7 - 5
Crevasse sands	6 - 9	0.5 - 3.5
Fluvial channel sands	14 - 25	0.2 - 0.7
Delta Front facies		
Sand ridges	8 - 20	0.3 - 1.4
Delta front silts and clays	1 - 3	2.3 - 6
Prodelta silts and clays	1 - 1.7	1.5 - 6

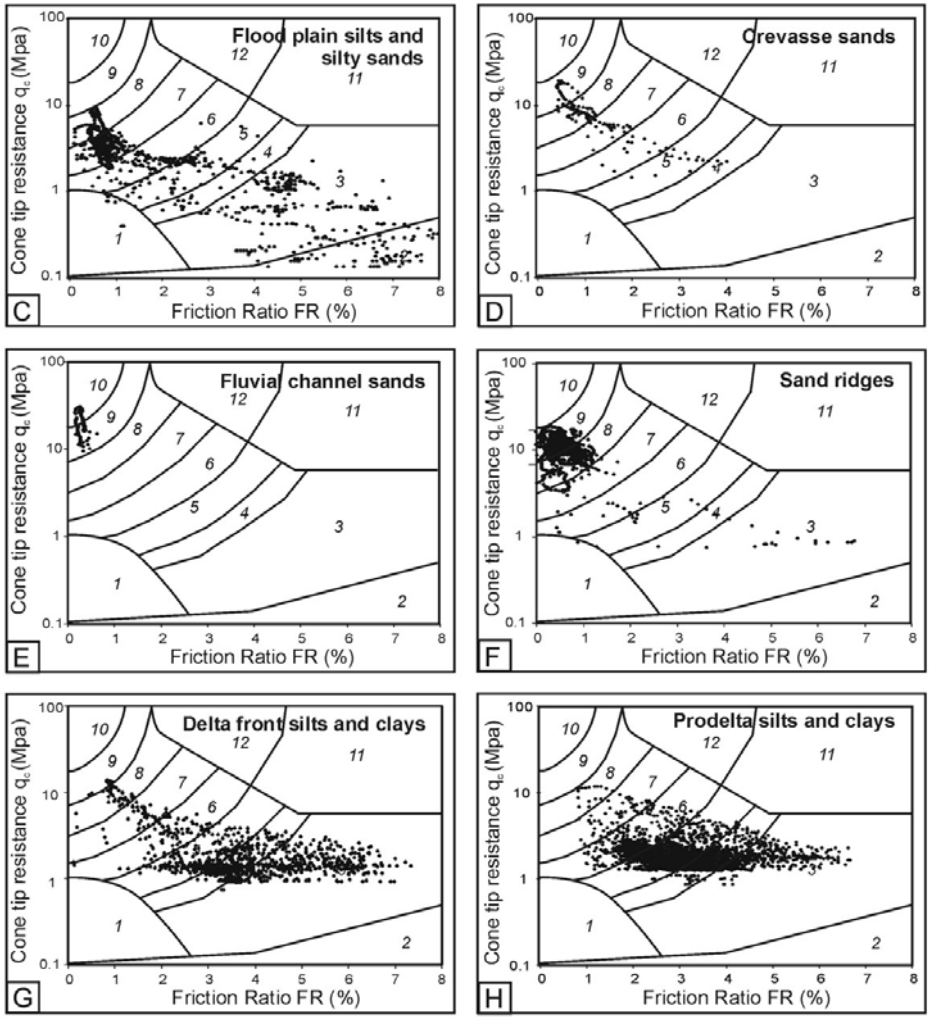

Figure 5.1.4. A: q_c/FR values and soil behaviour type given in Robertson's et al. chart (1986) of soil classification. B: Characterization of sediment facies in the study area. C to H: q_c/FR values for each type of sediment facies in the study area.

data, whereas the characterization of each individual unit can be made using any of the measured or derivative parameters, q_c, f_s, u or FR or combinations of these parameters (Moran et al., 1989).

Nevertheless, after groundtruthing CPT/CPTU profiles with the boreholes from the study area (Fig. 5.1.4) we noticed that q_c allowed us to distinguish sedimentary facies most effectively. Differentiating between q_c and q_t did not bring any additional advantage in distinguishing soil types, at least in our case. Generally, the measured and corrected tip resistance (q_c and q_t) in sands are essentially the same value (Lunne et al., 1997, Liao et al., 2002). Therefore, q_c was chosen to identify sediment bodies as for this purpose correction (2) proved negligible (Devincenzi et al., 2003). The use of q_c also permits us to directly use CPT/CPTU data since this parameter is measured in both tests.

Among the several charts existing for evaluating the soil type, we have used the Robertson's chart (Fig. 5.1.4), which is based on q_c and FR. This chart identifies twelve soil types according to their behaviour in terms of q_c/FR ratio, as described in Figure 5.1.4A. These range from sensitive fine grained, organic and clayey soils to gravelly sands to overconsolidated or cemented sands. After facies correlation, data groups were plotted in Robertson's chart as derived from q_c and FR profiles, thus allowing the geotechnical characterization of the sedimentary facies (Figs. 5.1.4B-4H).

5.1.3.2. 3D modelling

A 3D model of the study area in the Llobregat delta was created from irregularly spaced data with x, y and z coordinates and a property value (e.g. q_c). Regridding of those data was performed in order to obtain a regularly spaced three-dimensional grid. Different types of statistical approaches can be used to distribute data into a grid. Several authors have processed previously CPT/CPTU data with the same purpose by clustering, grouping methods and geostatistics (Nadim, 1988; Lacasse, 1995; Hegazy and Mayne, 2002; Devincenzi et al., 2003).

In our work, we have used the 3D Minimum Tension Gridding (3D-MTG) technique, which is an extension of the Minimum Tension Gridding (MTG) bi-cubic spline algorithm used to calculate 3D grid spacing from scattered data points of a given property. Splines have been already used in geological modelling (Eddy and Looney, 1993; Flach et al., 2003) and it has been proved that splines are as accurate for interpolation as kriging (Hutchinson and Gessler, 1994).

Applying the MTG technique involves an iterative process, which respects the input data when calculating the evenly spaced grid. First, a coarse grid is calculated and its cubic function is fitted to the grid nodes using the original input data. Following the iterations, the value of the grid node is evaluated and compared to the input data. If an original data point is located within half of the width of a grid cell, the point is compared to the grid node. As gridding progresses, the remainder between grid nodes and the original input data points usually decreases. However, if the remainder increases, each grid node is reset to the value that is numerically closest to the input data point.

3D grids of scattered data enable information to be shared along a finite number of spatial planes within a specific volume, therefore producing an accurate representation of the spatial variation of the property considered. However, careful evaluation of the results throughout the modelling process and technically-based decisions in setting variable parameters are key elements in the ultimate success of this type of application.

In our modelling, a grid rotation of 135º was chosen to minimize extrapolation effects where data were missing since this angle corresponds to the main directional trend of sedimentation in the study area, roughly coinciding with the orientation of the river's

course. A grid rotation only implies a new coordinate system rotated 135º with respect to the input data system of coordinates. A very low value, 0.01, was selected for vertical influence to remove weight from data above or below each interpolation node relative to data on the horizontal plane of that node (Flach et al., 2003). Otherwise, high smoothing may occur in the horizontal plane. In addition, a low vertical influence factor results in the elongation of the sediment bodies thus yielding more realistic models for coastal plain environments (Eddy and Looney, 1993). The grid size applied in our study was 5x5x0.5 meters (x, y, z).

A different interpolation technique using kriging algorithms was applied to the same study area by Devincenzi et al. (2003), who obtained very similar geometries to the ones from the present study where the MTG technique has been employed. For that reason, the application of the MTG is recommended when a high density of data is available and simple architectures are expected.

5.1.4. Results

5.1.4.1. Sediment facies characterization based on q_c and FR

Sediment facies have been characterized from q_c and FR values. The general response of q_c and f_s to changes of material type generally results in high q_c (>8 MPa) and low FR (<2 %) for sandy soils whereas soft clayey soils tend to give low q_c (< 4 MPa) and high FR (>4%) (Lunne et al., 1997). A general increase of q_c from bottom to top may be expected in the study area since deltas are made of coarsening-upwards sequences (Shepard et al., 1960). Consolidation effects may also produce increasing q_c with depth.

q_c and FR values found for the sediment facies are given in section B of Figure 5.1.4, which includes attribution to specific sedimentary environments obtained from groundtruthing with boreholes of nearby CPT/CPTU sites within the overall study area. The values in Figure 5.1.4B correspond to intervals of q_c /FR values including more than 70% of the data points represented on each sediment facies specific plot from Figure 5.1.4C to 4H.

Delta plain facies display a broad q_c range (2 to 25 MPa) as could be expected from the variety of deposits accumulating in this environment, which includes flood plain silts and silty sands, crevasse sands and fluvial channel sands. Flood plain silts and silty sands are the most common sediment type, with >70% of the q_c values from 2 to 4 MPa and 0.7 to 5% FR. However, observed lower q_c values and higher FR values (Fig. 5.1.4C) in flood plain sediments of the study area have been attributed to the presence of organic material and clays as mostly indicated by scattered data fitting into Robertson's soil types 2 and 3. Crevasse sands mostly display q_c values between 6 and 9 MPa with FR values between 0.5 and 3.5% (Fig. 5.1.4D). Finally, fluvial channel sands present the highest q_c (14-25 MPa) and the lowest FR (0.2-0.7 %) (Fig. 5.1.4E). As can be deduced from the above data and the plots in Figure 5.1.4, the higher q_c values corresponds to the coarser sediment type and, viceversa, the lowest q_c corresponds to the finest sediment type. FR shows an opposite behaviour as should be expected from expression [1] above (see section 5.1.3.1).

Delta front facies are mainly made of sand ridges where coarsening-upwards sequences ranging from fine sands and silts with variable clay content to upper well sorted sands. In sand ridges, most q_c values shift from 8 to 20 MPa whereas FR values mainly fit in the range of 0.3 to 1.4 % (Fig. 5.1.4F). More than 70% delta front silts range between 1 and 3 MPa for q_c and 2.3 and 6 % for FR, though some variability has been observed in the study area (Fig. 5.1.4G) likely due to lower sorting. In comparison with fluvial channel sands, delta front sand ridges tend to show lower q_c values (occasionally <10 MPa) due to their relative smaller grain size. Minor order coarsening-upwards sequences have been

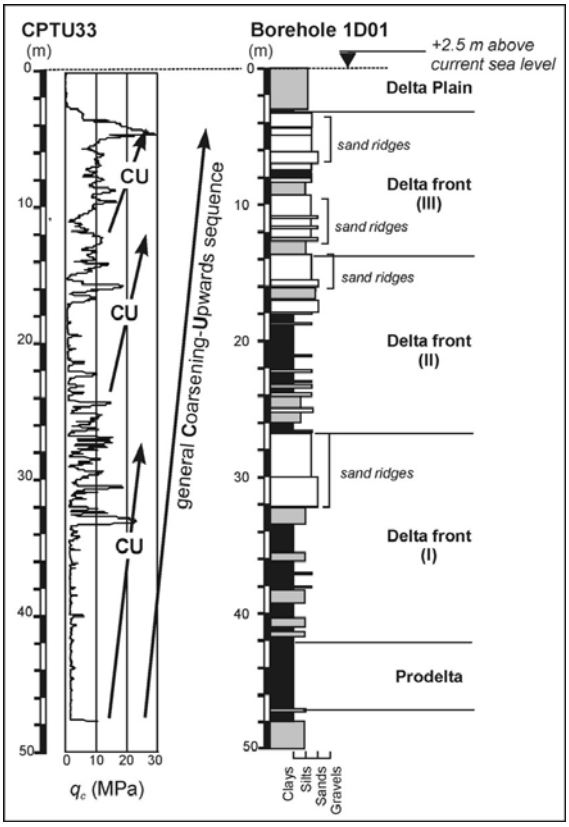

Figure 5.1.5. Correlation between the q_c profile from the CPTU33 test and the borehole 1D01 (see location in Fig. 5.1.3). Borehole 1D01 vertical scale has been cut at 50 m of depth. Minor coarsening-upwards sequences (CU) within the general coarsening-upwards sequence have been easily detected by the penetration tests, according to the stratigraphic record (see delta, prodelta and delta front environments, I-II-III, and sand ridges) of borehole 1D01.

registered by increases in qc from delta front silts and clays to sand ridges (Figure 5.1.5). The distinction between delta front silts and flood plain silts is more subtle although in general delta front silts tend to be somewhat finer.

Prodelta facies consist of silts with clayey silt and clay intervals. Also rare thin sandy intercalations are observed, with q_c values up to 10 MPa. Dominant prodelta facies have a narrow range of q_c, between 1 and 1.7 MPa, with few samples showing higher values. FR varies from 1.5 to 6 % (Fig. 5.1.4H).

Most of the CPT/CPTU penetration depths in the study area were shallower than the top of the transgressive sand sheet. The basal gravels described in the literature (units C and D in Fig. 5.1.2) were not profiled, though they were sampled in the boreholes. Penetrating coarse materials may seriously damage the delicate cone tip used in the tests and, therefore, we stopped testing before reaching such materials.

5.1.5.2. Identification of sediment bodies from the 3D model

The q_c isosurface model constructed from the interpolated grid, obtained after application of the 3D-MTG technique (see section 5.1.3.2) on the original data, is useful to identify the geometries of the wedge-shaped sediment bodies in the study area, and the 3D variability of each soil property. The boundaries of the model have been adjusted to the precise location of the outermost data in the study area with the aim of avoiding wrong calculated values to appear. A general view of the 3D isosurface model showing the geometries of sediment bodies in the study block is presented in Figure 5.1.6.

The 3D model clearly displays high q_c values at top and low values at the bottom (Fig. 5.1.6). Decreasing q_c values with depth prove the expected general coarsening-upwards sequence (see section 5.1.4.1) since we consider consolidation effects to be little significance. Four wedge-shaped sediment bodies U1 to U4 prograding southeastwards have been identified and described according to the sediment facies characterization (section 5.1.4.1.) and their stratigraphic location (Fig. 5.1.6).

The top of the basal U1 in Figure 5.1.6A lies at 47 to 60 m depth below sea level (0 line in Fig. 5.1.6) with depth increasing from NW (landward) to SE (seaward). According to the general model in Figure 5.1.2, such a depth is just above the sands left by the transgression. We hypothesize that the silts tested would have been deposited during the transgression on top of the sands, thus resulting in a fining upwards transgressive sequence.

Transgressive sands would equally grade seaward into finer silty sediments. q_c values of basal transgressive silts ranging from 2 to 6 MPa could be erroneously attributed to flood plain silts and silty sands because of their similar q_c values, the 3D model being of fundamental importance to avoid such as potential mistake.

The three upper bodies (U2, U3 and U4 in Fig. 5.1.6A) present similar q_c distributions, with highest values at the top of each. The top of the units is, therefore, likely made of sand ridges (q_c between 8 and 20 MPa, green tones) separated from underlying delta front silts and clays and prodelta silts and clays (q_c lower than 8 MPa, Fig. 5.1.6B) by sharp boundaries. These q_c trends clearly indicate that sediment bodies U2, U3 and U4 form coarsening-upwards sequences.

Fluvial channels (Fig. 5.1.6C) with q_c values of 26-32 MPa filled by sand ridges are observed close to the northwestern end of sediment body U2 of Figure 5.1.6. This sediment body is 37 m thick at the landward end of the study block, where its top is located at 10 m depth, and >26 m at its seaward end (Fig. 5.1.6D). Its upper boundary is tilted 7º seaward. Decreasing q_c in the upper levels of sediment body U2 seaward illustrates how delta front sand ridges pinch out to the SE.

Sediment body U3 (Fig. 5.1.6) is 19 m thick at the SE end (seaward) of the 3D block and its upper boundary displays a slope of up to 3º. Because of q_c values that do not vary greatly, it has not been possible to identify its upper boundary and thus sediments bodies U3 and U4 appear amalgamated landwards (Fig. 5.1.6D), where they have 10 m of thickness altogether. The upper boundary of sediment body U4 constitutes the modern delta plain. The thickness of this body ranges from 13 m at the SE end to less than 10 m at the NW end (Fig. 5.1.6C).

Whereas section 6D shows that the depth distribution of q_c values varies along the main SE -NW axis of the 3D block, cross sections 5.1.6E to 5.1.6G also illustrate SW-NE heterogeneities in the distribution of q_c values corresponding to lateral changes of sediment properties (Fig. 5.1.6D to 5.1.6G). This is particularly the case for the upper part of sediment body U2 as shown in Figure 5.1.6F. Figure 5.1.6H shows a horizontal slice at 5 m depth below sea level highlightening q_c variability in the upper sediment wedge or body U4. Slicing at greater depths would show a similar pattern for the sediment bodies below.

5.1.5. Discussion

The high potential for distributed grids of CPT/CPTU tests to identify the geometry of sediment bodies in deltaic settings and to discriminate the associated sediment facies and their lateral and vertical relations is illustrated by the study case of the Llobregat delta. The use of just one property measured directly (q_c) and a second derived parameter (FR) has proved to be sufficient to image with high resolution the 3D structure of the delta. In this way, three prograding sediment wedges, which we have named U2, U3 and U4 in Figure 5.1.6 have been identified down to a depth of 60 m below sea level in the study area. The geometry of the lowermost sediment body (U1 in Fig. 5.1.6) is uncertain because of the scarcity of data at the depths where it lies, though a wedge-shaped form can be inferred from the seaward slope of the upper boundary and from borehole data (Fig. 5.1.7).

Borehole data are essential in avoiding interpretation errors of q_c profiles and, therefore, to groundtruth the estimate of grain size tendencies from penetration tests. However, specific facies have proved in practice difficult to differentiate not only from q_c profiles but also in borehole cores by simply using grain size criteria. This is in particular the case of silts and clays from the delta front and prodelta environments, which show very similar q_c values and similar grain sizes (see Fig. 5.1.4B). It has to be taken into account that under specific circumstances, like the appearance of very thin layers of silts and clays, the

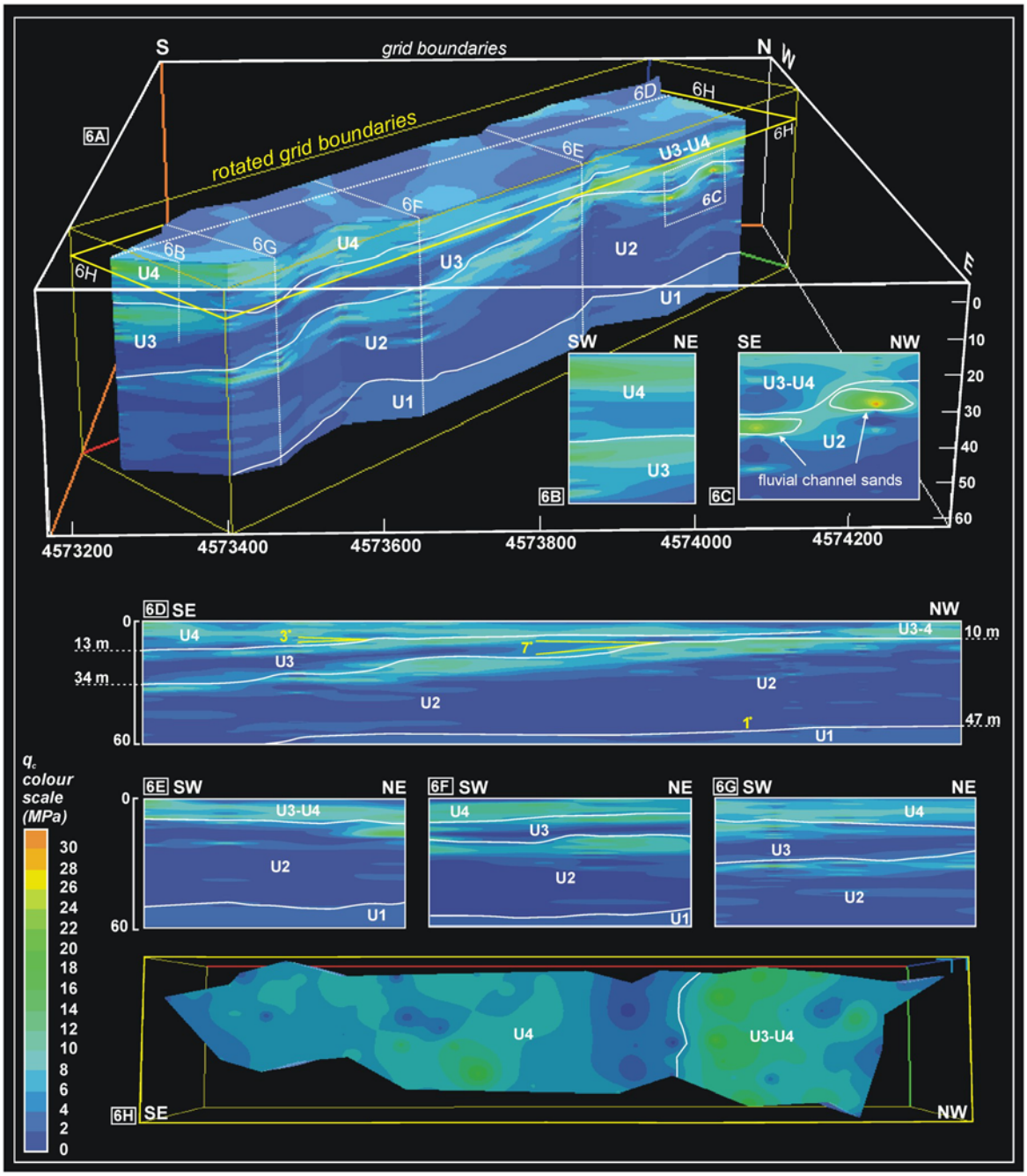

Figure 5.1.6. 3D model of q_c. Isosurfaces correspond to 2MPa intervals. A q_c colour scale is shown on the left border. The rotated grid boundaries and general grid boundaries are given with UTM coordinates in meters. Sediment bodies identified from the model are indicated as U1, U2, U3 and U4 from bottom to top. The 3D model clearly displays high q_c values at top and low values at the bottom (dominance of green tones at the top and blue tones at the bottom). A: General view of the q_c 3D model; B, Highest q_c values are found at the top of the sediment wedges (U3 and U4) suggesting coarsening-upward sequences; C, sand-filled fluvial channels cut in the sand ridges of wedge U2; D, SE-NW cross-section showing inclinations of the boundaries of each wedge and reference depths. Wedges U2 and U3 display 7º and 3º slopes; E to G, SW-NE cross-sections showing lateral changes in q_c values and the depths at which wedges are found; H, Horizontal slice at -5 meters where U4 changes in q_c values are displayed.

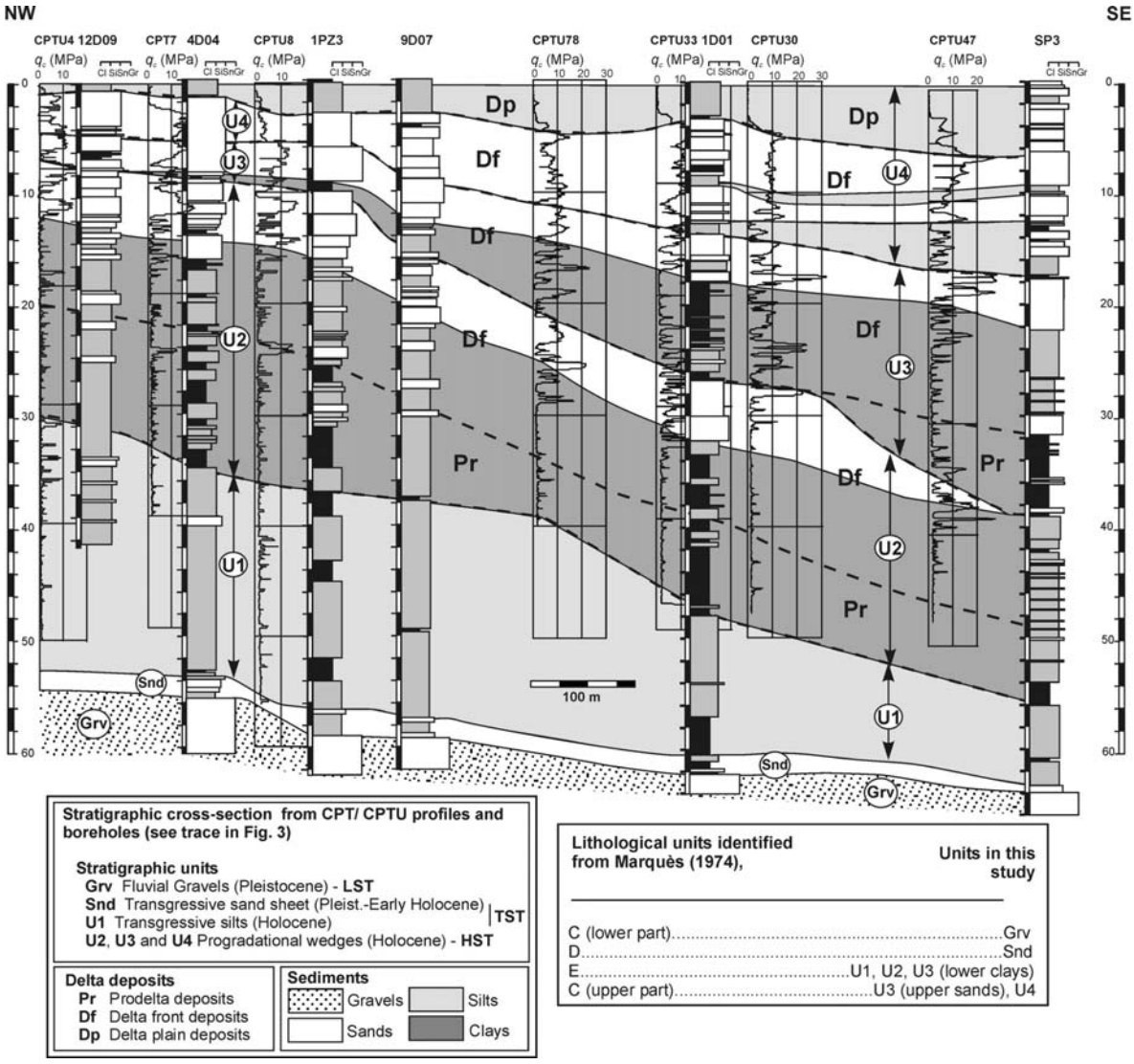

Figure 5.1.7. NW-SE stratigraphic cross-section showing the six stratigraphic units identified in the study area (from base to top, Grv: Pleistocene lowstand gravels, Snd: transgressive sands, U1, U2, U3 and U4 Holocene sediment bodies). Correlation between boreholes and CPT/CPTU profiles is shown. See location of cross-section in Figure 5.1.3. The depositional sequence represented in this cross-section comprises three systems tracts. The lowstand systems tract (LST) is represented by fluvial gravels (Grv). The transgressive systems tract (TST) presents a basal transgressive sand sheet (Snd) and transgressive shelf silts (U1). The highstand systems tract (HST) is constituted by three prograding wedges (U2, U3 and U4) where prodelta (Pr), delta front (Df) and delta plain (Dp) sediment facies are also indicated.

cone may continue sensing the sediment just above even when it has already entered a new material, which may thus not be sensed (Lunne et al. 1997). Facies associations provide clues to differentiate sedimentary environments. For example, delta front silts and clays are usually associated with sand ridges (see Fig. 5.1.6B) whereas prodelta silts and clays do not appear to be associated with this type of proximal, shallower sediment facies (see U4 in Fig. 5.1.7).

The general architecture of the Llobregat delta depicted by the four sediment bodies U1 to U4 and the general coarsening-upwards sequence given by the q_c values is consistent with the expected classical general stratigraphic architecture of Holocene deltas as described by Stanley and Warne (1994).

The LST is represented by the lowermost gravels in Figure 5.1.7. These gravels likely correspond to a ravinement surface and to the infill of river channels during the last sea level lowstand. Gravelly units from older Pleistocene lowstands would be found southeastward of the present delta, towards the Foix Canyon area. Lowstand gravels are overlain by a thin transgressive sand sheet (Fig. 5.1.7) accumulated during the shoreface retreat associated with the pre-Holocene and early Holocene rise in sea level. These transgressive sands rapidly were replaced by successions of silts (U1 in Figs. 5.1.6 and 5.1.7) resulting in a TST fining-upwards sequence, as has been shown in other deltas like the Song Hong delta (Hori et al., 2004). However, TST coarsening-upwards sequences have also been described in the Po and Tevere deltas (Amorosi and Milli, 2001).

The HST consists of the three prograding wedges U2, U3 and U4 in Figures 5.1.6 and 5.1.7 indicative of sustained delta growth and shoreline advance phases that, according to Checa et al. (1988), were likely favoured by the stabilization of sea level from 6000 yrBP onwards. At that time, shallowing because of sediment input started to exceed the relative sea level rise along the shoreline of the Llobregat delta. These progradational wedges built an overall coarsening-upwards sequence with vertical transition from prodelta to delta front and delta plain environments (Figs. 5.1.6 and 5.1.7). Similar depositional sequences, starting by basal LST deposits overlain by TST and HST deposits, have been identified in other areas of the Spanish continental shelf (Hernández-Molina et al., 1994; Somoza et al., 1998; Fernández-Salas, 2003).

The observed progradational stacking pattern likely reflects three cycles of deltaic build-up on the Llobregat coast produced by high frequency sea level oscillations (sixth-order sea level cycles of 1-2 x 103 years), as has also been observed in the Ebro delta by Somoza et al. (1998) and in southern Spain (Hernández-Molina et al., 2002; Fernández-Salas et al., 2003). High frequency climatic fluctuations, interpreted as related to short cool/humid events observed in the Ebro delta (Somoza et al., 1998), would cause relative sea level falls and increases in the sediment supply related to higher precipitation. Therefore, deltaic progradations identified in this study are may occur during stillstands after sea level falls of varying amplitudes related to such climatic excursions.

5.1.6. Conclusions

The cone tip resistance (q_c) constitutes a simple parameter that can be interpreted in terms of sediment facies. Prodelta, delta front and delta plain sediments have been characterized in terms of lithology, geometry and vertical grain size variations. Particularly, flood plain silts and silty sands, crevasse sands, fluvial channel sands, sand ridges, delta front-prodelta silts and clays, have been identified using boreholes. The use of q_c is suitable for discriminating between sediments with contrasting grain size. As an example, a distinction between delta front silts and prodelta silts is not obvious from q_c only.

CPT/CPTU measurements provided a high-resolution data set of the Llobregat delta suitable for 3D modelling. The 3D Minimum Tension Gridding technique constitutes a useful and practical tool to interpolate these data since its application has proved to be simpler than other methods and no large calculations are required. Extension of CPT/ CPTU into the study area allowed us to delineate sediment bodies in a three dimensional space, improving interpretations.

A 3D model integrating data from 66 CPT/ CPTU tests has shown with great detail the internal structure of the Holocene highstand sediment package in the study area, which is represented by three prograding wedges. The high stratigraphic potential of the CPT/CPTU profiles has allowed us to recognize small-scale grain size variations (Fig. 5.1.5), such as the few-meter thick coarsening-upwards sequences present in the prograding wedges

(Fig. 5.1.6B) and fluvial-channel sands (Fig. 5.1.6C). The progradational phases identified in the HST are related to relative sea level changes caused by high frequency climatic events according to observations in neighbouring delta areas.

Ongoing ^{14}C AMS radiocarbon dating will provide, in the near future, a much more precise time frame for the 3D evolution of the Llobregat delta and the age of its building blocks, namely the sandy and silty HST prograding wedges and the interfingering finer layers. Imaging the 3D geometries and understanding how they form is of prime importance for sequence stratigraphy and reservoir purposes as well as for geotechnical engineering. Diagnostic geotechnical properties from which other interesting parameters are derived could be predicted spatially through 3D modelling as illustrated by this Llobregat delta case study.

Acknowledgements

The authors would like to thank DEPURBAIX, S.A. for releasing the data used in the work. We wish to express our gratitude to Pere Busquets and Oriol Falivene, University of Barcelona, for interfacing with DEPURBAIX and for helpful advice and reviewing. This research is supported by the EC EURODELTA (EVK3-CT-2002-20001) and PROMESS 1 (EVR1 -CT-2001-00041) projects and the Spanish PRODELTA project (REN2002-02323). GRCGM is funded by Generalitat de Catalunya through its research groups program (ref. 2001 SGR-00076). SL benefited from a Ministry of Education and Science grant.

5.2. Subseafloor stratigraphic profiling and soil classification from piezocone tests: A case study in the gulf of Lion (NW Mediterranean Sea)

S. Lafuerza (1), J. Frigola (1), M. Canals (1), G. Jouet (2), M. Bassetti (3), N. Sultan (2), S. Berné (3)

(1) GRC Geociències Marines, Departament d'Estratigrafia, Paleontologia i Geociències Marines, Universitat de Barcelona, Spain
(2) Institut Français de Recherche pour l'Exploitation de la Mer, France
(3) IMAGES, Université de Perpignan Via Domitia, France

Abstract

We show the results provided by piezocone tests in determining the stratigraphic profile and the soil classification of two drilling sites in the outer shelf and the upper slope of the Gulf of Lion, PRGL2 and PRGL1, respectively. Correlations with grain-size data indicate that sleeve friction can be used for profiling fine-grained sediments (site PRGL1) whereas cone tip resistance is the most adequate for sequences made of alternations of coarse and fine-grained intervals (site PRGL2). Normalized cone resistance and friction ratio proved to be also appropriate for soil stratigraphy as it depicts trends in the coarse fraction of the tested soil. Silts and clays present in similar proportions at site PRGL1 responded to piezocone testing as pure clays usually do. Consequently, classical soil classification methods resulted in erroneous interpretation of these sediments as clays, whereas classification of the heterogeneous deposits at PRGL2 was consistent with the grain-size. When tied to a high resolution seismic reflection profile, the stratigraphy interpreted from the piezocone profile matches with the main seismic sequences and discontinuities defined from seismic stratigraphy analysis. Graded bedding also matches with cone tip resistance and sleeve friction data.

Keywords: piezocone, stratigraphy, soil classification, Gulf of Lion

2008, Geochemistry, Geophysics, Geosystems, Vol. 9 (12), Q12028
Doi: 10.1029/2007GC001845

5.2.1. Introduction

The EC funded "PROfiles across MEditerranean Sedimentary Systems 1" (PROMESS 1) research project was designed to obtain very long sediment cores and perform in situ physical measurements from two continental margins in the Mediterranean Sea (Berné et al., 2004a). In the Gulf of Lion, drilling and in situ testing were carried out at two sites: PRGL1 in the upper slope at 298 meters of water depth (mwd) and PRGL2 in the outer shelf at 103 mwd (Fig. 5.2.1). Five boreholes were drilled at site PRGL1 site (PRGL1_1 to PRGL1_5) and two at site PRGL2 (PRGL2_1 and PRL2_2). In this technical brief we compare the stratigraphic profile and soil type classification interpreted from piezocone measurements performed at sites PRGL1_3 and PRGL2_1 with grain size data acquired from sediment cores at PRGL1_4 and PRGL2_2 and with high-resolution seismic reflection profiles. The aim of this study is to illustrate the advantages of piezocone tests for (i) soil classification and stratigraphic profiling of marine sediments before drilling and (ii) for the lithostratigraphic interpretation of seismic reflection profiles.

5.2.2. Materials and methods

Piezocone tests (CPTU) were performed using a down-hole cone penetration system that enables CPTU from the base of the borehole in sites PRGL1_3 and PRGL2_1, reaching penetration depths of 150 and 100 mbsf, respectively. The down-hole system latches into the lower end of a drill pipe by applying mud pressure in the borehole, while down-hole data are recorded. The system requires a drilling apparatus for advancing the borehole and a bottom hole assembly that permits latching the thrust machine, of 90 kN capacity. The maximum stroke of the thrust machine is 3 m. This system enables the borehole to be advanced and CPTUs be performed at every depth. Direct measurements of cone tip resistance (q_c), sleeve friction (f_s) and pore pressure (u_2) were recorded at a constant penetration rate of 2cm·s^{-1}. CPTU were performed before

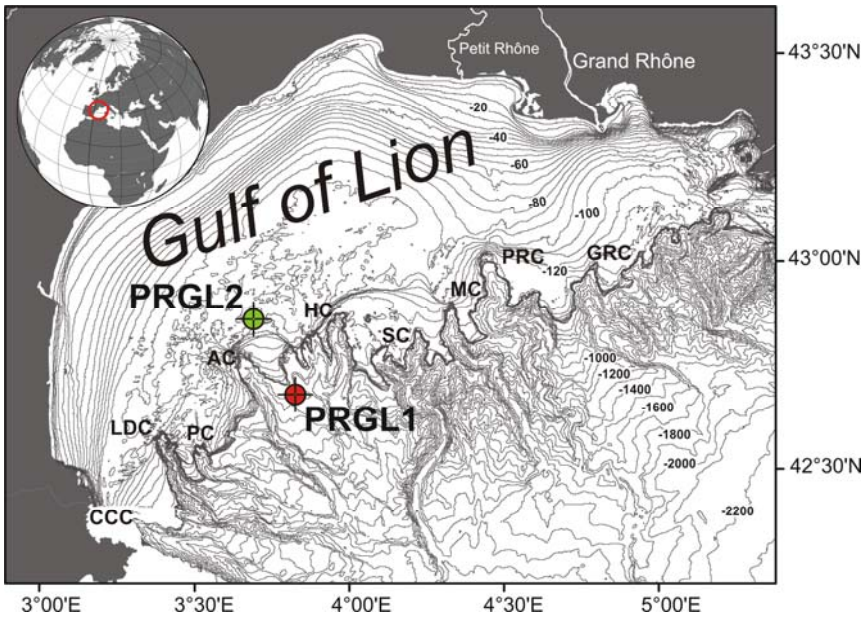

Figure 5.2.1. Location of the PRGL2 (42º50'58.20''N, 003º39'3085''E) and PRGL1 (42º41'23.30''N, 003º50'15.50''E) sites. CCC, Cap de Creus Canyon; LDC, Lacaze-Duthiers Canyon; PC, Pruvot Canyon; AC, Aude Canyon; HC, Hérault Canyon; SC, Sète Canyon; MC, Montpellier Canyon; PRC, Petit Rhône Canyon; GRC, Grand Rhône Canyon. Bathymetry in meters from Berné et al. (2004b) and Medimap Group (2005). 100 m contour equidistance unless otherwise indicated. Names after Canals (1985).

drilling for coring providing a reliable lithostratigraphic profile.

Derived parameters from CPTU, such as the normalized cone resistance (Qt), the friction ratio (FR) and the pore pressure ratio (Bq) (see List of Symbols), allow the identification of the soil type using the soil classification charts proposed by Robertson (1990) and Ramsey (2002). Both methods define nine soil classes according to Qt/FR and Qt/Bq ratios but numbers are referred to soil classes distinctly (Figs. 5.2.2 and 5.2.3). Changes in profiles of q_c, f_s, have been followed for delineating the stratigraphic profile and the ratio of Qt/FR for correlating with grain size curves. q_c and Qt respond to variations in the resistance generated by the coarse fraction whereas f_s and FR illustrate changes in the cohesive fraction, which usually corresponds to the fine-grained fraction (Lunne et al., 1997).

The total sediment core recovery from PRGL1_4 and PRGL2_2 was 300 and 100 m, respectively. Grain-size analyses were carried out in both the bulk and the carbonate free fractions using a Laser Particle Sizer (LPS) Coulter LS100 at PRGL1_4 (Frigola et al., 2008 personal communication) and a LSP Coulter LS230 at PRGL2_2 (Bassetti et al., 2008). Since laser diffraction methods are claimed to underestimate plate-shaped clay mineral percentages, we consider the clay-silt limit at 8mm following the method proposed by Konert and Vandenberghe (1997). The particle sizes considered are: (i) clays with diameter (ϕ) between 0 and 8 μm; (ii) silts with $8<\phi<63$ μm and (iii) sands with $\phi > 63$ μm.

Geotechnical stratigraphy derived from CPTU was correlated with the seismic stratigraphy established by several authors. Six seismic sequences (S0 to S5), corresponding to 100 ky glacial-interglacial cycles, are bounded by major erosion surfaces (D30 to D70) (Berné et al., 2004a and this issue; Rabineau et al., 1998 and 2005). Within the last sequence (S5), other relevant secondary unconformities (D65, D64, D63 and D61) are identified (Jouet et al., 2006 and see review by Bassetti et al., 2008).

5.2.3. Results

5.2.3.1. CPTU tests at PRGL1 site

At PRGL1_3 the cone tip resistance, q_c, and the pore water pressure, u_2, increase quasi-linearly with depth, whereas the sleeve friction, f_s, depicts a more variable profile (Fig. 5.2.4). Note that the three-m-spaced negative peaks in u_2 curves are losses in CPTU readings, and therefore, are unrelated to soil type changes. Five geotechnical-stratigraphic units were identified based f_s values trend. These units have been numbered from I to V from top to bottom. Subunits are identified by alphabetical subindexes (Fig. 5.2.4). Soil classifications charts in Figures 5.2.2 and 5.2.3 predict that the geotechnical unit I consists of silty clays and clays whereas units from II to V are uniformly made by clays. Figure 5.2.4 shows the soil type based on the Qt/FR chart from Robertson's (Fig. 5.2.2) at corresponding depths.

Correlation of Qt/FR and grain-size profiles illustrates the correspondence between Qt/FR and the silt/clay ratio (Fig. 5.2.5), supporting the sedimentological interpretation of the soil classes in Figures 5.2.2 and 5.2.3. Furthermore, unit boundaries (red dotted lines, Figs. 5.2.4 and 5.2.5) correspond to marked decreases in clay content accompanied by an evident increase in sand fraction, as observed by increases in Qt/FR. The coincidence of these sharp changes with the end of CPTU sequences suggests those unit boundaries at 36 and 72 mbsf can be located within units IIb and IIId, respectively. In these levels and to a lesser extent at IVd, pronounced positive peaks in Qt/FR correspond to sand content augmentations (Fig. 5.2.5). Main changes in the clay fraction, such as those in subunits IIb, IIId and IVd are clearly identified from the fs profile (Fig. 5.2.6). The inverse variation between Qt/FR and the clay fraction supports the clay-dependence of FR and f_s, as well as

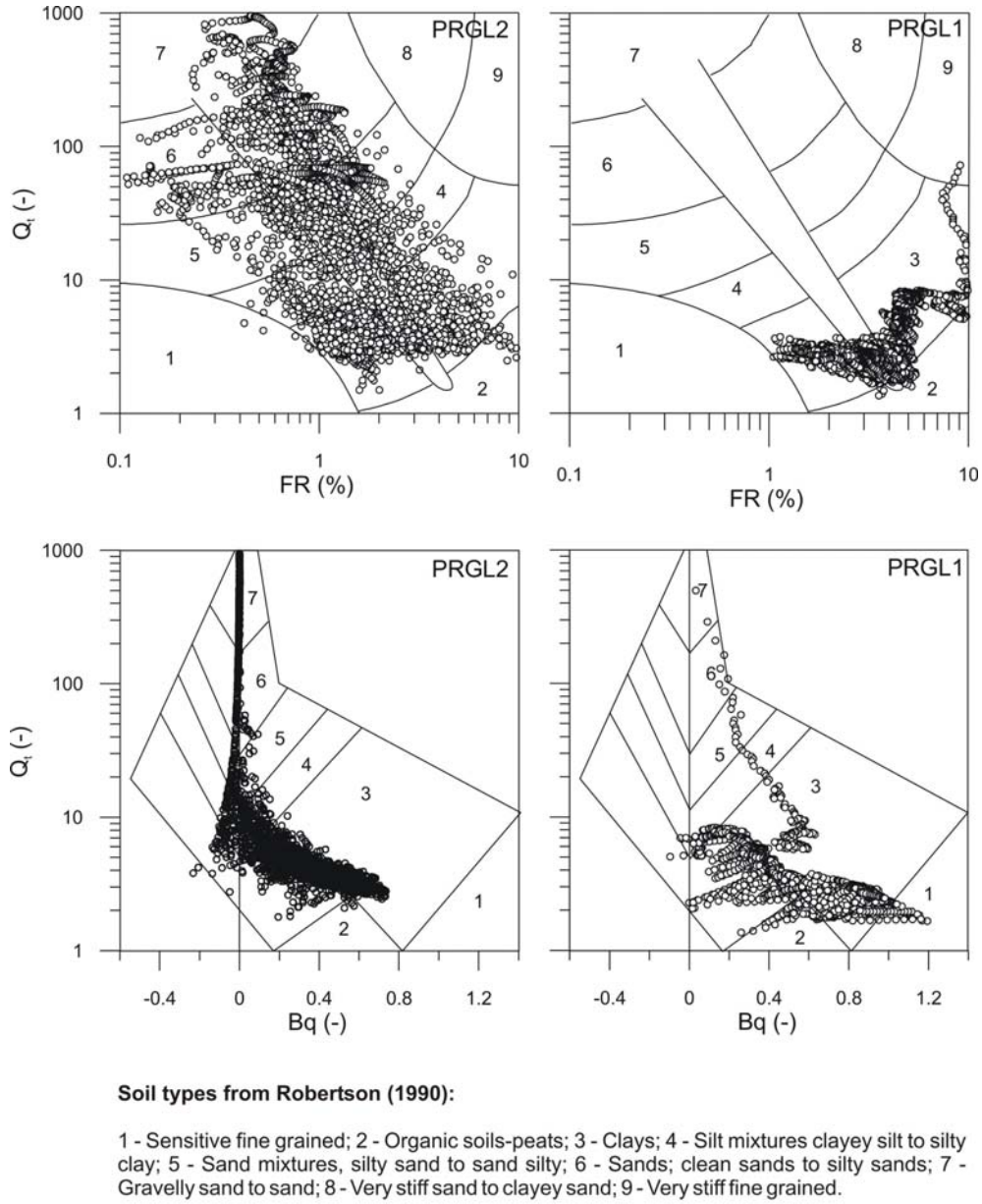

Figure 5.2.2. Soil type classifications for PRGL1 and PRGL2 sites plotted on Robertson's (1990) charts for normalized parameters Q_t, FR and Bq.

the silt dependence of Qt. This, in addition, confirms the 8 µm size as an adequate clay-silt limit for laser grain-size measurements.

5.2.3.2. CPTU tests at PRGL2 site

In PRGL2, five geotechnical-stratigraphic units are identified based on changes in q_c (Fig. 5.2.7) and named 1 to 5 from top to bottom, and subdivided using alphabetically ordered subindexes. q_c and f_s curves are highly similar, with relative high values for sands (from 0 to 28.6 mbsf and from 67 to the borehole bottom) and relative low values in clays (from 28.6 to 68 mbsf and from 78.3 to 82.3 mbsf) (Fig. 5.2.8). Zero u_2 values through the upper 30 meters and negative values at the borehole bottom are attributed to readings in sands affected by cavitation processes (Lunne et al., 1997). Soil types based on the Qt/FR chart from Robertson classification at corresponding depths are also shown in Figure 5.2.7. The good correlation between the sand content profile and Qt/FR profile supports geotechnical stratigraphy for site PRGL2. Geotechnical

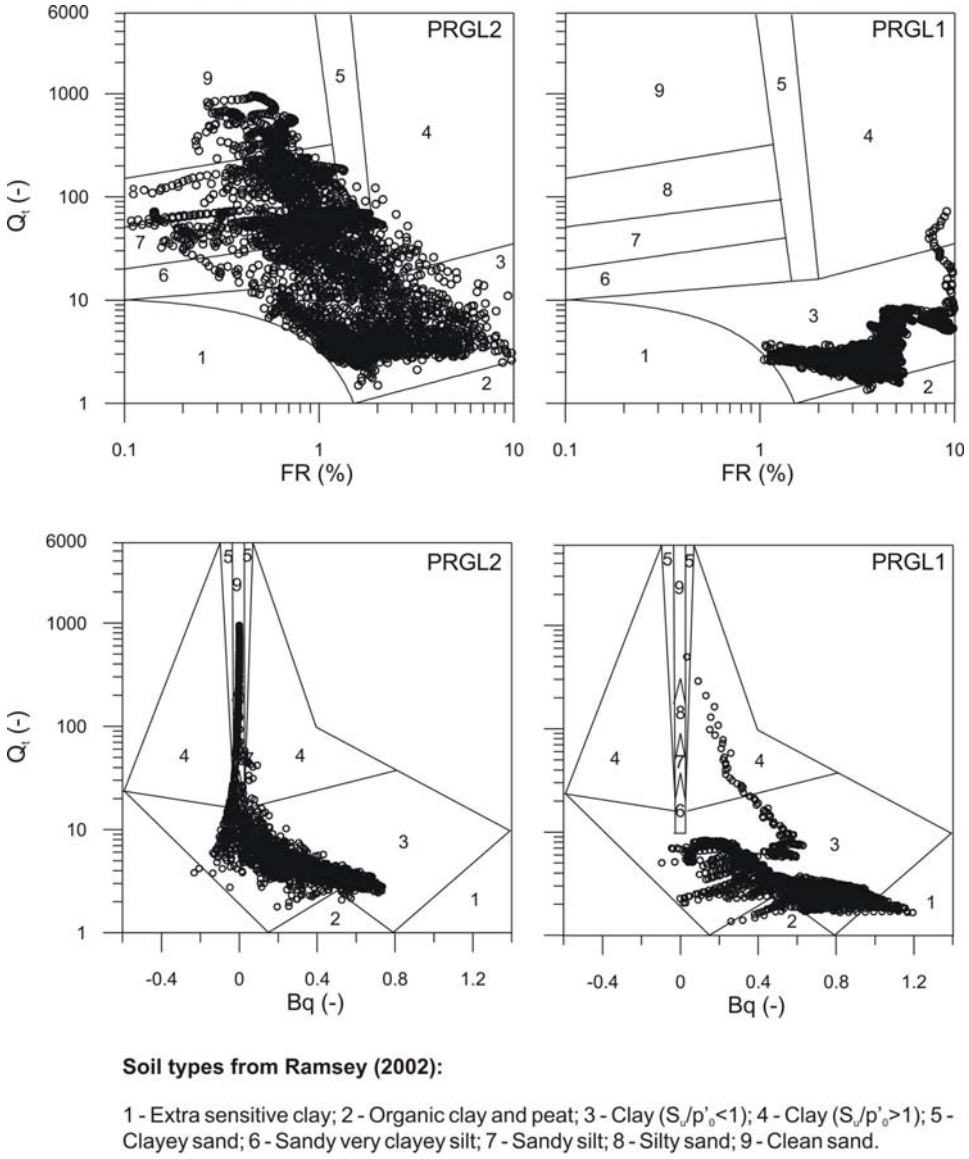

Figure 5.2.3. Soil type classifications for PRGL1 and PRGL2 sites plotted on Ramsey's (2002) charts for normalized parameters Q_t, FR and Bq.

units have been correlated with the lithological units defined for this site by Bassetti et al. (2008) and we found good correlation. However, we grouped these lithological units in five major units for ease of consistency with resistance values whereas the lithological profile identified 14 units (Bassetti et al., 2008). At the borehole bottom (99.24-100.13 mbsf), these authors identify a very coarse clastic unit that we have included in geotechnical subunit 5c.

The soil types interpreted from CPTU classifications (Figs. 5.2.2 and 5.2.3) are highly consistent with the grain size distribution (Fig. 5.2.8). Graded-bedding is identified from q_c at intervals where the sampling resolution from grain size analysis is insufficient to detect them. This is illustrated by the overall coarsening-upwards trend of subunit 1d and the interval comprised by subunits 5b and 5c, and the fining-upwards trend of subunits 4a, 4b and 4c and by subunit 5a. Changes of the fine fraction content, which is made of clayey silts, are well depicted by the 1/Qt profile.

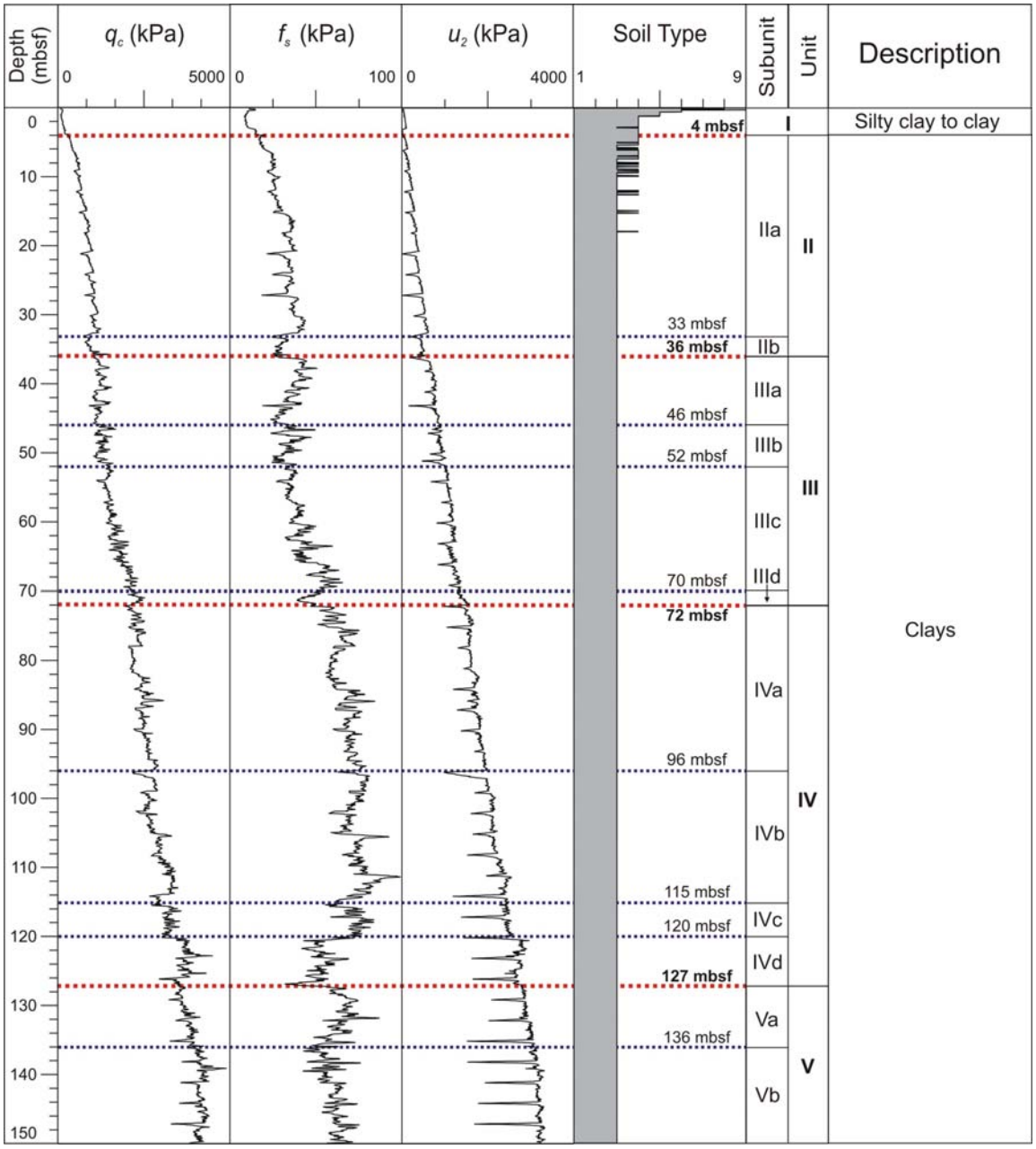

Figure 5.2.4. CPTU profiles from PRGL1_3 borehole. Red dotted lines are unit boundaries that correspond to main seismic discontinuities. Blue dotted lines indicate subunit boundaries. Robertson's (1990) soil types based on Q_t/FR are represented at corresponding depths. Numbers in the soil type scale correspond to those in Figure 5.2.2.

5.2.4. Discussion

5.2.4.1. Soil classification from CPTU measurements

Correlations of grain-size curves with CPTU sediment type classifications at site PRGL1 indicate that the percentage of silts and clays ranges between 40 and 60% along the borehole (Fig. 5.2.4). Units II to V are made of a mixture of silts and clays instead of mainly clays, as suggested by CPTU classifications (Figs. 5.2.2 and 5.2.3). This can be attributed to similar (undrained) piezocone penetration of silts and clays when they occur in similar proportions. In contrast, piezocone testing in sediments with heterogeneous grain-size, where drainage conditions occur (Lunne et al., 1997), as in PRGL2, allows accurate sediment type attribution (Fig. 5.2.7). On the

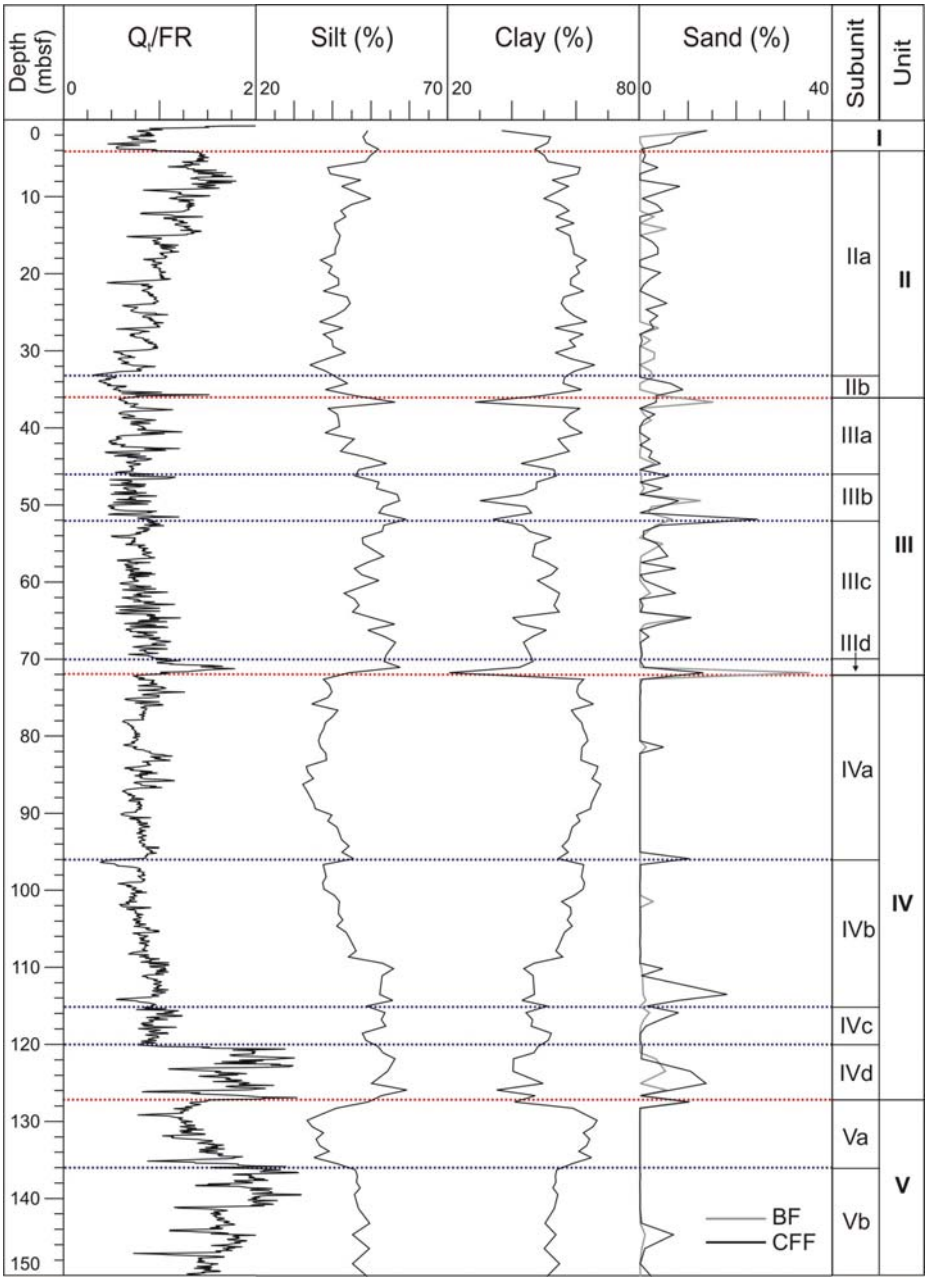

Figure 5.2.5. Correlation between the profile of the ratio Q_t/FR and grain-size distribution profiles from PRGL1. Grain-size analyses were performed at 1:80 cm resolution. Sand contents correspond to both the bulk fraction (BF) and the carbonate free fraction (CFF).

other hand, in deposits where mixtures of cohesionless (silty sands to gravels) sediments are present, as in PRGL2, soil changes are better detected from cone tip resistance, q_c, as it responds more precisely to changes in drainage conditions than sleeve friction, f_s (Fig. 5.2.7).

We have found a good correlation between Robertson's (1990) and Ramsey's (2002) soil classification methods. However, when cavitation occurs, as in PRGL2, the Qt/FR ratio should be used in isolation for soil-type interpretation. Gravelly sands and sands may induce temporary cavitation adjacent to the pore-water pressure sensor location, making the Qt/Bq model unreliable (Ramsey, 2002). For correlating with grain size we, therefore, have used only Robertson's (1990) classification based on Qt/FR (Figs. 5.2.4 and 5.2.7), although the one from Ramsey (2002) can be also considered since both

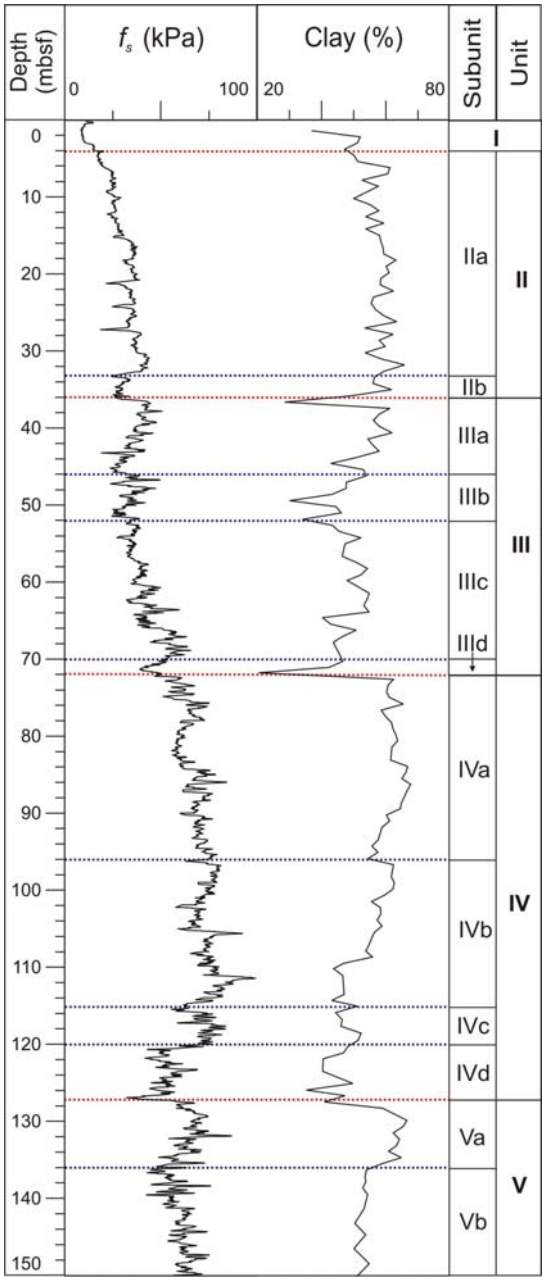

Figure 5.2.6. Correlation between the sleeve friction f_s profile and the clay content from PRGL1.

classifications identify the same soil types (Figs. 5.2.2 and 5.2.3).

Water pressures generate significant values of cone resistance and pore pressure, which are corrected to zero at seafloor. In down-hole CPTU systems, the pressure conditions in the drill pipe may not be in full equilibrium with the surrounding ground water pressure. Consequently, zero-correction can be subject to increased uncertainty that is in the order of 100 kPa (Peuchen, 2000). The uncertainty for the zero-correction of the cone tip resistance is approximately equivalent to a factor representing the net area ratio effect, which is 0.75 for the data presented herein. The zero drift of the measured q_c and u_2 is considered to be within the allowable minimum accuracy according the accuracy class selected by Fugro, following standardized practice (ISSMGE, 1999). Therefore, we consider irrelevant the uncertainty of the derived parameters used for soil classification.

5.*2.4.2. Stratigraphic profiling from CPTU profiles*

The transition from one layer to another is not necessarily registered as a sharp change in cone tip resistance, q_c (Lunne et al., 1997). Recent numerical analyses show that q_c in a dense sandy layer embedded in soft clays is less than its true value when the thickness of the sand layer is less than 28 cone diameters (Ahmadi and Robertson, 2005), i.e. >1 m for the cone used in our study. In contrast, for a very loose sand layer under moderate stress states (effective vertical stress ≥ 70 kPa) the layer should be more than eight cone diameters, i.e. >0.3 m for our study. The lower thickness of sand layers identified at PRGL2, which is 1.5 m in subunit 1c (Fig. 5.2.7), is slightly above the 0.3-1 m cone accuracy.

Some authors (Robertson, 1990, Lunne et al., 1997) consider that the sleeve friction, f_s, is less accurate than the cone tip resistance qc and that the pore pressure u_2 measurements since f_s measures average values over the sleeve length (13 cm in our case), which tends to smooth out the record of thin layers. However, we found f_s to be the most accurate CPTU parameter for profiling the sediments at PRGL1 site, as demonstrated by its correlation with the clay content (Fig. 5.2.6). The stratigraphic profile based on f_s is further supported by the Qt/FR profile, which proves that f_s variations are, at this site,

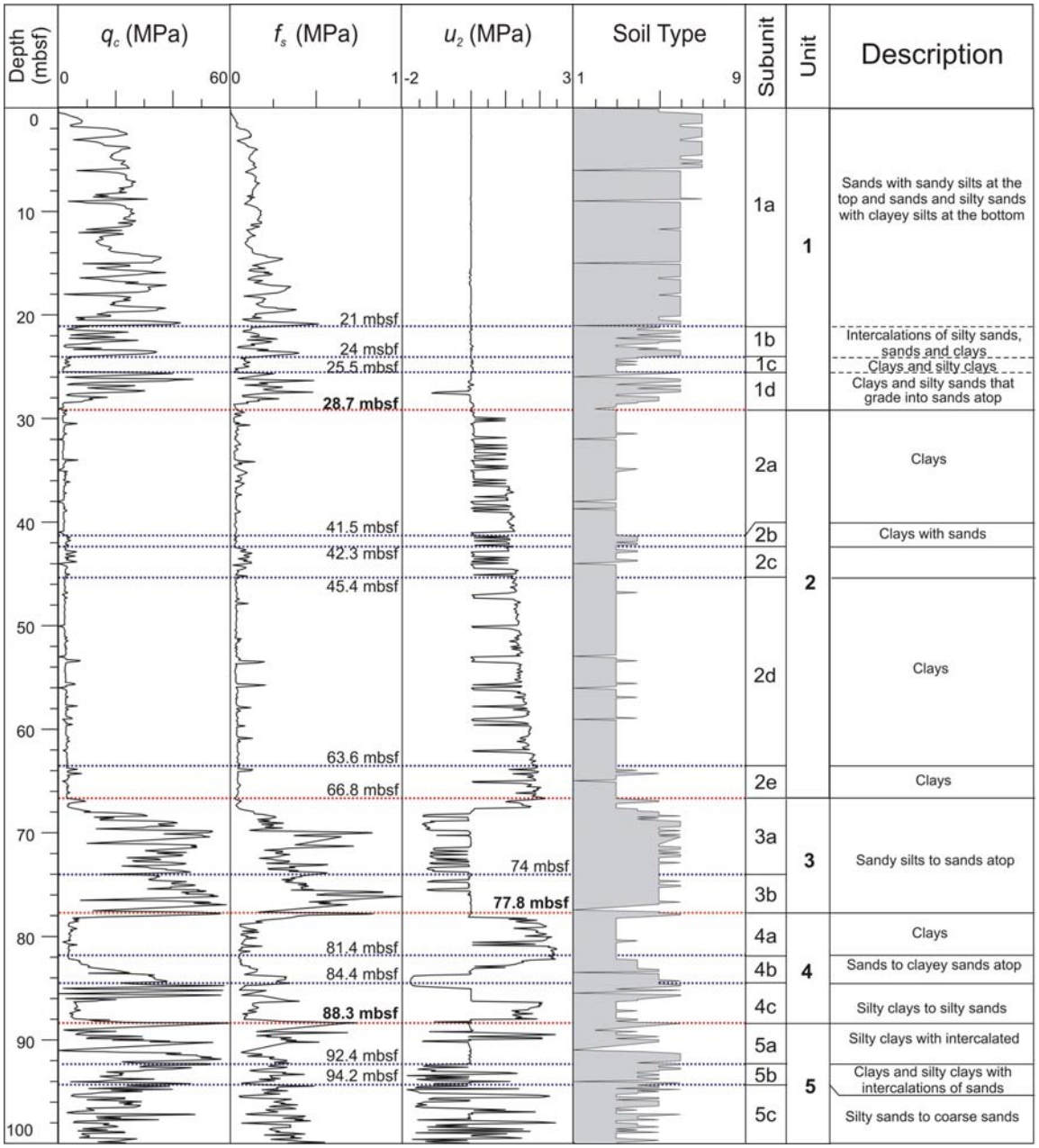

Figure 5.2.7. CPTU profiles from PRGL2_1 borehole. Red dotted lines are unit boundaries that correspond to main seismic discontinuities. Blue dotted lines indicate subunit boundaries. Soil types are based on the Q_t/FR chart from Robertson's (1990). Numbers in the soil type scale correspond to those in Figure 5.2.2.

caused by changes in the cohesion that are directly related to the clay content.

5.2.4.3. Correlation between CPTU based geotechnical stratigraphy and high resolution seismic reflection profiles

At site PRGL2, lithological and geotechnical subunits 1a to 1d correspond to the upper shoreface sands of the seismic unit U152 (Fig. 5.2.9a, Bassetti et al., 2008). Our sandy Unit 1 is bounded by a submarine erosion surface D65 atop of the geotechnical Unit 2. Subunits 2a and 2b, separated by discontinuity D64, display clays with intercalations of silty clays of a lower shoreface and correspond to the seismic unit U151 (Fig. 5.2.10a). The top of the silty clayey subunit 2c, which is characterized by a slight increase in q_c and f_s, corresponds to combined discontinuity D60-D63, which separates seismic sequence S5 (formed here by U152 and U151) from S4.

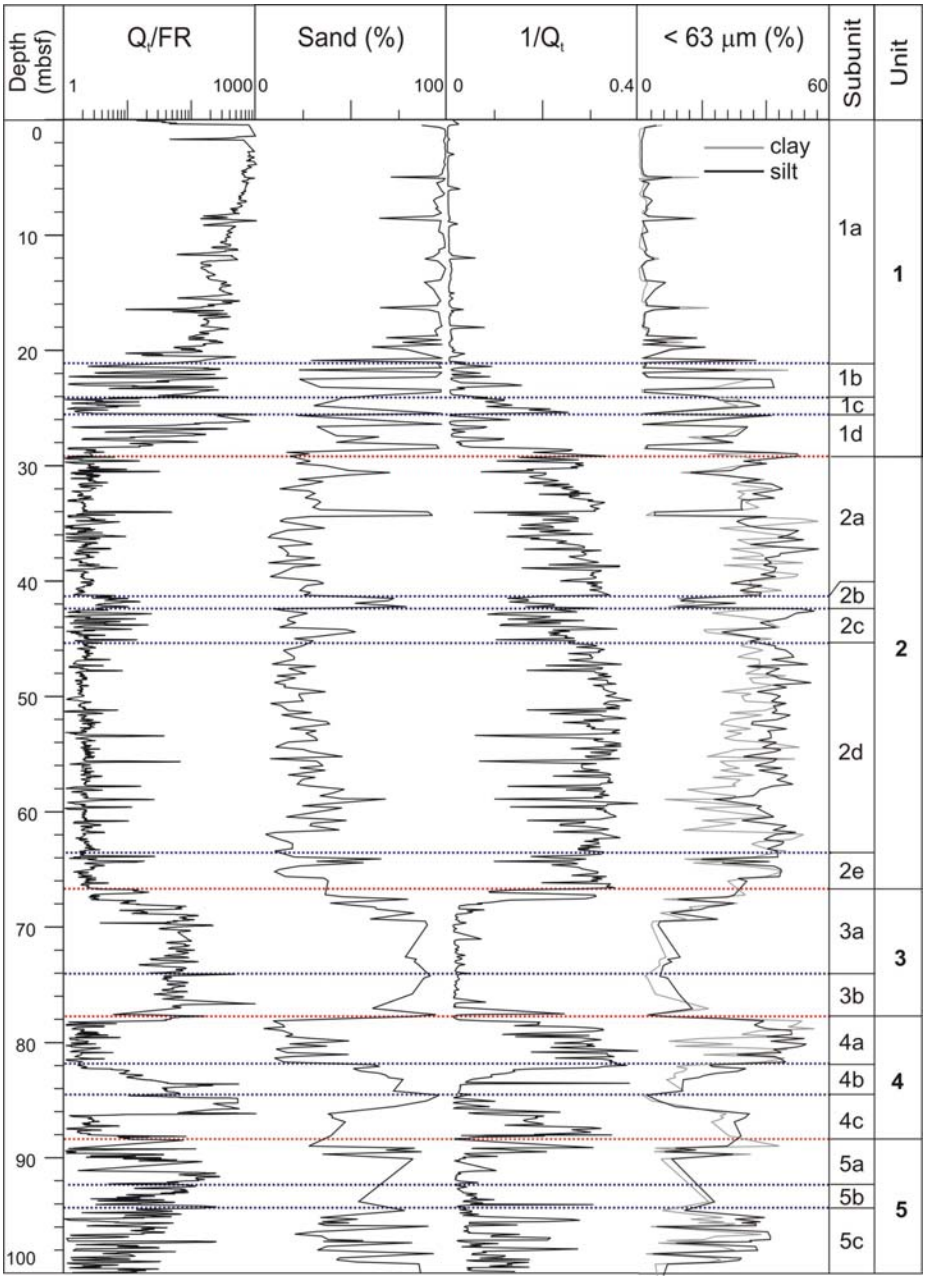

Figure 5.2.8. Correlation between profiles of the ratio Q_t/FR and 1/Q_t and grain-size distribution profiles from PRGL2. Grain-size analyses were performed at 1:20 cm resolution in muddy sections and at 1:80 cm in cohesionless sandy sections.

D63 is an erosion surface attributed to a drop of sea-level during the overall sea-level fall between Marine Isotope Stage (MIS) 3 and MIS 2 (Jouet et al., 2006, Bassetti et al., 2008). Clays in our subunits 2d and 2e correspond to the distal part of seismic sequence S4. The sandy Unit 3 corresponds to foreshore-upper shoreface deposits that, in conjunction with the clayey subunit 4a forms seismic unit S3. The underlying fining upwards subunit 4b constitutes seismic unit S2. The top of Unit 3 corresponds to seismic discontinuity D50 and the base of subunit 4b corresponds to the combined surfaces D45-D40-D35. Nevertheless, the three coarse-grained intervals represented by positive peaks of qc could be linked to D45-D40-D35. Although their thickness (<1m) is slightly below the 0.3-1 m cone accuracy (Fig. 5.2.10a) and it does not allow them to be distinguished on seismic profiles, we consider these three discontinuities are closely spaced

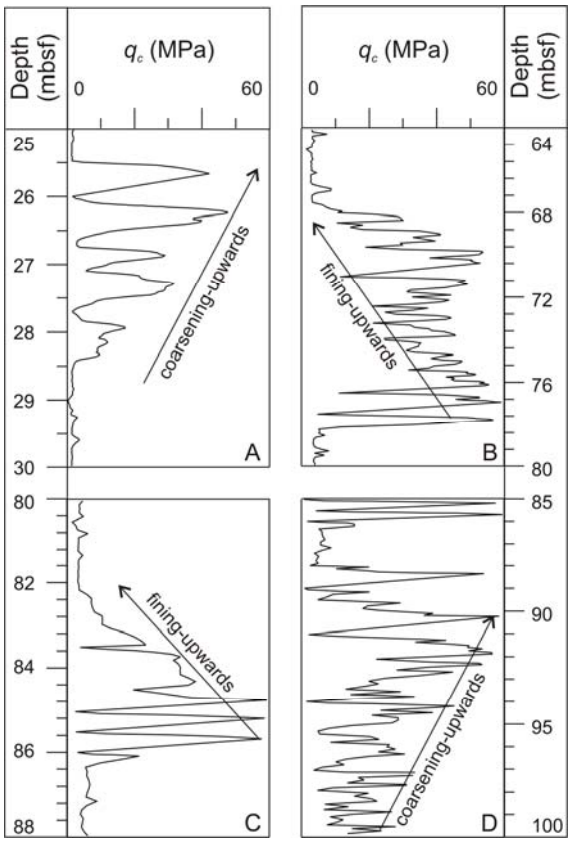

Figure 5.2.9. Grain size trends at PRGL2 interpreted from cone tip resistance q_c trends. A: coarsening-upwards sequence at subunit 1d; B: fining-upwards sequence at unit 7; C: fining-upwards sequence at subunits 4c, 4b and 4a; and D: coarsening-upwards sequence at subunits 5c and 5b.

but distinct on the basis of q_c profile. 5a is separated from the coarsening upwards subunits 5b and 5c by discontinuity D30, which is at the base of seismic sequence S0.

At the much more lithologically homogeneous site PRGL1, we found a likely correspondence amongst units I to III and IV with seismic sequences S5 and S4, respectively (Fig. 5.2.10b). Subunits IIb (from 33 to 36 mbsf), IIId (70-72 mbsf) and IVd (120-127 mbsf) comprise the reflectors corresponding to discontinuities D63, D60 and D50, which are found to represent intervals of variable thickness characterized by low friction measurements due to increased sand content (Figs. 5.2.5 and 5.2.6). The lower Unit V corresponds to S3. The rest of the boundaries between our CPTU based subunits do correspond to specific seismic reflectors, which are seen to separate different seismic facies: subunits IIa and IIIc correspond to low amplitude hemi-stratified facies; IIIb, IVa, IVb, Va and Vb to facies of intermediate amplitude; and IIIa, IIIb and IVc to facies of higher relative amplitude. Such changes in relative amplitude in the seismic record do correlate well with the CPTU based geotechnical-stratigraphic divisions.

5.2.5. Conclusions

The piezocone (CPTU) is a widely accepted soil classification test routinely used by geotechnical engineers. However, CPTU soil classification charts have to be used with extreme care when dealing with mixtures of marine silts and clays in similar proportions. The (undrained) behavior of these admixtures is the same as (undrained) pure clays and, consequently, they could be erroneously classified as clays. Combined normalized tip resistance Qt and friction ratio FR profiles are very useful to identify grain-size trends in these sediment types and verify soil type classification results.

The comparison of CPTU profiles with grain-size data and high resolution seismic reflection profiles has demonstrated that amongst the various CPTU parameters, sleeve friction is convenient for profiling fine-grained sediments, such as those found at PRGL1 site, whereas cone tip resistance proves to be the best suited parameter in heterogeneous sequences with coarse and fine-grained sediments as at PRGL2 site. The ratio of the normalized tip resistance vs friction ratio Qt/FR has proved to be also suitable for identifying soil stratigraphy.

From the case study presented herein we conclude that in situ piezocone tests are a useful tool to interpolate and extrapolate the stratigraphic profile and the soil classification on the basis of grain-size and/or seismic reflection data. The drawbacks found in the prediction of fine-grained deposits illustrate the need to further investigate soil classification methods in these sediment types.

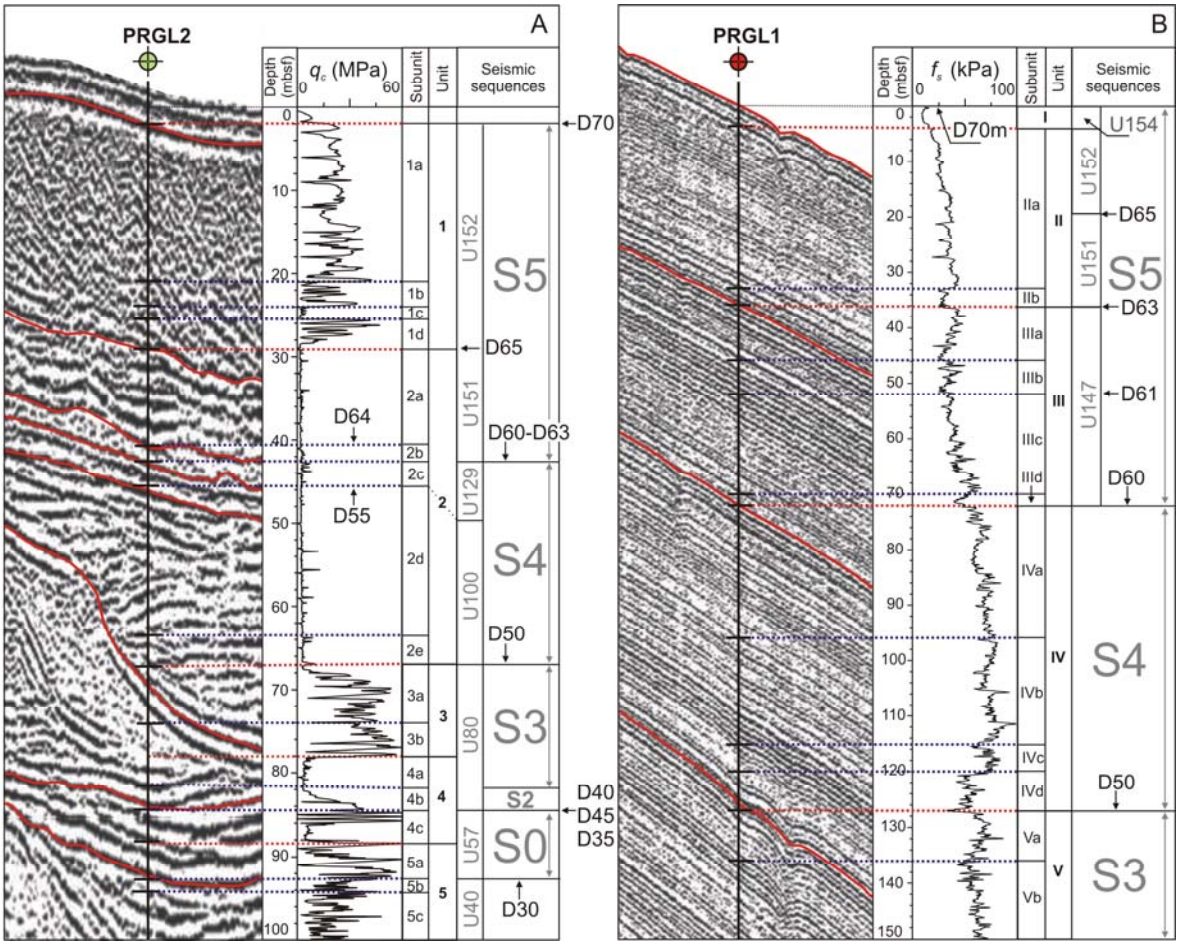

Figure 5.2.10. Correlation between CPTU based geotechnical stratigraphy and seismic reflection stratigraphy at PRGL1 and PRGL2 sites. A: CPTU-seismic reflection data correlation at site PRGL2 and B: CPTU-seismic reflection data correlation at site PRGL1.

Acknowledgements

The authors thank the EC PROMESS1 project (contract num. EVR1-CT-2002-40024). The onboard scientific party of the project has been involved in the gathering of the data and their input is very much appreciated. We thank G. Herrera (Universitat de Barcelona) for grain size analyses and E. Thereau (Ifremer) for processing the seismic data. We also acknowledge all other researchers and technicians from PROMESS1 partner institutions that have contributed in different ways to this research. Associate Editor as well as G. Verdiccio and an anonymous reviewer are thanked for their review of the manuscript. S. Lafuerza benefits from a PhD research grant by the Spanish Ministry for Education and Science. GRC Geociències Marines is funded by Generalitat de Catalunya research grants program to high quality scientific groups (ref. 2005 SGR-00152).

5.3. Overpressure within upper continental slope sediments from CPTU data, Gulf of Lion, NW Mediterranean Sea

S. Lafuerza (1), N. Sultan (2), M. Canals (1), J. Frigola (1), S. Berné (3), G. Jouet (2), M. Galavazi (4), F.J. Sierro (5)

(1) GRC Geociències Marines, Departament d'Estratigrafia, Paleontologia i Geociències Marines, Universitat de Barcelona, Spain
(2) Institut Français de Recherche pour l'Exploitation de la Mer, France
(3) IMAGES, Université de Perpignan Via Domitia, France
(4) Fugro Engineers B.V., The Netherlands
(5) Departamento de Geología, Universidad de Salamanca, Spain

Abstract

Data from in situ piezocone tests (CPTU) and laboratory analyses are utilized for the interpretation of the stress history of Quaternary sedimentary sequences in the upper continental slope of the Gulf of Lion, northwestern Mediterranean Sea. A CPTU based preconsolidation pressure profile referenced to the current effective stress indicates that the deposit is underconsolidated from 12 meters below the seafloor (mbsf) down to at least 150 mbsf. Excess pore pressure below 12 mbsf is further supported by results from oedometer and dissipation tests. Subseafloor pockmarks and indications of free gas in seismic reflection profiles reveal four main overpressure sources (SI-SIV) with overpressure ratios > 0.3 at subseafloor depths coinciding with levels where the dominantly silty-clayey sediment contains increased proportions of sand. We relate the excess pore pressure related to free gas due to gas exsolution processes and sea level variations driven by Pleistocene sea level changes.

Keywords: stress history, preconsolidation pressure, overpressure, continental slope, Gulf of Lion

2009, International Journal of Earth Sciences (Geol Rundsch), Vol. 98, p. 751-768.
Doi: 10.1007/s00531-008-0376-2

5.3.1. Introduction

Fine-grained sediments such as those occurring in continental slope sequences are particularly prone to develop overpressure (pore fluid pressure in excess of hydrostatic pressure) as they usually exhibit low permeabilities (Bolton et al. 1998). Overpressure drives fluids along permeability pathways and the resulting fluid flow can lower the effective stress of the sediment thus favouring its failure (Dugan et al. 2003; Canals et al. 2004a).

Excess pore pressure (Δu) can be estimated from the difference between the current vertical effective stress (σ'_{v0}) and the preconsolidation pressure (σ'_p) as expressed by:

$$\Delta u = \sigma'_{v0} - \sigma'_p$$

The vertical effective stress σ'_{v0} is defined as the difference between the total vertical stress (σ_{v0}) and the pore fluid pressure that, considering hydrostatic conditions (u_h), is $\rho_w \gamma$ z. The preconsolidation pressure is the highest pressure the deposit (or soil) has ever been submitted. While it is normally interpreted on the basis of oedometer tests it can be also estimated from in situ tests. Laboratory oedometer consolidation tests are usually conducted on small samples assumed to be undisturbed. However, almost all recovered samples have some degree of disturbance (Grozic et al. 2003; Lunne et al. 2006) and, consequently, the laboratory-derived strength and consolidation parameters may not be entirely representative of the in situ soil conditions. In situ tests are performed under existing stresses and boundary conditions in the field, providing more accurate and reliable results than laboratory tests.

The piezocone test (CPTU) is now the most widely used in situ test for the geotechnical characterization of marine sediments in deepwater. CPTU involves the measurement of the resistance and friction of sediments to steady and continuous penetration of a piezocone penetrometer equipped with sensors for cone tip resistance (q_c), sleeve friction (f_s) and pore pressure (u). These are the three direct CPTU parameters that are recorded continuously with depth during in situ CPTU testing. The near continuous information provided by CPTU direct and derived parameters, as the corrected cone resistance (q_t), is utilized to predict the nature of subseafloor sedimentary sequences and geotechnical properties (Lunne et al. 1997). In particular, several empirical formulas allow determining the preconsolidation pressure based on piezocone measurements (Lunne et al. 1997). Some studies have shown the reliability of obtaining the preconsolidation pressure s'p for a wide range of clays from the net tip resistance (q_{net}) (see Appendix A) and the parameter $N_{\sigma t}$, which relates the corrected cone resistance q_t and the vertical effective stress σ'_{v0} to the preconsolidation pressure σ'_p (Demers and Leroueil 2002; see Appendix B).

This paper deals with the CPTU characterization of a 150 m thick sedimentary sequence from the upper continental slope in the Gulf of Lion, northwestern Mediterranean Sea. The aim of this work is to exploit preconsolidation pressure σ'_p data derived from in sit CPTU tests in order to establish the links between the stress history of such sedimentary sequence and the geological processes that determined its development. The study site was selected on the basis of high resolution seismic reflection data in the fluvial-dominated continental slope of the Gulf of Lion, which holds a continuous sediment record of at least the last 500 kyr (PROMESS1 research project unpublished results; see Sections 5.3.2 and 5.3.3)

5.3.2. Study area

5.3.2.1. Geological setting

The Gulf of Lion passive continental margin includes the widest (70 km) continental shelf in the western Mediterranean Sea with the shelf edge at a mean depth of 135 m. The continental slope is dissected by an intricate network of 100-150 km long submarine canyons feeding base-of-slope and rise thick sediment bodies such as the Rhône Deep Sea Fan and the Pyrenean Canyon Deep Sediment Body (Alonso et al. 1991; Berné et al. 1999; Canals 1985; Canals et al. 2004b; dos Reis 2005; Droz 1983; Medimap Group 2005). Canyon heads and upper courses are cut into the continental shelf and are separated by interfluves (or inter-canyon areas) that are assumed to hold the most continuous, high resolution sedimentary sequences of Quaternary age in the Gulf of Lion's slope. The main sediment source in the study area, accounting for shelf, slope and rise outbuilding, is the Rhône River, with minor inputs from other rivers along the shores of the Gulf of Lion (UNEP/MAP/MED POL 2003).

Outer shelf Quaternary sequences are characterized on seismic reflection profiles by alternating steep and low angle clinoforms that correspond, respectively, to high energy (sand) and low energy (silt) sediments formed during glacial and interglacial cycles (Aloisi 1986; Bassetti et al. 2006; Berné et al. 1999 and 2004; Jouet et al. 2006; Rabineau et al. 2005; Tesson et al. 2000). Such outer shelf clinoforms have been attributed to sandy shoreface and muddy offshore deposits, respectively (Berné and Gorini 2005), and related to 100 kyr glacio-eustatic cycles (Rabineau et al. 2005). Seaward, along the upper slope interfluves, outer shelf erosional surfaces created during low stands of the sea become correlative conformities, shelf sequences get thicker due to higher accommodation space, and sediment grain size is finer. These fine-grained sedimentary sequences may destabilise under the influence of external triggers (Sultan et al. 2004 and 2007a).

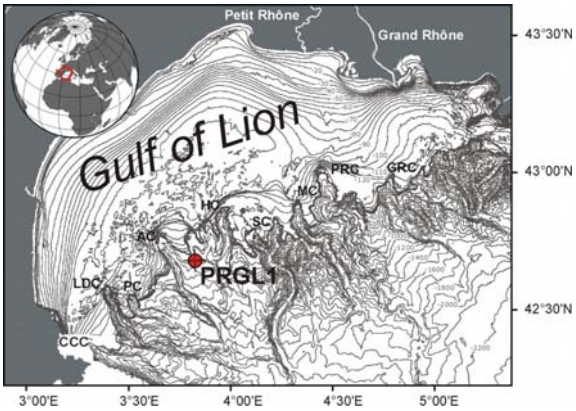

Figure 5.3.1. Location of the PRGL1 site. CCC, Cap de Creus Canyon; LDC, Lacaze-Duthiers Canyon; PC, Pruvot Canyon; AC, Aude Canyon; HC, Hérault Canyon; SC, Sète Canyon; MC, Montpellier Canyon; PRC, Petit Rhône Canyon; GRC, Grand Rhône Canyon. Bathymetry in meters from Berné et al. (2001) and Medimap Group (2005). 100 m contour equidistance unless otherwise indicated. Names after Canals (1985).

5.3.2.2. Site description

The drilling site PRGL1 was located at 42º41'23.30''N and 003º50'15.50''E, at 298 m of water depth, on the uppermost part of the interfluve separating the Aude (or Bourcart) and Hérault submarine canyons, in the western half of the Gulf of Lion, 12 miles off the shelf edge that locally lies at 200 m depth (Fig. 5.3.1).

Preliminary chronostratigraphic and sedimentological data from borehole PRGL1_4 (Frigola et al. 2005; see Section 5.3.3 below) showed that the drill went through a Pleistocene sedimentary package made of silts and clays in variable proportions with some intercalated sand-bearing layers. Micropaleontological studies at this same site have revealed that the sand-bearing layers contain abundant coarse-grained planktic foraminifera and that they represent condensation levels (Sierro et al. 2005 and 2006). On the basis of seismic velocity analyses, the correlation between seismic reflection profiles crossing the PRGL1 site and borehole data suggests that the main seismic sequences, related to 100 kyr cycles, are bounded by seismic amplitude anomalies

caused by the above mentioned condensed layers (Berné et al. 2006)

5.3.3. Materials and methods

5.3.3.1. Borehole information

CPTU in situ testing and drilling of site PRGL1 were made from SRV Bavenit, operated by Fugro Engineers B.V., as part of the EC funded "PROfiles across MEditerranean Sedimentary Systems 1" (PROMESS1) research project. Five boreholes were drilled at site PRGL1 that were named PRGL1_1 to PRGL1_5. Of these, PRGL1_3, PRGL1_4 and PRGL1_5 have been used for this study (Table 5.3.1). CPTU measurements down to 150 mbsf and in situ dissipation tests at four depths were performed in-hole at PRGL1_3. Following sediment coring, downhole logging was done at PRGL1_4 down to 301 mbsf. Sediment samples from PRGL1_4 have been analyzed for grain size and biostratigraphy. Continuous coring for geotechnical purposes was made at PRGL1_5 down to 126.4 mbsf with >95% recovery (Table 5.3.1).

5.3.3.2. In situ measurements

The CPTU testing technique utilized in our study consists of pushing down the piezocone penetrometer from the seafloor to the targeted subseafloor depth by steps (each implying an individual CPTU test) within the drill hole. The pushing equipment was made of a downhole WISON CPT with a 3 m stroke downhole jacking unit and a thrust capacity of 90 kN. During testing, the WISON CPT is lowered by its umbilical wire to the drill bit level, where it seats and latches into the seating subassembly or seabed frame (Fig. 5.3.2a). The tool is then hydraulically pushed down at a constant rate of 2 $cm \cdot s^{-1}$. Upon reaching the maximum stroke of 3 m or the 90 kN thrust capacity, the test is finished and the system depressurized. Successive 3 m long tests allow completing the CPTU profile down to the target depth.

The piezocone penetrometer used in this study is a relatively small instrument with a diameter of 36 mm, a cross-sectional area of 1000 mm^2, 60º tip apex angle and a 13 cm sleeve (Fig. 5.3.2b). q_c and f_s (see Section 5.3.1) are measured on two electrical strain-gauge load cells located inside the sleeve (Fig. 5.3.2c). The piezocone penetrometer applied to our study uses a so-called subtraction load-cell arrangement, which allows measurements of the axial forces on the cone and the friction sleeve by compression of two internal strain-gauge load cells. The load cells are in series so that the lower load cell measures q_c and the upper load cell measures q_c and f_s. Therefore, f_s is obtained by subtracting q_c from the measure by the upper load cell. The pore pressure u can be measured at different locations throughout the piezocone penetrometer: at the cone, u_1, behind the cone, u_2, and behind the sleeve friction sensor, u_3. Pore pressure measurements presented in this paper correspond to u_2 (Fig. 5.3.2b) as this location usually provides good stratigraphic detail and dissipation data (Lunne et al. 1997). q_c, f_s and u_2 profiles run at PRGL1_3 borehole are shown in Figure 5.3.3.

In situ tests yielded preconsolidation pressure and excess pore pressure data. The direct relationship between the preconsolidation pressure σ'_p, through the Nst parameter (see Section 5.3.1 and Equation 5 in Appendix B) following Demers and Leroueil (2002), and the net tip

Borehole	Performance	Water depth (mbsf)	Borehole depth (m)
PRGL1_3	CPTU (Dissipation tests at 11.7, 32.6, 59.9 and 125.9 mbsf)	298	150.0
PRGL1_4	Sedimentological sampling and downhole logging	298	301.0
PRGL1_5	Geotechnical sampling	298	126.4

Table 5.3.1. PRGL1 site boreholes general information.

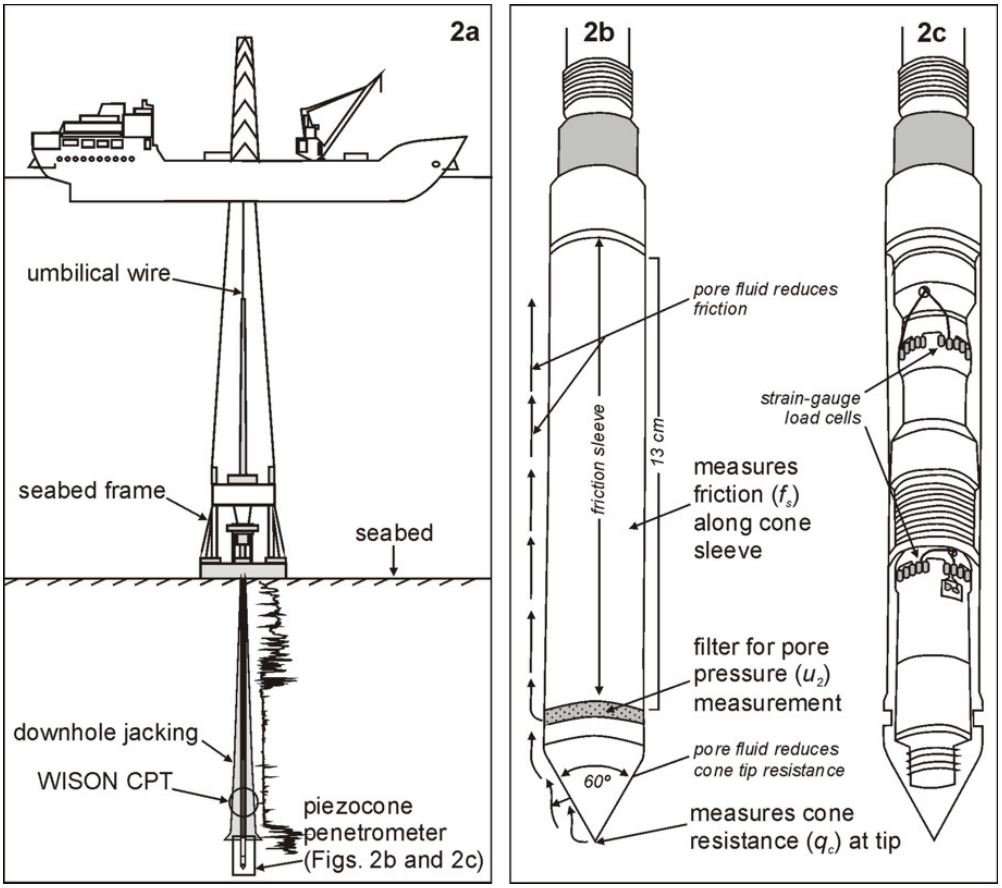

Figure 5.3.2. The piezocone penetrometer. Figure a illustrates CPT/CPTU deployment from a drilling vessel in deep water. Figure b shows where cone tip resistance, q_c, sleeve friction, f_s and excess pore pressure, u, are measured. The filter used in the present study for u measurements is located behind the cone tip, u_2. Figure c illustrates the location of the strain-gauge load cells that measure f_s and q_c altogether.

resistance q_{net}, derived from the piezocone tests (see Equation 2 in Appendix A), provided the stress history of PRGL1 site. Continuous P-wave (Vp) measurements were performed by downhole logging at borehole PRGL1_4. The resulting data have been used for estimating a Vp based continuous excess pore pressure profile (see Appendix C). The equilibrium pore pressure has been estimated from in-hole dissipation tests at PRGL1_5 at 11.7, 32.6, 59.9 and 125.9 mbsf (see Appendix C; see Section 5.3.4.3 for details).

5.3.3.3. Laboratory tests and age model

Of the various laboratory geotechnical tests made on samples from PRGL1 (Sultan et al. 2007), we have used the results of six oedometer tests performed on PRGL1_5 samples (see Section 5.3.4.1). Time between load increments was 24 hours, the size of the cell 50 mm and the initial height of the sample 20 mm. Oedometer tests were conducted according to the ASTM D-2435 method (ASTM 1993). Sand contents have been determined from bulk and carbonate free sediment fractions (BF and CFF, respectively) of 168 samples (Frigola et al. 2005; see Appendix A.2).

The coarse-grained planktic foraminifera and other sand-size particles, which compose the condensed layers, have been used to calibrate our record to global climatic records. This resulted in an inferred age model (Table 5.3.2) based on the assumption that coarse-grained condensed units formed at times of rapid sea level rises during global melt-water events, when sediment supply to the upper slope decreased suddenly as a consequence of the flooding of the

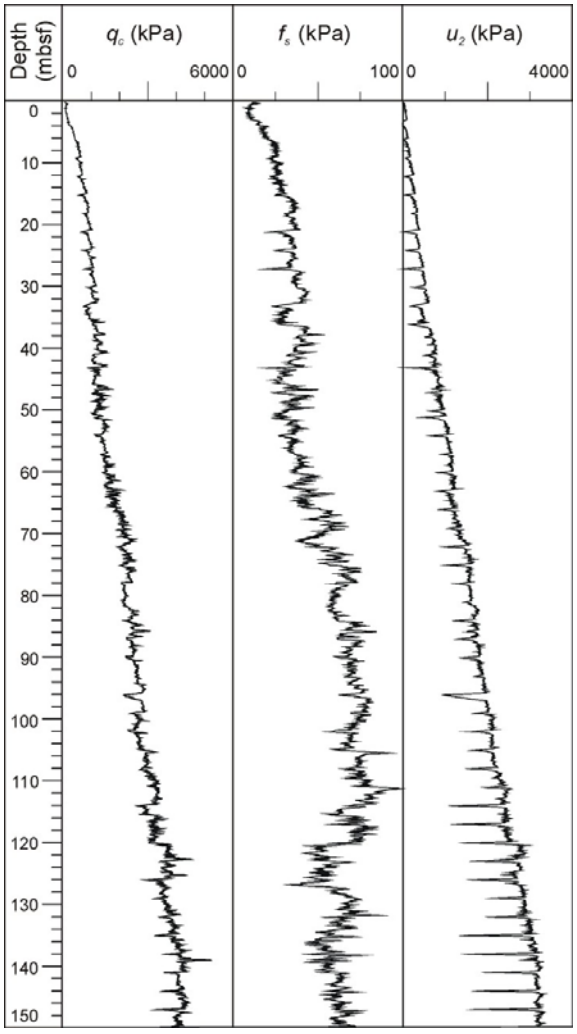

Figure 5.3.3. Preconsolidation pressure from oedometer tests as derived from Casagrande's (σ'_{pa}) and Onitsuka's (σ'_{pb}) methods, respectively.

continental shelf. These melt water events occurred in phase with the longest and warmest Greenland interstadials of the last 300 kyr at least (Sierro et al. 2005 and 2006). Such an inferred age model (Table 5.3.2) is considered accurate enough for the purposes of this paper, and it has been used to calculate average sedimentation rates (Dennielou et al. 2006).

5.3.3.4. Borehole-seismic data correlation

The vertical positions of data from CPTU and laboratory analyses on seismic reflection profiles have been calculated using MSCL gamma-density shaped P-wave velocities calibrated by interval seismic velocity analysis from in situ measurements in order to

Table 5.3.2. Inferred age model for PRGL1_4 borehole obtained with the AnalySeries Version 1.1 (Paillard et al., 1996) on the basis of a preliminary age model from Sierro et al. (2006). Values have been rounded to the first decimal wherever needed. See details in main text (Section 5.3.3.3).

Depth (mbsf)	Age (kyr)*
0.1	14.5
6.6	17.5
21.0	24.0
29.6	29.0
31.5	30.6
35.7	35.3
36.7	38.4
42.3	42.6
44.6	45.5
47.5	47.2
49.6	52.1
53.6	58.2
58.6	61.9
64.4	68.6
65.2	73.0
65.4	82.0
68.4	102.0
72.0	125.0
117.6	198.0
123.5	221.0
127.5	243.0
160.0	336.0

convert the meter below sea floor (mbsf) scale from borehole measurements and coring into the millisecond two-way travel time (mstwtt) scale of the seismic reflection profiles. The seismic data were acquired during the "Marion" cruise in year 2000 aboard R/V *Le Suroît*. A 24-channel, 300 m long high resolution streamer was used, together with a cluster of mini-GI and GI-guns. The seismic section used in this study corresponds to an amplitude processed multi-channel high-resolution seismic line.

5.3.4. Results

5.3.4.1. σ'_p from laboratory tests

Preconsolidation pressures σ'_p obtained following Casagrande's (1936) and Onitsuka's (in Grozic et al. 2003) methods (Figs. 5.3.4a and 5.3.4b) are shown in Table 5.3.3, where they are labelled σ'_{pa} and σ'_{pb}, respectively. Of these we give more relevance to σ'_{pb} based on Onitsuka's method, which is easier to apply than the Casagrande's one (Grozic et al. 2003). Figure 5.3.4c shows oedometer results obtained from six PRGL1_5 samples (see Section 5.3.3.3) named, from shallower

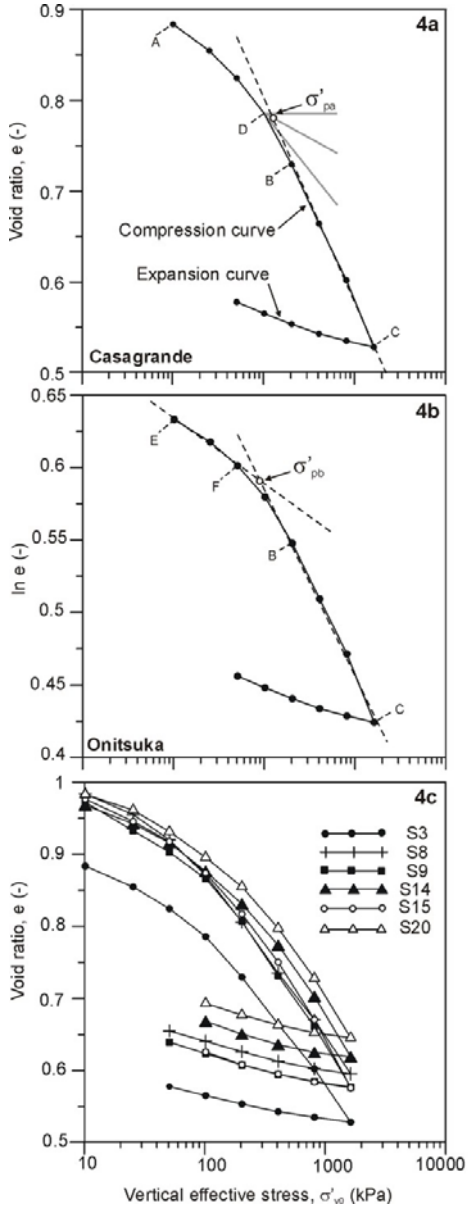

Figure 5.3.4. Estimation of preconsolidation pressure and results from oedometer tests. Figure 4a illustrates the Casagrande's method for obtaining the preconsolidation pressure (σ'_{pa}). The calculation of σ'_{pa} comprises the following steps: (1) construction of the straight-line part (BC) of the curve, (2) determination of the point D of maximum curvature on the recompression part (AB) of the curve, (3) drawing the tangent to the curve at D and bisect the angle between the tangent and the horizontal through D, and (4) drawing the line through the point of intersection of the bisector and CB. Figure 4b displays the bi-logarithmic method of Onitsuka for obtaining σ'_{pc}, based on the intersection of the straight-line BC and the straight -line EF. Figure 4c shows the curves obtained from the six oedometer tests on samples S3, S8, S9, S14, S15 and S20 (see Tables 5.3.3 and 5.3.5).

to deeper, S3, S8, S9, S14, S15 and S20. Calculated σ'_{pb} values increase with depth, from 90 kPa at 4.3 mbsf (sample S3) to 198 kPa at 45 mbsf (sample S20) (Table 5.3.3).

5.3.4.2. σ'_p from piezocone measurements

Following the approach described in Appendix B to calculate a continuous σ'_p profile based on piezocone data, six $N_{\sigma t}$ points were calculated from σ'_{pb}, which are 3.4, 5.6, 6.9, 5.9, 4.6 and 4.5 for S3, S8, S9, S14, S15 and S20, respectively. These $N_{\sigma t}$ values combined with grain size distributions allow subdividing the sediment column into 9 intervals in a way that changes in $N_{\sigma t}$ relate to soil type changes (Table 5.3.4). $N_{\sigma t}$ values from σ'_{pb} range from 3.4 to 6.9 (Table 5.3.4), which are consistent with those published by Lunne et al. (1997) and Demers and Leroueil (2002). $N_{\sigma t}$ values in Table 5.3.4 have been used to calculate a continuous σ'_p profile (Fig. 5.3.5) based on Equation [5] of Appendix B.

Figure 5.3.5a shows σ'_p profiles obtained from the approach based on the site-specific $N_{\sigma t}$ (black line) and the constant $N_{\sigma t}$ = 3.4 (grey line) following Demers and Leroueil (2002). σ'_{pb} values from the oedometer tests are also plotted (red circles). By relating σ'_p to the vertical effective stress, σ'_{v0}, we find clear overconsolidation from the surface down to 9 mbsf, and a slight overconsolidation down to 12 mbsf if considering the site-specific $N_{\sigma t}$ and down to 30 mbsf if $N_{\sigma t}$ = 3.4 (Fig. 5.3.5b). Below these depths the sequence appears

Depth (mbsf)	Sample	σ'_{pa} (kPa)	σ'_{pb} (kPa)
4.3	S3	90	90
12.2	S8	60	80
16.8	S9	80	110
32.6	S14	215	167
36.0	S15	156	176
45.0	S20	125	198

Table 5.3.3. Preconsolidation pressure from oedometer tests as derived from Casagrande's (σ'_{pa}) and Onitsuka's (σ'_{pb}) methods, respectively.

underconsolidated according to $\sigma'_{v0} > \sigma'_p$ (see Equation 4 in Appendix B).

The identification of overconsolidation in the upper 30 m indicates that σ'_p calculated from $N_{\sigma t}$ = 3.4 following Demers and Leroueil (2002) cannot be applied to our case since the erosion processes required to generate such an overconsolidation have ever been described in the study area. Therefore, we consider the σ'_p based on the site-specific $N_{\sigma t}$ to be the best approach for the upper continental slope in the Gulf of Lion.

5.3.4.3. Overpressure

Underconsolidation at site PRGL1 is explained by excess pore pressure (Fig. 5.3.5c). According to Equation [6] in Appendix C.1, the excess pore pressure calculated following the site-specific $N_{\sigma t}$ approach indicates that the soil is overpressurized below 12 mbsf down to the borehole bottom. In order to verify this overpressure, labelled DuCPTU, we compared it to an Δu profile estimated from P-wave velocity downhole logging measurements at borehole PRGL1_4, Δu_{LOGS}, following Equations [7] to [9] of Appendix C.1. The average values used for this calculation are eo = 1.21 and I = 0.09 (see Appendix C.1).

The Δu_{LOGS} profile depicts only three overpressurized intervals at 34-39, 89.5-91.5 and 121.7-122.5 mbsf (red curve in Fig. 5.3.6). Additional equilibrium pore pressure values, Δ_{ue}, obtained from dissipation tests (Figs. 5.3.7a to 5.3.7c) are compared with consistent Δu_{CPTU} and Δu values derived from oedometer results, Δu_{oedo} (calculated by means of Equation 6 in Appendix C.1). Of the three levels with excess pore pressure identified from Δu_{LOGS} only the one at 34-39 mbsf clearly corresponds to a relative increase in Δu_{CPTU} and in the sand fraction from 34 to 36 mbsf (Figs. 5.3.6 and 5.3.8). The 121.7-122.5 mbsf interval is at the boundary of a sand fraction increase (Fig. 5.3.8). In consequence, as it appears that Δu_{LOGS} is not consistent with Δu_{oedo} and Δu_e, and since no relationship can be established with the general trend of Δu_{LOGS} and grain size, we have decided to discard Δu_{LOGS}. Table 5.3.5 summarizes Δu values as derived from oedometer and dissipation tests.

Down to 12 mbsf the adimensional ratio of the overpressure magnitude λ^* (Fig. 5.3.6; see Appendix C.1) responds to $\sigma'_p < \sigma'_{v0}$ (Fig. 5.3.5a and 5.3.5b) and, thus, to the presence of overpressure. Below this depth λ^* allows differentiating two main units: (i) from 12 to 72 mbsf, characterized by variable λ^* with predominance of $\lambda^* > 0.3$, and (ii) a lower unit from 72 mbsf to the borehole base at 150 mbsf, with $\lambda^* \sim 0.3$ (Fig. 5.3.6). The boundary at 72 mbsf coincides with a clear decrease in the sand content in both the bulk (BF) and the carbonate free fractions (CFF) (Fig. 5.3.8). The unit from 12 to 72 mbsf contains average

Depth (mbsf)	$N_{\sigma t}$ (for OCR_3)	Sand (%)		Silt (%)		Clay (%)		Silt/Clay	
		BF	CFF	BF	CFF	BF	CFF	BF	CFF
0 – 7	3.4	1.88	4.83	46.81	51.87	51.32	43.30	0.94	1.21
7 – 15	5.6	1.05	1.89	43.92	49.34	57.82	48.79	0.80	1.02
15 – 27	6.9	0.00	2.31	40.69	45.63	59.31	52.21	0.69	0.88
27 – 33	4.0	1.79	0.40	39.38	41.80	58.84	57.79	0.68	0.73
33 – 72	5.0	2.44	3.19	48.74	52.23	48.81	44.57	1.06	1.22
72 – 122	4.0	0.23	1.12	42.58	47.48	57.19	51.40	0.77	0.97
122 – 127	5.0	2.71	7.70	54.14	55.49	43.17	36.81	1.29	1.54
127 – 142	4.0	0.58	0.62	41.14	46.65	58.28	52.73	0.73	0.91
142 – 150	5.0	0.31	2.14	47.72	51.74	51.98	46.12	0.92	1.13

Table 5.3.4. Interval values of the site-specific $N_{\sigma t}$ compared to averaged grain size data. BF: bulk sediment fraction. CFF: carbonate free sediment fraction. Note that the sand and silt fractions are higher in the carbonate free subsamples than in the bulk samples for all intervals.

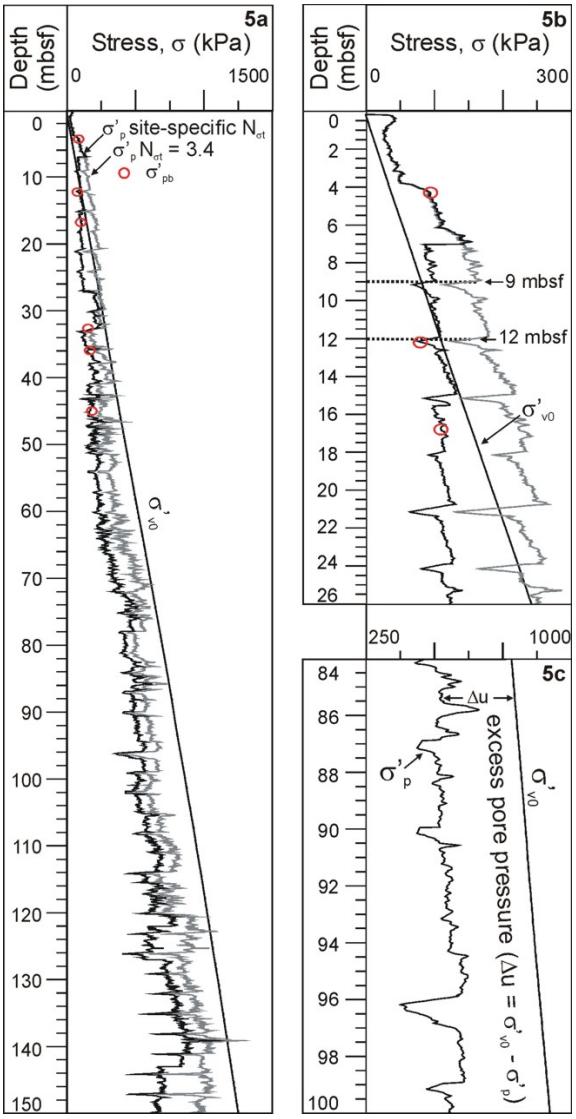

Figure 5.3.5. Preconsolidation pressure (σ'_p) at PRGL1 site. Figure 5a shows continuous σ'_p profiles estimated from the site-specific $N_{\sigma t}$ profile (black line) and the $N_{\sigma t}$=3.4 (grey line, after Demers and Leroueil 2002); σ'_{vo} corresponds to the vertical effective stress and the red circles to σ'_{pb} values interpreted from oedometer tests. Figure 5b illustrates overconsolidation ($\sigma'_p > \sigma'_{vo}$) from 0 to 12 mbsf according to the site-specific $N_{\sigma t}$ and from 0 to 30 mbsf based on a constant $N_{\sigma t}$=3.4 (after Demers and Leroueil 2002). Figure c shows a detail of the excess pore pressure ($\sigma'_p < \sigma'_{vo}$) found from 12 mbsf down to the borehole bot-

sand contents of 1.8% (BF) and 2.8% (CFF), with maximum values of 11.80% (BF) and 5.96% (CFF), whereas in the lower unit the averages are 0.44% (BF) and 1.5% (CFF), with maximum values of 2.36% (BF) and 8.91% (CFF) (Fig. 5.3.8). From this, we infer that small augmentations in the sand content may lead to significantly higher overpressures (higher λ*).

The lower and upper bound shear strength (Su_{min} and Su_{max}, respectively) were calculated from the net tip resistance qnet and the factor N_k equal to 15 and 10, respectively (Appendix C.2). Su_{min}, Su_{max} and in situ shear vane measurements published in Sultan et al. (2007) were used for calculating the Shansep factor as (Fig. 5.3.9). This factor allows the evaluation of the consolidation by normalizing the shear strength Su with respect to effective vertical stress σ'_{v0}. Values lower than 0.25 indicate underconsolidation and upper values overconsolidation (Tanaka et al., 2002). As values of in situ vane measurements and Su_{min} obtained at PRGL1 are lower than 0.25, which confirms the presence of underconsolidation below 9 and 20 mbsf, respectively. This indicates that overpressurized sediments appear at some depth between 9 and 21 mbsf, which is in agreement with our boundary between overconsolidated and underconsolidated sediments at 12 mbsf.

5.3.5. Discussion

5.3.5.1. Stress history related to geological processes

In our PRGL1 site we have found both overconsolidated sediments in the upper 12 m and underconsolidated sediments below. Overconsolidation in marine sediments has been related to erosion and to ice sheet degrounding resulting in the removal of overburden pressure (Craig, 2005). While overconsolidation in the study area cannot be attributed to ice sheet dynamics (Lowe and Walker, 1984), no evidences of erosion have been found in the PRGL1 site (Berné et al., 2004b). Therefore, other mechanisms should account for the overconsolidation of the uppermost section of PRGL1. One acceptable hypothesis is the ageing effects related to cementation, bioturbation and physico-chemical changes that have been

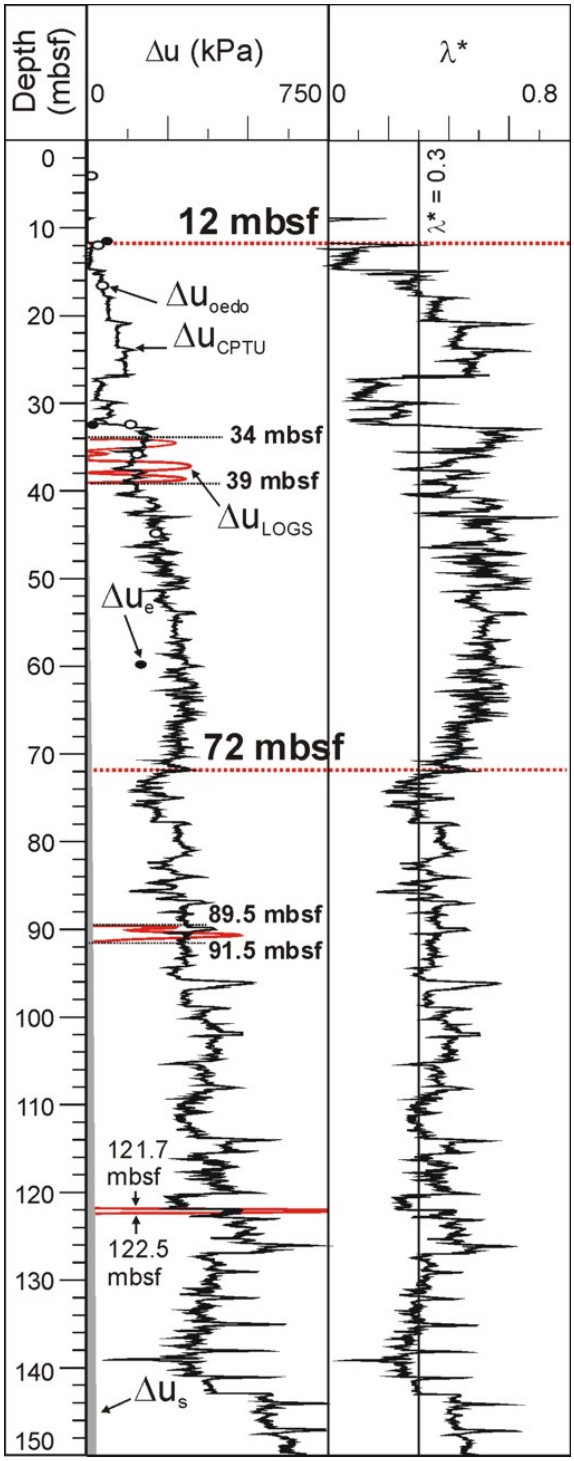

Figure 5.3.6. Excess pore pressure (Δu) and over-pressure ratio (λ^*) at PRGL1 site. Δu_{oedo} measurements are derived from oedometer tests, Δu_{CPTU} from in situ tests, Δu_e from dissipation tests, and Δu_{LOGS} from the P-wave downhole logging profile.

described in marine environments (Baraza et al., 1990; Mitchell, 1976; Poulos, 1998; Silva and Bryant, 2000; Sultan et al., 2000).

On the other hand, underconsolidation of marine sediments is usually associated with excess pore pressure. A well known example is the rapid sediment loading, e.g. >1mm yr^{-1} in the Gulf of Mexico (Expedition 308 Scientists, 2005), that favours overpressure development in the sediment column as fast burial by fine sediment fluxes prevents fluids to escape. The fluids thus bear some of the overburden pressure and delay the normal consolidation process, which leads to underconsolidation (Gordon and Flemings, 1998).

We have estimated by back analysis the excess pore pressure generated by sediment loading (Δu_s) and the stress state at PRGL1 (see Appendix C.1 for the details on the procedure followed). Our results suggest that the averaged sedimentation rates at PRGL1 site (Table 5.3.6) are not high enough to generate the required overpressure, i.e. Δu_s only explains ~ 1% of the total excess pore pressure found in the study area (Fig. 5.3.6).

Other sources of excess pore pressure reported in the literature are gas hydrates (Jansen et al., 1987), and the decomposition of the organic matter that can result in the generation of free gas and thus excess pore pressure (Orange et al., 2005). However, temperature and pressure conditions prevent the development of gas hydrates in the study area (Kvenvolden, 2000). Excess pore pressures may be also triggered by earthquakes, as found in the Norwegian continental margin (Solheim et al., 2005), but the study area is seismically quiet (Grüntal et al., 1999).

The presence of pockmarks in the study area, with a large one extending deep into the sedimentary column at the location of PRGL1, and of high amplitude values in seismic reflection profiles (Berné et al., 2006 and our Fig. 5.3.8) suggest the presence of free gas that could account for the generation of the observed excess pore pressure.

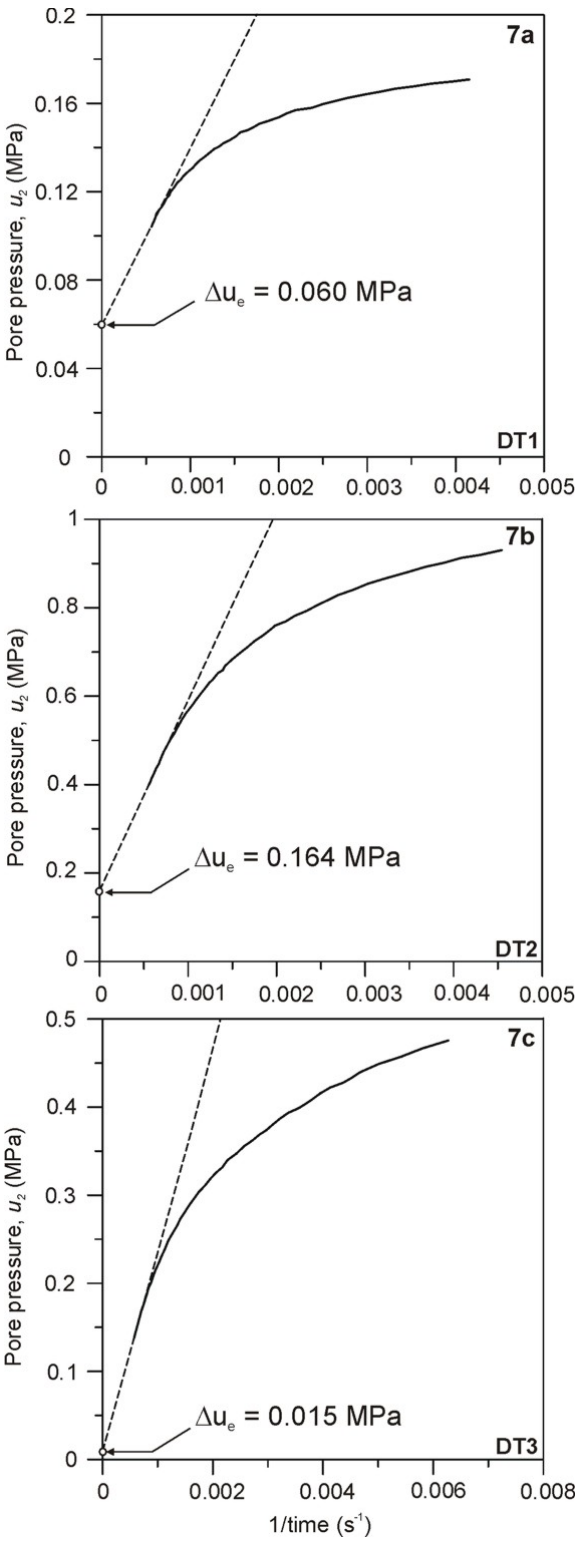

Figure 5.3.7. Equilibrium pore pressure (Δu_e) measured during CPTU dissipation tests. Figure 7a corresponds to dissipation test DT1 at 11.7 mbsf, Figure 7b to dissipation test DT2 at 32.6 mbsf and Figure 7c to dissipation test DT3 at 59.9 mbsf.

It is known that overpressure may appear in sand-bearing layers interbedded within low permeability sediment packages preventing fluids to escape (Magara 1978.). The PRGL1 λ^* profile displays quasi-constant low overpressure values (λ^*~0.3) at the lower unit, from 72 mbsf to the borehole base, and higher values (λ^*>0.3) along most of the unit above, from 72 to 12 mbsf. We associate this specific overpressure profile to four overpressure sources, SI to SIV from bottom to top, with λ^*>0.3, that correspond to depth levels where the dominantly silty-clayey sediment contains increased proportions of sand (Fig. 5.3.8).

Seismic reflection profiles crossing the PRGL1 site show high amplitudes at the depths of overpressure sources SI, SII, SIII and SIV that could indicate (i) overpressure due to the presence of free gas and/or (ii) low P-wave velocity also generated by the presence of free gas (highest seismic amplitudes in Fig. 5.3.8). These depth levels show relatively high sand contents (mainly in the CFF) and are characterized by an increased cone resistance (q_c) and a reduced pore pressure (u_2) (Fig. 5.3.10) due to the permeability of sand. Other levels displaying similar sand contents do not show equivalent high amplitudes in the seismic reflection profiles. Some disrupted reflectors from 150 mbsf to the seafloor in the seismic reflection profile of Figure 5.3.8 indicate vertical fluid migration, likely of free gas. This observation supports the existence of a link between overpressure and free gas from SI upwards, as related to the pockmark in the seismic reflection profile in Figure 5.3.8.

The convex shape of the λ^* profile from 33 to 72 mbsf suggests that fluid flow and overpressure generation from SII and SIII occurs in all directions whereas from SIV only upwards fluid migration is possible due to λ^*< 0.3 values likely related to a relative low permeability layer from 27 to 33 mbsf.

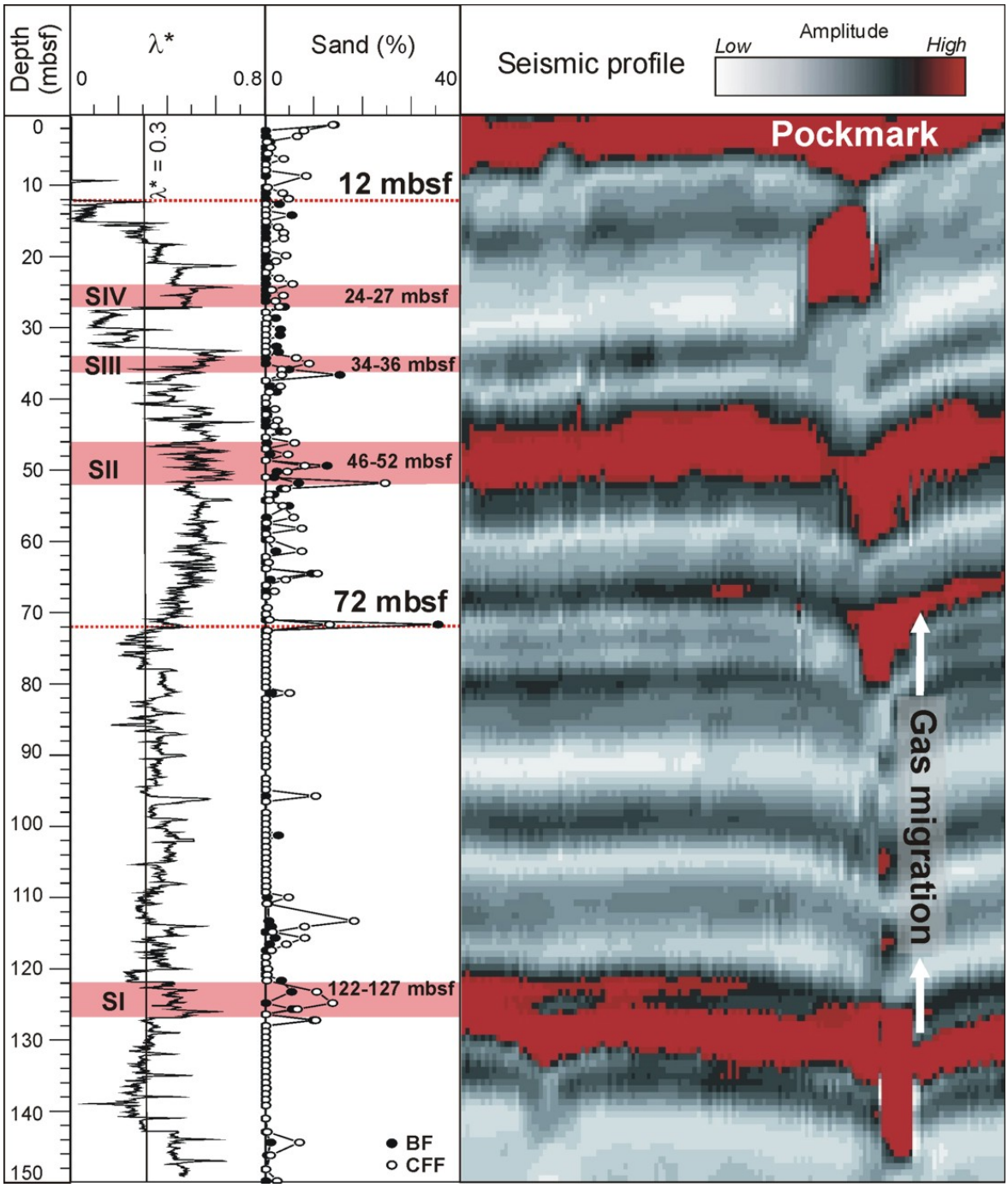

Figure 5.3.8. Correlation amongst overpressure ratio (λ*), sand contents and a seismic reflection profile across site PRGL1 site. Sand contents correspond to both the bulk fraction (BF) and the carbonate free fraction (CFF). Seismic amplitude scale in upper right corner. Pink fringes from 24-27 mbsf, 34-36 mbsf, 46-52 mbsf and 122-127 mbsf correspond to overpressure sources SI to SIV. The dotted lines at 12 and 72 mbsf mark the boundaries between the main units described in the text. The dashed lines show the correspondence between overpressure source SIV and the shallowest high amplitude anomaly associated to the labelled pockmark.

Oedometer tests			Dissipation tests		
Depth (mbsf)	Sample/ID	Δu_{oedo} (kPa)	Depth (mbsf)	Sample/ID	Δu_e (kPa)
4.3	S3	0.0	-	-	-
11.7	-	-	11.7	DT1	60.0
12.2	S8	31.4	-	-	-
16.8	S9	45.1	-	-	-
32.6	S14	133.1	32.6	DT2	15.0
36.0	S15	153.5	-	-	-
45.0	S20	212.5	-	-	-
59.9	-	-	59.9	DT3	165.0

Table 5.3.5. Excess pore pressure obtained from oedometer tests (Δu_{oedo}) and equilibrium pore pressure from dissipation tests (Δu_e).

The excess pore pressure related to free gas could be explained by gas exsolution processes and sea level variations driven by global climate oscillations. Sea level falls cause a reduction in hydrostatic pore pressure that lowers the gas solubility and results in gas exsolution. The exsoluted gas will then accumulate preferentially in relatively more porous (i.e. sand-bearing) layers interbedded within less permeable (i.e. without sand) layers. In contrast, during sea level rises, the increase in the hydrostatic pressure dissolves free gas in the water would therefore decrease the excess pore pressure. According to this, the four main sources of overpressure (SI to SIV) found in sand-bearing layers could be linked to millennial scale sea level changes and gas exsolution.

5.3.5.2. Overpressure and sea level variations

In Figure 5.3.11, we compare sand contents (BF and CFF), depth of main overpressure sources and the sea level curve of Sidall et al. (2003). The 150 meters long sedimentary sequence described in this paper represents about 340 kyr (336 kyr at 159.98 mbsf as shown in Table 5.3.2) during which overall decreasing sea level fall periods occupy a much longer cumulative time period than sea level rises.

Our inferred age model (Table 5.3.2) allows assigning ages to the main overpressured layers. The age of SIV is 24-26 kyr old, SIII is 33-38 kyr old, SII is 46-55 kyr old, and SI is

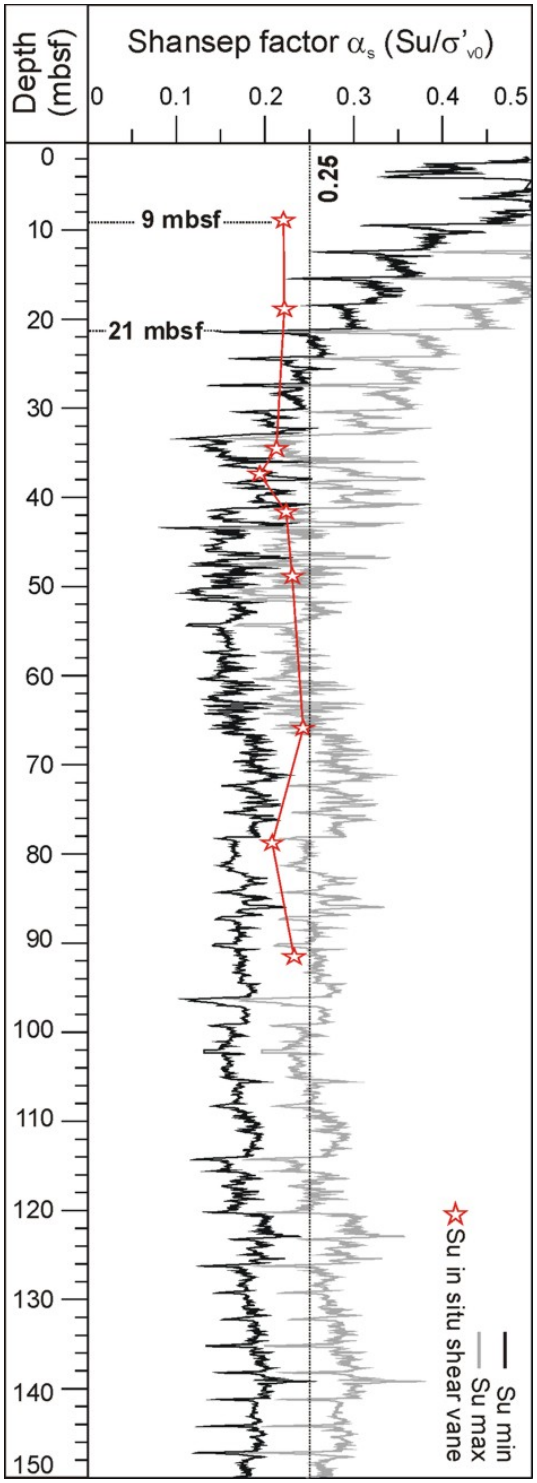

Figure 5.3.9. Shansep (Su/σ'$_{v0}$) factor from CPTU based undrained shear strength. Black and grey lines correspond to lower and upper bounds of the Shansep factor, calculated from respective lower and upper Su values (Su_{min} and Su_{max}). Stars correspond to Su values measured by in situ shear vane measurements. Line at Su/σ'$_{v0}$ equal to 0.25 corresponds to the boundary between underconsolidated and normally consolidated conditions.

Depth interval (m)	Sedimentation rate (m·kyr^{-1})	α (-)	Corrected sedimentation rate (m·kyr^{-1})
0-15	2.0	1.21	2.4
15-30	1.7	1.25	2.1
30-33	2.3	1.27	3.0
33-41	0.9	1.27	1.1
41-47	1.2	1.28	1.5
47-54	0.5	1.28	0.6
54-64	0.7	1.29	0.9
64-72	0.1	1.30	1.9
72-110	0.6	1.31	0.8
110-120	0.3	1.32	0.4
120-127	0.2	1.34	0.3
127-140	0.4	1.35	0.5

Table 5.3.6. Corrected sedimentation rates and correction factors (α) applied. The values in the second, third and fourth columns have been rounded to the first, second and first decimal, respectively.

220-238 kyr old. According to the general sea level curve in Figure 5.3.11, SIV and SIII correspond to relatively high stillstands, SII to the highstand part of a secondary rise and fall event, and SI to a high sea level followed by a pronounced lowering. Therefore, though SIV, SIII and SII occurred during the decreasing sea level falling trend from 123 to 20 kyr, they all represent intervals of relatively high sea level preceding lowering phases.

The aforementioned suggests that sand-bearing intervals SI to SIV were deposited under relative highstands and subsequent sea level falls might generate excess pore pressure by gas exsolution. Therefore, the overpressure source SI would relate to the sea level peak and fall from 238 to 220 kyr, to the dissolution period from 220 to 193 kyr and to a first exsolution period from 193 to 130 kyr, and to a later dissolution period from 130 to 123 kyr and a second exsolution period during the general sea level fall from 123 to 20 kyr (Fig. 5.3.11). Overpressure source SII would be linked to the decrease in sea level from 50 to 38 kyr, 33 to 26 kyr and 24 to 20 kyr, SIII to the decrease from 33 to 26 and 24 to 20 kyr, and SIV to the decrease from 24 to 20 kyr, in agreement with the findings of Jouet et al. (2006) in the same area.

The highest excess pore pressure is to be expected at level SI as the dissipation of the excess pore pressure is proportional to the square of the drainage distance that in this case is the distance to the seafloor. Therefore, for the same initial excess pore pressure, SIV would dissipate the excess pore pressure much earlier than SI. However, successive phases of exsolution and dissolution (during sea level rises) would explain lower λ* values for SI. Compared to SI, the different history of SII to SIV, which have been affected by only one major sea level rise (the one following the last deglaciation from 20 kyr to present), would explain the higher excess pore pressure found above 72 mbsf (Fig. 5.3.8). Indeed, this

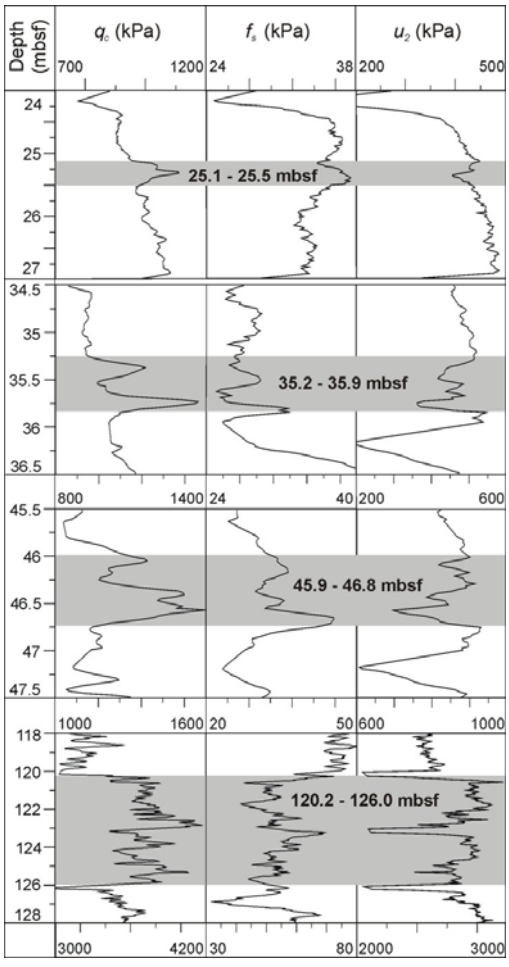

Figure 5.3.10. CPTU behaviour in the sand-bearing overpressurized layers identified. Relative high sand contents (mainly in the CFF, Fig. 5.3.8) are characterized by increases in cone resistance (q_c) and a reduced pore pressure (u_2) due to the permeability of sand.

particular depth coincides with the highstand at 123 kyr, supporting the idea that gas in layers below 72 mbsf was significantly affected by dissolution processes from 130 to 123 kyr. An additional relevant factor that may justify the higher excess pore pressures at the upper levels SII to SIV with respect to SI is the volume change of free gas due to a decrease of the hydrostatic pressure: for a given decrease of the hydrostatic pressure Δu_h, the volume change of the free gas (or the excess pore pressure) decreases with depth as it depends on $\Delta u_h / u_h^2$ where u_h is the hydrostatic pressure at a given depth.

The excess pore pressure generated by gas exsolution is considered to take place during the whole sea level fall process. Therefore the excess pore generated by gas release and exsolution from sandy layers could be considered as a continuous flow during the whole sea level fall process (Appendix D.1). By considering the level SI and for a mean of the hydraulic diffusivity D_h of 5.10-9 m^2/s (determined from oedometer tests), the dissipation of 93% of the pressure will need around $t_{93\%}$= 3960 years for a drainage distance of 25 m and $t_{93\%}$ =90000 years for a drainage distance of 120 m.

A simple calculation was also carried out to evaluate the time needed for the dissipation process of the pore pressure during the last sea level rise for the whole sedimentary profile (Appendix D.2). Three λ^* profiles at 20 kyr, 10 kyr and 0 kyr were calculated and are presented in Figure 5.3.12a. For the considered sediment profile with the hydraulic diffusivities values presented in Figure 5.3.12b, it is clear that 20 kyr is not enough to dissipate the excess pore pressure generated by gas exsolution.

It is not known how fast gas exsolution responds to decreases in the hydrostatic pressure during sea level falls, nor how fast dissolution increased under the high hydrostatic pressure of both the 123-116 kyr highstand interval and the present-day highstand. Notwithstanding, we think likely

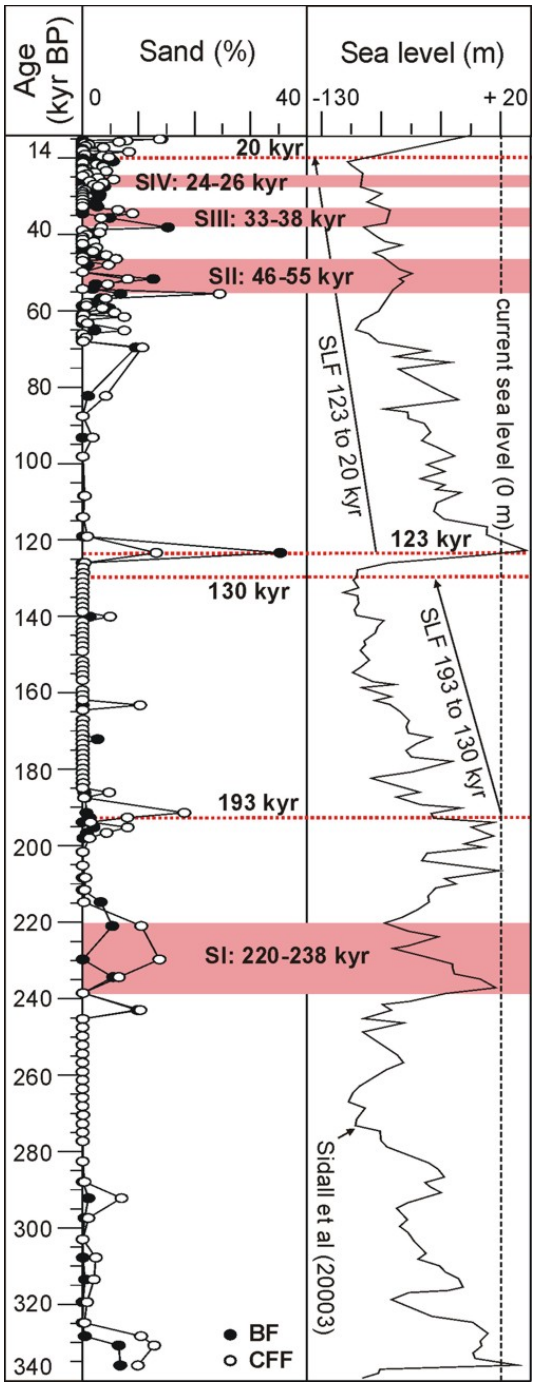

Figure 5.3.11. Sand contents and overpressure sources at site PRGL1 compared to sea level oscillations from Sidall et al. (2003). Sand contents correspond to both the bulk fraction (BF) and the carbonate free fraction (CFF). The borehole depth scale has been converted into an age scale after the inferred age model in Table 5.3.2. Note that the top age is 14 kyr. Pink fringes at 24-26, 33-38, 46-55 and 220-238 kyr correspond to overpressure sources SI to SIV. The dotted lines at 20, 123, 130 and 193 kyr mark the boundaries between overall sea level fall (SLF) and rise periods.

that part of the present day excess pore pressure corresponds to the pore pressure generated during previous sea level falls and lowstands. The inherited excess pore pressure possibly is proportional to the cumulated time difference between slow, punctuated sea level falls and much faster sea level rises (Fig. 5.3.11). Gas exsolution during sea level falls increases the gas saturation and generates upward migration of the free gas. Shallower layers are, therefore, submitted to local gas exsolution but also to the migration of deep overpressured gas. The migration of the free gas is proportional to the time length of sea level falls. During the quick sea level rises (Fig. 5.3.11), residual excess pore pressure may exist as migrated gas partially saturating shallower sand-bearing layers exceeds gas solubility under the new hydrostatic conditions induced by high sea level. The presence of pockmarks in the study area is a clear indication of the significance of gas migration, which occurred mainly during sea level falls.

5.3.6. Conclusions

The stress history at PRGL1 site has been reconstructed from empirical correlations based on CPTU measurements and derived preconsolidation pressures, which are consistent with results from oedometer tests and dissipation tests. By relating the CPTU based preconsolidation pressure and the current vertical effective stress, an excess pore pressure has been found from 12 mbsf down to the borehole bottom at 150 mbsf. Our data show that such an excess pore pressure is mainly fed by four overpressure sources corresponding to sand-bearing layers within an upward gas migration setting related to pockmark development. We link the observed overpressure situation to persistent hydrostatic pressure diminutions causing gas exsolution during the prolonged periods of sea level lowering of, at least, the last 340 kyr. No other overpressure sources have been identified in the study area. Our results clearly point out the need of further

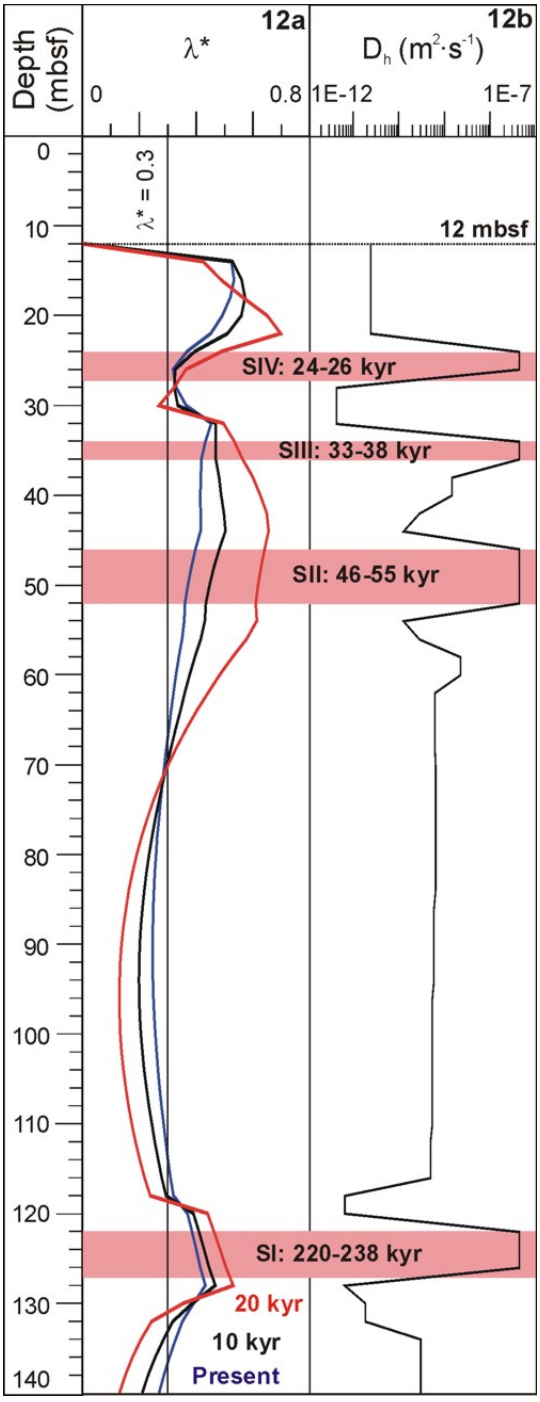

Figure 5.3.12. Time needed for the dissipation process of the pore pressure during the last sea level rise. Figure a shows λ* profiles obtained from Equation 13 (Appendix D.1, this section) and showing excess pore pressure dissipation during the last sea level rise (from 20 kyr to present). Figure b shows the profile of the hydraulic diffusivity used in the calculation based on Equation 14 (Appendix D.2, this section).

studies on the effects of global sea level changes coupled with the presence and behaviour of gas to elucidate the stress history of continental slopes, where most of submarine instability processes occur worldwide. In situ measurements, like CPTU, are crucial to address this question.

Acknowledgements

We thank the PROMESS1 scientific party, and the technical staff and crew from Fugro Engineers B.V. and Amige onboard SRV Bavenit (ref. EVR1-CT-2002-40024) for their continuous support during CPTU tests at sea. The EURODOM Research Training Network (ref. RTN2-2001-00281) eased the cooperation between IFREMER and University of Barcelona researchers. Additional support was provided to Ifremer staff by the French Agence Nationale de la Recherche (ANR, contract NT05-3-42040). The crew and technical staff onboard R/V Le Suroît (Ifremer and Genavir) are thanked for their assistance during seismic reflection data acquisition at sea. We also thank G. Herrera (Universitat de Barcelona) for grain size analyses and E. Thereau (Ifremer) for processing the seismic data. Dr. J. Locat and Dr. S. Leroueil from the University of Laval, Quebec, provided helpful suggestions. We also acknowledge all other researchers and technicians from PROMESS1 partner institutions that have contributed in different ways to this research. S. Lafuerza benefits from a PhD research grant by the Spanish Ministry for Education and Science. GRC Geociències Marines is funded by Generalitat de Catalunya research grants program to high quality scientific groups (ref. 2005 SGR-00152).

Appendix A

A.1. CPTU background information

Corrections and derived parameters

Due to the geometric design of the piezocone penetrometer, the pore pressure acts on the shoulder above the tip and at both ends of the friction sleeve. This influences the total stress measured from the cone tip resistance, q_c, and the sleeve friction, f_s. This is known as the "unequal area effect" (Lunne et al. 1997). CPTU data are interpreted by using derived parameters, such as corrected tip resistance, qt (Equation 1), which accounts for avoiding the unequal area effect. In fine-grained sediments, q_c, f_s and u tend to increase with increasing overburden stress, resulting in a false change in the CPTU soil type classification. To solve this problem, the direct CPTU parameters are usually normalized, being the net tip resistance, qnet (Equation 2) and the normalized tip resistance, Q_t (Equation 3) useful parameters for stratigraphic interpretations:

$$q_t = q_c + u_2 \cdot (1\text{-}a) \quad [1]$$

$$q_{net} = q_t - \sigma_{v0} \quad [2]$$

$$Q_t = (q_t - \sigma_{v0}) / \sigma'_{v0} \quad [3]$$

where a is the cone area ratio of the cross-sectional area at the gap between cone and friction sleeve to the cone base area, which is 0.75 in this study. σ_{v0} is the total in situ vertical stress relative to seafloor and σ'_{v0}, the vertical effective stress.

Dissipation tests

The piezocone can be stopped at any depth during penetration and this allows monitoring the variation with time of the measured parameters. Dissipation curves are used for estimating the equilibrium pore pressure, which is the in situ pore pressure, by relating the measured pore pressure with 1/time of dissipation.

A.2. Grain size analyses

The grain size data presented in this study were obtained with a Coulter LS100 Laser Particle Size Analyser. Sampling frequency was each 80 cm. Grain size analyses were done on the bulk fraction (BF) and on the carbonate free fraction (CFF). Carbonate was removed by attack with HCl 10%. Sand (>63 mm), silt (2-63 mm) and clay (<2m m)

fractions were determined. The clay fraction underestimation attributed to difractometers like the Coulter Counter if compared with results from pipette analysis (McCave et al., 1995) was corrected following Konert and Vandenberghe (1997). Therefore, the Coulter Counter fraction <8 mm was considered equivalent to the <2 mm pipette analysis fraction, while the 8-63 mm Coulter Counter fraction was considered equivalent to the 2-63 mm pipette fraction.

Appendix B

Methodology for CPTU and laboratory based stress history analysis

Definition of preconsolidation pressure and overconsolidation ratio

If the present vertical effective stress (σ'_{v0}) is the highest the soil has ever been submitted, i.e. the preconsolidation pressure (σ'_p), the soil is normally consolidated. If some time in the past the effective stress has been larger than the present one, the soil is overconsolidated. If the present vertical effective stress is less than it should be according to the burial depth of the investigated sediment layer, then it is underconsolidated. The highest past vertical effective stress divided by its present value is known as the overconsolidation ratio (OCR), as Equation [4] shows:

$$OCR = \sigma'_p / \sigma'_{v0} \quad [4]$$

where σ'_{v0} is the vertical effective stress considering hydrostatic conditions ($\sigma'_{v0} = \sigma_{v0} - u_h$). If OCR > 1 the soil is overconsolidated; if OCR = 1 the soil is normally consolidated; if OCR < 1 the soil is underconsolidated.

CPTU approach

Based on the evaluation of the existing methods for estimating σ'_p from CPTU data published by Demers and Leroueil (2002), a continuous, site-specific $N_{\sigma t}$ profile has been determined. For this, the $N_{\sigma t}$ derived from the σ'_p estimated from the oedometer tests has been related to changes in grain size distributions. This approach is derived from the following expression:

$$N_{\sigma t} = (q_t - \sigma_{v0}) / \sigma'_p \quad [5]$$

Appendix C

C.1. Overpressure and related concepts

Overpressure and excess pore pressure

Overpressure exists when there is an excess pore pressure, Δu, which is interpreted as the difference between the current effective stress (σ'_{v0}) and the preconsolidation pressure (σ'_p), as follows:

$$\Delta u = \sigma'_{v0} - \sigma'_p \quad [6]$$

Overpressure estimated from downhole logs

A simple empirical function relating P-wave velocity and porosity (ϕ) called "time average equation" (Wyllie et al. 1956) has been applied to calculate a continuous ϕ profile according to Equation [7]:

$$Vp = \phi \cdot Vp_w + (1 + \phi) \cdot Vp_s \quad [7]$$

where Vp is the compressional wave (P-wave) velocity, Vp_w the Vp of the fluid, e.g. 1500 m s^{-1} and Vps the Vp of the sediment (solid grain), e.g. mean of 1700 m s^{-1} in clays (Nafe and Drake 1957). On the other hand, porosity and the void ratio are related by:

$$e = \phi / (1 - \phi) \quad [8]$$

From Equation [8], a continuous void ratio profile is derived, which can be directly utilised for calculating a secondary σ'_p profile, by means of the following compressibility equation:

$$e - e_o = -\lambda \cdot \ln(\sigma'_p / \sigma'_{v0}) \quad [9]$$

where e_0 is the reference void ratio at a vertical effective stress of σ'_{v0}, λ is the compression index and σ'_p the preconsolidation pressure. e_0 and λ are determined from oedometer tests. σ'_p calculated from Equation [9] is used to

estimate the overpressure, Δu_{LOGS}, by means of Equation [6].

Overpressure ratio

The excess pore pressure, Δu, is the pressure gradient that is usually converted to an adimensional ratio of the magnitude of overpressure, which is defined as follows:

$$\lambda^* = (\Delta u - u_h) / (\sigma_{v0} - u_h) \quad [10]$$

where u_h is the hydrostatic pressure and σ_{v0} the total vertical stress (Expedition 305 Scientists, 2005).

Excess pore pressure generated by sedimentation

Following Sultan et al. (2004), the excess pore pressure generated by sediment accumulation, Δ_{us}, is calculated from (i) biostratigraphy derived average sedimentation rates from PRGL1_4 borehole, (ii) the reference void ratio (e_o), and (iii) the compression index (λ) derived from oedometer tests. The average sedimentation rates are corrected by multiplying them by the so-called factor a (Equation 11) (Dennielou et al., 2006) that accounts for the difference between the initial sediment height before consolidation and the final sediment height:

$$a = 1 - [(\lambda / 1+e_o)\cdot \ln(\sigma'_v / \sigma'_{v0})] \quad [11]$$

where λ is the compression index, e_0 a reference void ratio at a reference vertical effective stress σ'_{v0}, and σ'_v the effective stress (definitions already provided). Here σ'_v corresponds to the notation σ'_{v0} used in Equation [3] in Appendix A, [4] in Appendix B and [6] in Appendix C.

C.2. Shear strength from CPTU data

An estimate of the undrained shear strength Su can be deduced from the following equation:

$$Su = q_{net} / N_k \quad [12]$$

We have calculated the lower and upper boundaries of Su by using the empirical cone factor N_k equal to 15 and 10, respectively (Lunne et al. 1997).

Appendix D

D.1. Gas release and exsolution as a continuous flow

The time dissipation t of this pore pressure depends mainly on 2 key parameters: the longest drainage distance h and the hydraulic diffusivity D_h:

$$t = (T_v \cdot h^2) / D_h \quad [13]$$

where T_v is a non-dimensional time factor. T_v was given as a function of the degree of dissipation by Casagrande (1936) and Taylor (1948). For a degree of dissipation of 93%, T_v is equal to 1.

D.2. Dissipation of the pore pressure

The key differential equation used for this process was given by Terzaghi (1943):

$$D_h \frac{\partial^2 u}{\partial z^2} = \frac{\partial u}{\partial t} \quad [14]$$

where u is the pore water pressure, t is time and z denotes the position where u is determined.

5.4. Overpressure as triggering mechanism of Ana Slide (Eivissa Channel, Western Mediterranean)

S. Lafuerza (1), N. Sultan (2), G. Lastras (1), M. Canals (1), A. Cattaneo (2), B. Dennielou (2), S. Costa (1)

(1) GRC Geociències Marines, Departament d'Estratigrafia, Paleontologia i Geociències Marines
(2) Institut Français de Recherche pour l'Exploitation de la Mer, France

Abstract

In situ and laboratory geotechnical data and sediment cores from the Ana Slide, Eivissa Channel, Western Mediterranean Sea, allowed characterizing the upper 28 meters of undisturbed and remoulded sediments at the headscarp and lower slide. Overpressure ratios estimated from CPTU data unveal an overpressure field that reaches up to 40% of the hydrostatic effective stress below depths between 6.6 and 13.25 mbsf from lower slide to headscarp regions. Overpressure is further supported by CPTU-derived normalized undrained shear strength (Su/σ'_{v0}) values <0.25 corresponding to underconsolidated (overpressurized) sediments below the depth range where overpressure has been measured.

Changes in CPTU pressure filter saturation inferred from a highly variable pore pressure (u_2) signal indicate the likely presence of gas bubbles within the sediment, which could account for the estimated overpressure. Piezometer readings and P-wave measurements do not inform about overpressures in the upper 6.75 m thus suggesting that excess pore pressures reside at larger depths (i.e. at a depth range of 6.6-13.25 mbsf). Local erosion with maximum values of 11 m have been identified below the headscarp from overconsolidation ratios higher than 1. The absence of overpressure at sites where erosion is found suggests that overpressure could have been locally dissipated during landsliding.

Furthermore, CPTU profiles reveal the existence of a high sensitivity, relatively coarse-grained layer with reduced undrained shear strength overlying the basal shear surface. Gas could have accumulated preferentially in this weak layer thereby reducing the effective stress and the shear strength and finally leading the slope to fail.

Key words: preconsolidation pressure, overpressure, CPTU, piezometre, gas, weak layer, Ana Slide, Western Mediterrnean Sea.

Article per sotmetre a International Journal of Earth Sciences.

5.4.1. Introduction

In situ pressures in excess of the hydrostatic, i.e. overpressure, affect the stability even of low angle slopes by decreasing the effective stress, which in turn strongly reduces shear strength, bringing slopes to fail (Canals et al., 2004a; Lee et al., 2007). Shear strength depends on the rate at which the shear stresses are applied and the stress history of the sediment. If stresses are applied rapidly in low permeability materials, e.g. overburden is loaded faster than the normal consolidation rate (rapid sedimentation settings), the load is carried by the pore pressure, which causes overpressure.

The Gulf of Mexico continental slope is one of the best known case studies in which shallow overpressures are present due to the very rapid deposition of the Mississippi River sediment discharge through Pleistocene time (Flemings and Lupa, 2004). Sediment that is not fully consolidated under the existing overburden pressure are named underconsolidated. Underconsolidated sediments build up in gas charged settings that can develop through: (1) the decay of organic matter in areas influenced with fluvial input (Orange et al., 2005; García-García et al., 2006, 2007), (2) the dissociation of gas hydrates (Sultan et al., 2004; Ellis et al., 2009), or (3) gas migration from deep hydro-thermal sources, as revealed for example by the gas chimneys in the Nile Deep Sea Fan (Dupré et al., 2007). Groundwater flow and cyclic loading typically caused by earthquakes are other likely sources of excess pore pressure (Lee et al., 2007).

The verification of the existence and origin of overpressure must be based on direct measurements of in situ pore pressure penetrometers or piezometers (Strout and Tjelta, 2005). Pore pressure readings consist on pressure peaks during probe insertion that subsequently decline with time as function of sediment permeability. This pore pressure dissipation can be also run by stops during CPTU execution. In situ pore pressures are directly obtained when initial pressure is fully dissipated and reach the stable level, namely the equilibrium pressure. Equilibrium pressures (u_0) are reached much faster in coarse sediments (<1 h) that in fine sediments, in which it can take several hours to reach u_0. Operations at sea are often time-limited and usually short deployment of piezometers and piezocones are carried out. Consequently, full dissipation is not reached in most of the cases and extrapolation of dissipation times is used to interpret the equilibrium pressure (Davis et al., 1990). Unfortunately, there are no simple analytical approaches to extrapolate partial pressure dissipation data to obtain in situ pressure. The most used is the empirical extrapolation approach based on the inverse time from Davis et al. (1990) (see section E, Appendix) but recent works show that the use of the square root of time requires much less decay time to achieve a desirable accuracy (Flemings et al., 2008).

On the other hand, in situ pressures can be obtained by empirical correlations based on CPTU data. This consist on a simple comparison between CPTU-based preconsolidation pressure (σ'_p) and the vertical effective stress (σ'_v) by subtracting σ'_v from σ'_p, i.e. $\Delta u= \sigma'_p-\sigma'_v$, where Δu represents the excess pore pressure or overpressure, often expressed by the ratio λ^* equal to $\Delta u/ \sigma'_v$. This empirical estimation based on CPTU-based σ'_p (Demers and Leroueil, 2002, section B, Appendix) has proven to be useful for estimating excess pore pressures in slope sedimentary sequences of the Gulf of Lion (Lafuerza et al., 2009).

In this article we present a sedimentological and geotechnical characterization of the sediments of the Ana slide (Eivissa Channel, western Mediterranean Sea) obtained from multiple parameters derived from in situ piezocone test (CPTU), piezometer readings and laboratory analyses of sediment cores. We have evaluated the geotechnical properties of the undisturbed and remoulded sediments and the slide plane, in order to

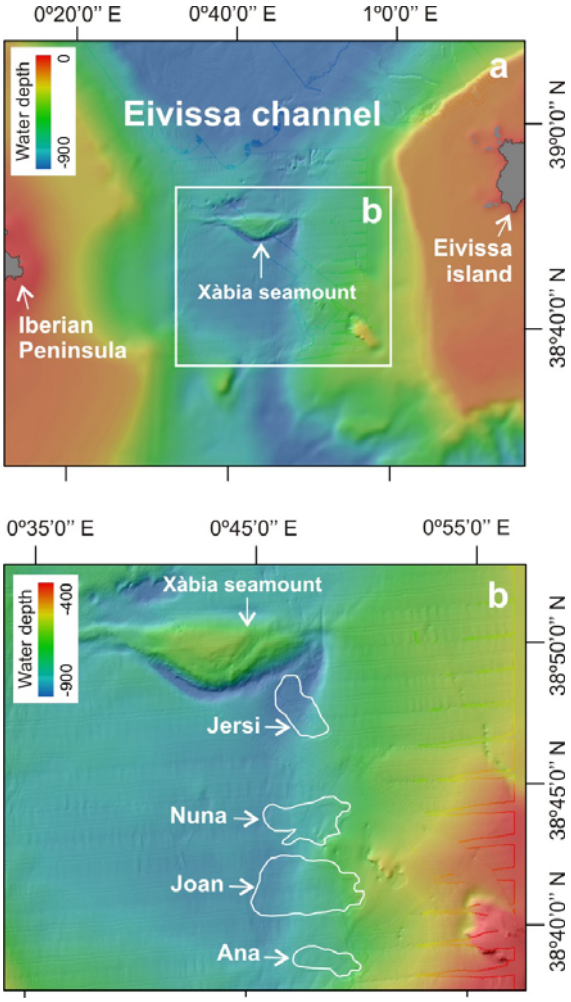

Figure 5.4.1. a: Shaded relief image and swath bathymetry map of the southern Eivissa Channel. The Xàbia Seamount forms the boundary between the northern and southern Eivissa Channel; b: balearic slope of the Eivissa cannel where are outlined the four Eivissa channel landslides Ana, Joan, Nuna and Jersi (based on Lastras et a., 2004)..

find evidences of overpressures identified from the CPTU-based stress history parameters and short term piezometer monitoring, and characterise slope conditions involved in failure and the implication of fluid as source of overpressure as a possible trigger mechanism of the Ana slide.

5.4.2. Geological setting

Four small slides aligned along the 0º48' meridian at water depths ranging between 600 m and 900 m evidence the existence of slope instability processes in the Balearic continental slope of the Eivissa Channel (Fig. 5.4.1; Lastras et al., 2004, 2007). These slides, namely Ana, Joan, Nuna and Jersi occupy areas from 6.0 to 16 km^2 and volumes from 0.14 to 0.4 km^3. They occur in a segment of the continental slope with gradients ranging from 1.6º to 3º. Their depositional lobes are characterized by areas of positive and rougher relief with respect to the surrounding seafloor (Lastras et al., 2004, 2006). However, this relief is much less than the thickness of the disturbed sediment, demonstrating that sediments were not evacuated, with the partial exception of the Jersi Slide (Lastras et al., 2004). The Ana slide, located between 38º37.5'N and 38º39'N and between 0º47'E and 0º51'E, at water depths ranging from 635 m at the rim of the headscarp down to 815 m at its distal region, with an average slope of 1.6º (Fig. 5.4.2), is the one that has been more extensively surveyed. Observations made on seismic reflection profiles by Lastras et al. (2004) indicate that most of the sediment in the central and lower Ana deposit remains in situ or has only slightly displaced, but it looks like highly disrupted, as suggested by chaotic seismic facies (Fig. 5.4.3a). Maximum slide thickness (44 m) contrasts with the small bathymetric expression of the edge of the depositional lobe in terms of height difference, suggesting that modest transfer is accompanied by the downslope propagation of deformation front that extensively remoulds the slope sediment without necessarily translating it very far downslope (Lastras et al., 2004).

The existence of pockmarks in the northern part of the Eivissa channel and the western end of the Balearic promontory has been related to gas and water extrusion through fractures created by subsurface thermogenic and/or hydrothermal fields and volcanic structures (Acosta et al., 2002). The proximity between pockmarks and the four slides on the Balearic margin of the Eivissa channel manifests a likely relationship between sudden releases of fluids and overpressure generation, slides and pockmark formation

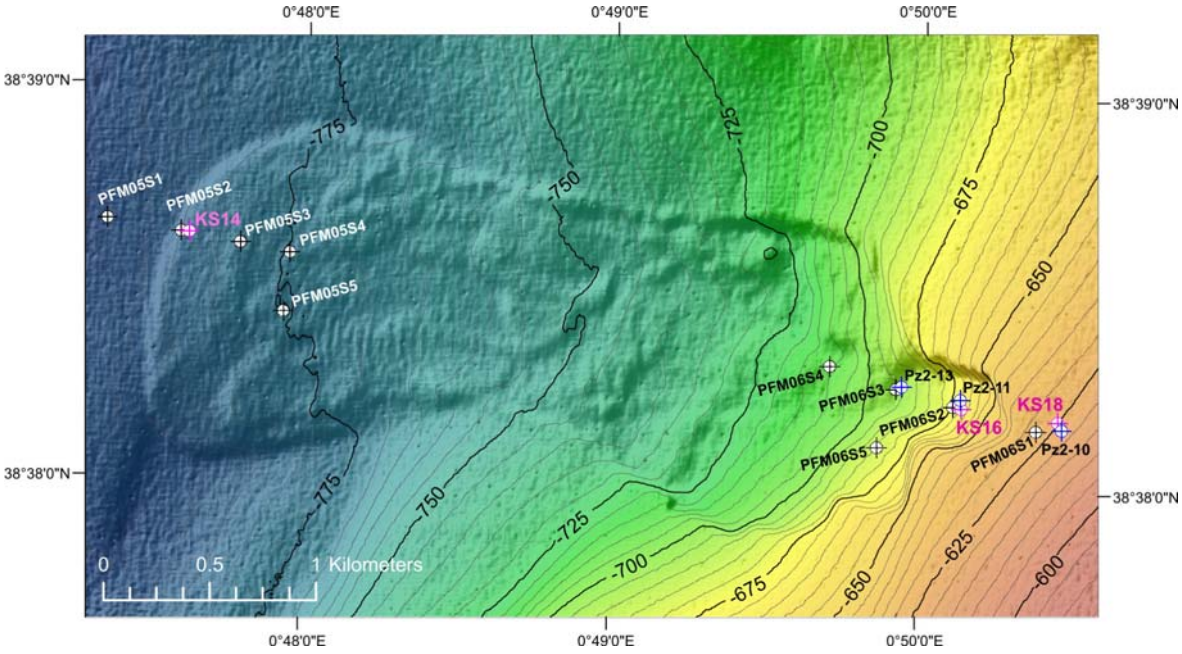

Figure 5.4.2. Shaded relief image and swath bathymetry map of the Ana slide with the PRISME survey sampling and measuring sites. PFM corresponds to CPTU sites, KS to sediment cores and PZ to piezometers.

(Lastras et al., 2006). Recent investigations based on 3D seismic data reveal the existence of another slide buried below the Ana slide. Both slides overlay a high-amplitude, normal-polarity seismic anomaly body not related to free gas but rather to overpressurized fluids that would rise from beneath the Messinian erosional surface up to the seafloor through a preferential pathway (Costa et al., 2009).

5.4.3. Materials and methods

The Eivissa channel area was surveyed in 1995 and 2002 during BIG'95 and MARINADA cruises onboard BIO Hespérides (Spain) in 1995, during which swath bathymetry data and very-high resolution seismic reflection profiles were acquired (Lastras et al., 2004). Additional swath bathymetry data were gathered during CD178 cruise onboard RSS Charles Darwin in 2005. Sedimentological and geotechnical data used in this study were collected during PRISME cruise onboard RV L'Atalante (IFREMER, France) in 2007. In situ tests and sediment cores, detailed below, were located along the Ana slide along the seismic reflection profile TOPAS Marinada-3 (Marinada 2003 cruise, Fig. 5.4.3a) (Lastras et al., 2004). Finally, ^{14}C dating of sediment samples obtained during COBAS cruise onboard RV Urania (CNR, Italy) in 2004 (Cattaneo et al., submitted) have been used to constrain the age of the Ana slide.

In situ measurements consisted of: (i) two deployments of the IFREMER CPTU system named PENFELD that tested 28 metres of sediment at five sites at the headscarp area (PFM06S1 to PFM06S5) and five at the distal lobe (PFM05S1 to PFM05S5) (Table 5.4.1, Fig 5.4.2) and (ii) three piezometre readings of the upper 6.5 sediment at sites Pz2-10, Pz2-11 and Pz2-13 (Table 5.4.2, Fig. 5.4.2). Sites PFM06S1 and PFM05S1 correspond to undisturbed sedimentary sequence whereas the rest hold partially remoulded sediments. Geotechnical stratigraphy derived from CPTU was correlated with reflectors of seismic profile TOPAS Marinada-3 at sites where well-stratified seismic faces have been identified.

5.4.3.1. PENFELD penetrometer

The IFREMER penetrometer PENFELD is a seabed system to perform piezocone tests

Penfeld site	Water depth (m)	Coordinates	Relative location
PFM05S1	798	E 000º 47.356' N 38. 38.651'	Outside distal lobe
PFM05S2	789	E 000º 47.600' N 38º 38.620'	Distal lobe
PFM05S3	784	E 000º 47. 791' N 38º 38.600'	Distal lobe
PFM05S4	779	E 000º 47. 955' N 38º 38.576'	Distal lobe
PFM05S5	781	E 000º 47.937' N 38º 38.426'	Distal lobe
PFM06S1	632	E 000º 50.382' N 38º 38.160'	Outside slide scar
PFM06S2	669	E 000º 50.113' N 38º 38.222'	Below slide scar
PFM06S3	699	E 000º 49.929' N 38º 38.261'	Below slide scar
PFM06S4	710	E 000º 49.713' N 38º 38.316'	Below slide scar
PFM06S5	683	E 000º 49.866' N 38º 38.112'	Below slide scar

Table 5.4.1. Location of CPTU sites measured during PRISME cruise.

Site	Core Section	Depth (cm)	Description
KS14	S1	86-91	Oedometer
	S4	184-189	Oedometer
	S5	280-285	Oedometer
		285-310	Triaxial
	S8	582-587	Oedometer
		587-612	Triaxial
KS16	S1	88-94	Oedometer
	S3	230-255	Triaxial
		255-260	Oedometer
	S5	430-455	Triaxial
		455-460	Oedometer
	S7	627-652	Triaxial
		652-657	Oedometer
KS18	S2	95-100	Oedometer
	S3	265-290	Triaxial
		290-295	Oedometer
	S5	465-490	Triaxial
		490-495	Oedometer
	S7	665-690	Triaxial
		690-695	Oedometer

Table 5.4.3. Oedometer and triaxial samples carried out for sediment cores KS14-KS16-KS18.

that provides continuous measurements of the cone tip resistance (q_c), sleeve friction (f_s) and excess pore pressure (u_2) behind the cone tip (Meunier et al., 2005). From CPTU based normalised net tip resistance Qt, the friction ratio FR and the pore rpessure ratio Bq (section A, Appendix), soil classification has been obtained following the method proposed by Ramsey (2002). The net tip resistance q_{net} (section A, Appendix), was used to estimate the undrained shear strength (Su) and the preconsolidation pressure (σ'_p). σ'_p was later used to estimate overconsolidation and overpressure ratios (sections B and D, Appendix).

Site	Water depth (m)	Coordinates	Information	
KS14	789	E 000º 47.639' N 38º 38.613'	668 cm	Core length
KS16	672	E 000º 50.139' N 38º 38.219'	657 cm	
KS18	630	E 000º 50.453' N 38º 38.184'	765 cm	
PZ2-10	631	E 000º 50.466' N 38º 38.168'	4 hrs	Dissipation time
PZ2-11	670	E 000º 50.136' N 38º 38.228'	4 hrs	
PZ2-12	698	E 000º 49.944' N 38º 38.269'	2.3 hrs	

Table 5.4.2. Location of sediment cores KS14-KS16 -KS18 and piezometer readings at Pz2-10, Pz2-11 and Pz2-13 sites. Core lengths and dissipation times are also provided.

5.4.3.2. Piezometer

The IFREMER free-fall piezometre measures the dissipation of the pore pressure generated in response to the displacement of the sediments by the probe. It consists on a sediment-piercing lance of 60 mm in diameter attached to a recoverable instrument part. The rate of the pressure decay informs about the in situ pressures and sediment permeability. Pore pressures relative to hydrostatic are measured at five captors located at 0.5, 3.5, 5, 5.75 and 6.75 mbsf, with a resolution of about ±0.2 kPa.

5.4.3.3. Sediment cores

Three kullenberg piston cores KS14, KS16 and KS18 were collected at sites PFM05S1, PFM06S2 and PFM06S1, respectively (Fig. 5.4.2, Table 5.4.2), in order to characterize physical, geotechnical and sedimentological properties.

All cores were cut in one metre long sections after retrieval. Each section was logged using a Geotek multi-sensor core logging device, which provides gamma density (γ), P-wave velocity and magnetic susceptibility along the section. After core logging, selected sections of 5 and 25 cm were cut for oedometer and triaxial tests, respectively (Table 5.4.3). Where samples were taken for geotechnical tests, sedimentological and other descriptions are not available. Final core sections were visually described before laboratory tests and measurements. Archive core sections were analyzed onboard using an Avaatech XRF core scanner (Richter et al., 2006), which provided measurements of the elemental composition.

Onboard geotechnical laboratory measurements in working sections comprised water content (wc), vane shear tests, which provided peak and residual strengths, and P-wave attenuation measurements. Fall cone apparatus was also used for estimating the remoulded undrained shear strength Su and Atterberg limits at selected depths. Grain size analyses were conducted at the Univerity of Barcelona laboratory with a particle size analyzer Coulter LS 230 in samples were moisture content and shear vane measurements were done. Carbonate content were obtained using a Bernard calcimeter tool and total organic carbon (TOC) was measured by an elemental analyser LECO CS-125 at the CEFREM laboratory.

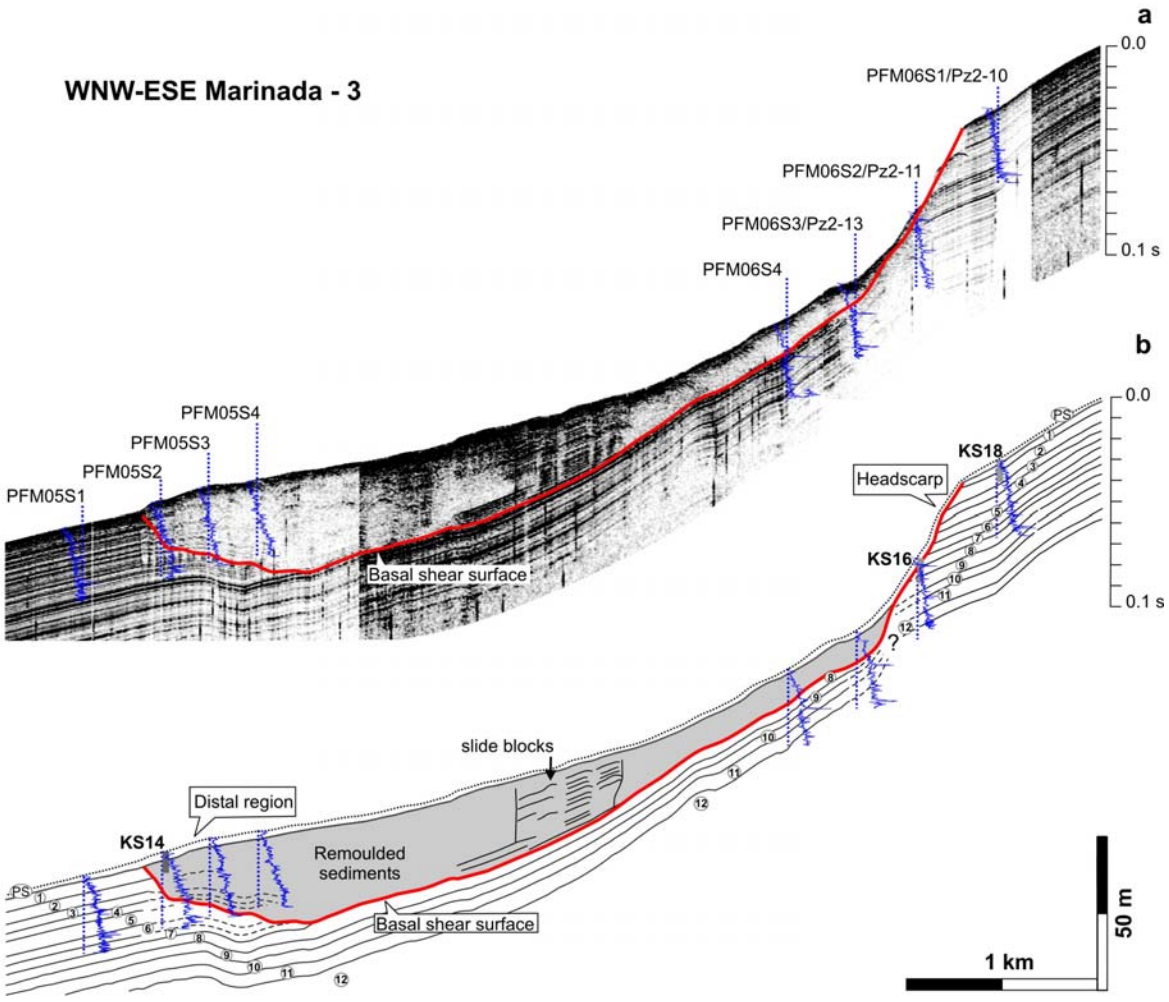

Figure 5.4.3. a: WNW-ESE Marinada-3 TOPAS profile (modified from Lastras et al., 2004) across the Ana slide showing correlation among CPTU profiles and seismic reflectors through the undisturbed sedimentary sequence at PFM06S1 and PFM05S01 sites and the basal shear surface; b: stratigraphic interpretation based on CPTU sites and seismic faces.

Consolidation tests were carried out by GEOMAR SL (Barcelona) laboratory in order to assess the stress history and consolidation characteristics. Derived preconsolidation stress (σ'_p) was determined following the Casagrande method (Craig, 2005). Intact values of the effective cohesion and effective friction angles of 13 kPa and 28º (6.54 mbsf, KS16) and 18.09 kPa and 30.6 º (4.92 mbsf, KS18) were determined from triaxial CU shearing tests made at confining pressures of 850 and 900 kPa by La Salle laboratory.

5.4.4. Results

Results from CPTU and piezometre data and laboratory analyses have allowed to characterize the undisturbed sedimentary sequence outside Ana slide boundaries and remoulded sediments within the slided mass. The investigated sedimentary sequence consists on 13 units (sediment drape, SD, and units 1-12) according to sediment changes inferred from CPTU profiles (Fig. 5.4.3b). Relevant sedimentological and geotechnical properties observed are described below.

5.4.4.1. Undisturbed sediments

CPTU soil classification at reference PFM06S1 and PFM05S1 sites informs about the presence of two types of clays:

- low sensitive clays (type 3), present in units SD, 1-4 and 8-12 and

- very sensitive clays in units 5-7, with sensitivity (St) values higher than 8 (type 1) (Fig. 5.4.4).

From laboratory analyses carried out in sediments samples in cores KS14-16-18 (Fig. 5.4.5) we infer that, at least, clay type 3 actually corresponds to carbonated (40-60% CaCO3) silty clays (62% of clays and 28% of silts) with very low total organic carbon (<0.5%). The sandy fraction (7-12%) consists of biogenic carbonated fragments. From sediment samples in unit 7 (Fig. 5.4.4, KS16 core) we assume that high sensitivity in sediment type 1 is due to relative coarser and unsorted sediment (inferred from sand and clay peaks) with lower content in clays (55%) and higher silts (30%) and sands (15%) (Fig. 5.4.5).

Plasticity varies from very high in post-slide unit (PS) and units 1 and 8 to intermediate in units 2 and 7 (Fig. 5.4.6). Water content (wc, 40-60%) tends to decrease with depth in all cores and Atterberg limits (liquid wl and plastic wp) range between wc values (Fig. 5.4.5). Gamma density (γ) profiles increase from 1.6 $g \cdot cm^{-3}$ at the upper sediment to ~2 $g \cdot cm^{-3}$ at core bases, and locally increases up to 1.96 $g \cdot cm^{-3}$ in units 7-8 (KS16 core) due to increased sand content.

Magnetic susceptibility varies substantially from one core to another and seems to be in agreement with sediment changes only in core KS18 (Fig. 5.4.5). From the various elements analysed by the XRF core-scanner (Al, Si, P, S, Cl, K, Ca, Ti, Mn, Fe, Rh), we found Fe counts to be the best in profiling the sediment drape's base between the three cores (Fig. 5.4.5). CU triaxial tests in KS18 core provided an effective friction angle of 30º and an effective cohesion of 18 kPa in unit 1 at 4.9 mbsf (Table 5.4.2).

Sedimentological and micropaleontological interpretation of COBAS cruise sediment cores (COBAS 44 and COBAS 42) obtained in the Ana slide suggests that the slide deposit is covered by an Holocene hemipelagic drape that includes an interval corresponding to the sapropel S1 of the Eastern Mediterranean (Cattaneo et al., submitted). These authors found a sedimentary hiatus between the Holocene drape and the underlying sediment. Moreover, they observed that at site of COBAS 44 core, which coincides with our PFM06S2/KS16 site, there is a slide surface without remoulded deposits on top, which is in agreement with our stratigraphic interpretation (Fig. 5.4.7).

We have considered the uppermost ^{14}C age between 40-41 cm (8931 yr calBP) in COBAS

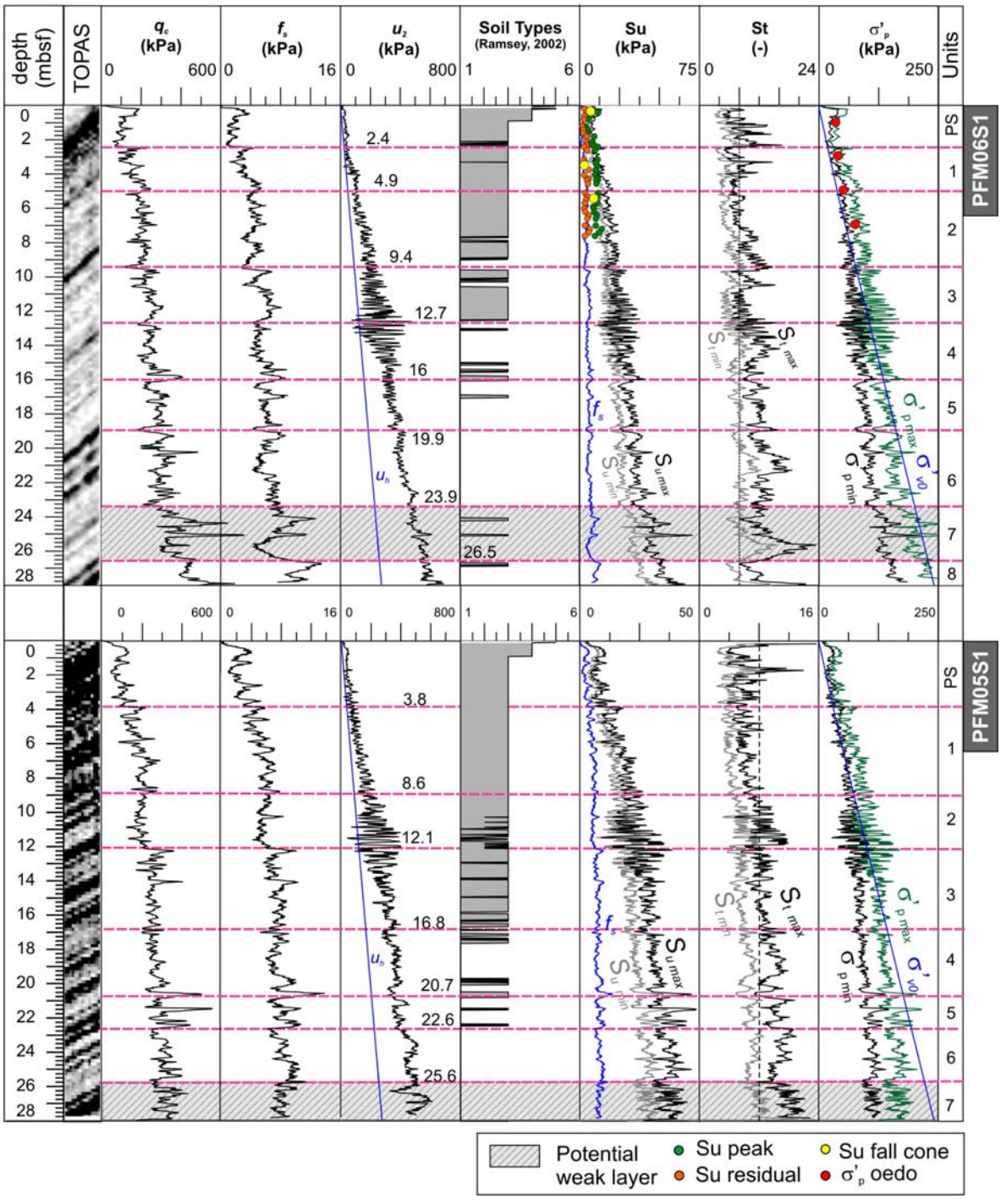

Figure 5.4.4. CPTU profiles in undisturbed sedimentary sequence at PFM06S1 and PFM05S01 sites. Red dashed lines indicate unit boundaries. PS, post-slide unit, q_c, cone tip resistance; f_s, sleeve friction; u_2, excess pore; u_h, hydrostatic pressure; Su, undrained shear strength; St, sensitivity; σ'_p, preconsolidation pressure; σ'_{v0}, vertical effective stress. Laboratory measures Su were obtained by a lab vane and a fall cone apparatus and σ'_p from oedometer tests (σ'_{pOEDO}). Grey fringe highlights the interpreted weak layer in unit 7.

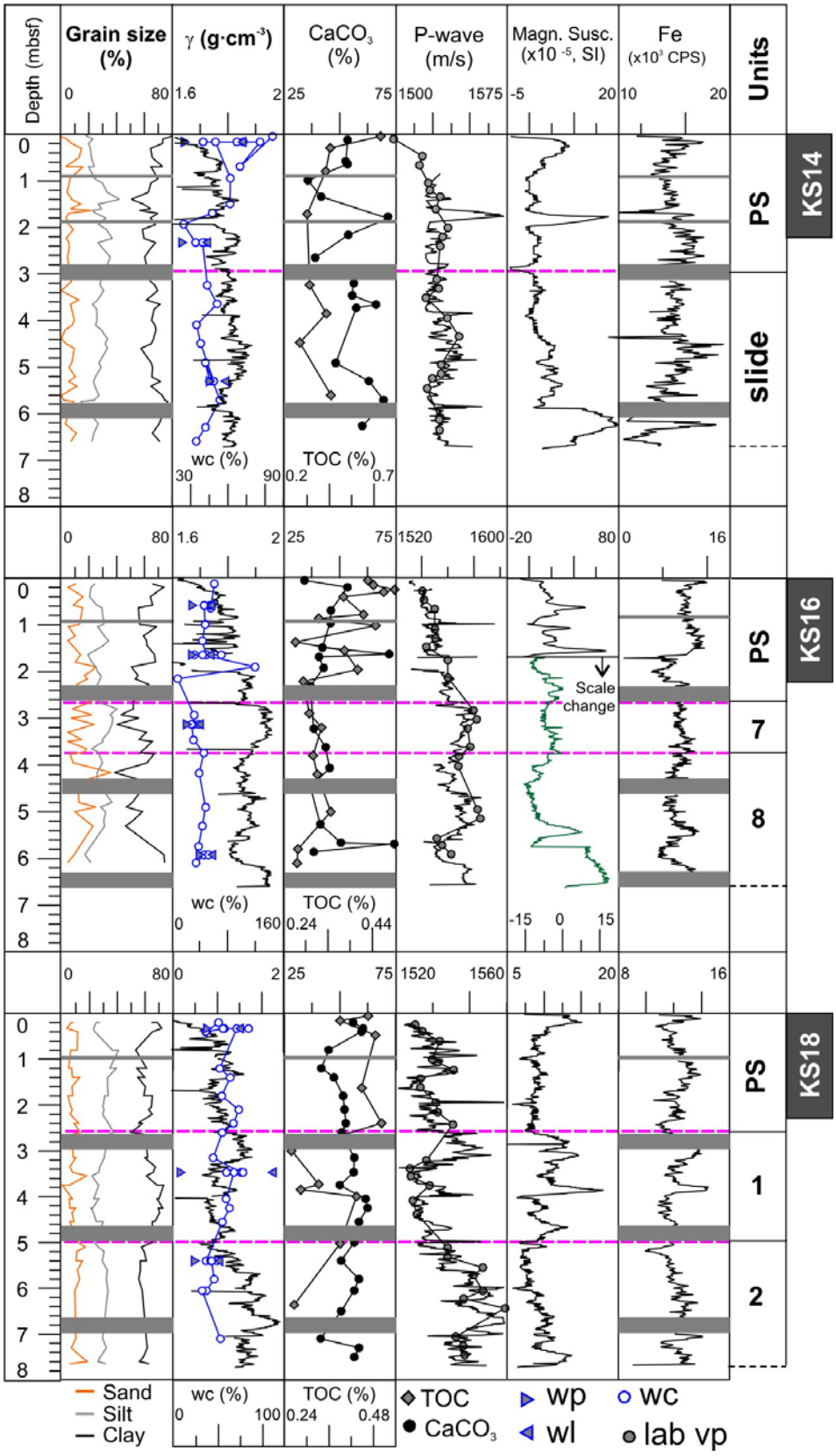

Figure 5.4.5. Grain size, gamma density (γ), water content (wc), Atterberg limits (liquid and plastic, wl and wp, respectively), carbonate content, total organic carbon (TOC), P-wave, magnetic susceptibility and elemental Fe measures carried out in sediment cores KS18, KS16 and KS14. Grey fringes correspond to sections used for oedometer and triaxial testing. PS corresponds to the post-slide unit.

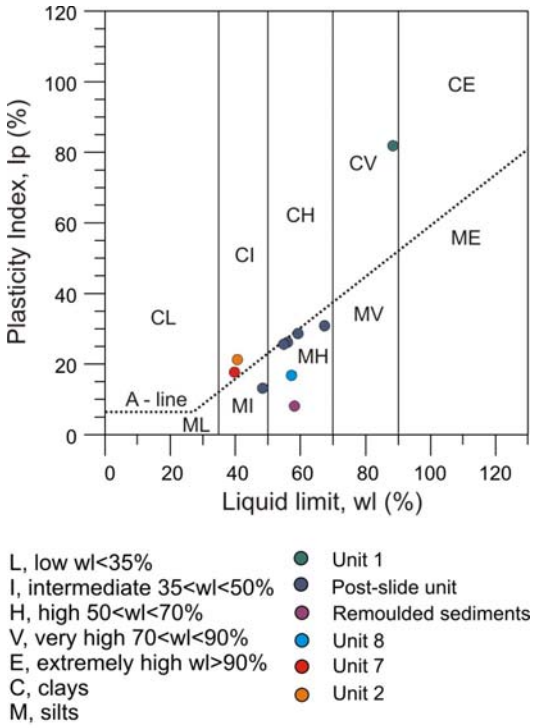

Figure 5.4.6. British soil classification of soils based on the plasticity index and the liquid limit (BS5930, 1999).

44 core to obtain an average sedimentation rate of 4.5 cm/kyr for the interval comprised between the seafloor and the base of our PS unit. This assumption provides an approximated age of 55.13 kyr cal BP for the base of our PS unit that we asume to be equivalent to the Ana's age.

5.4.4.2. Remoulded sediments

Remoulded sediments were sampled at core KS14 (Fig. 5.4.2). Deformation structures from 6.1 to 6.4 mbsf, the presence of clasts of dark sediment in lighter matrix, patches of silty sands with water escape and fluidified sediments at the core base were considered key indicators of remoulding (Fig. 5.4.8). Sediment facies identified in KS14 core consist on stratified sediments with shell debris with dewatering structures and darker coloured mud clasts of similar lithology in section S6 (380-481 cm), low degree disturbed sediments in section S7 (481-581 cm) and convolute zones, distorted sediments and fluidified sediments in section S8 that evidence plastic deformation. This distribution suggests a downward increase in the degree of sediment deformation.

5.4.4.3. Overconsolidation

The OCR has been studied from CPTU data (σ'_p), since lower σ'_{pOEDO} values (Fig. 5.4.9) suggest a certain degree of disturbance (Figs. 5.4.4 and 5.4.7). This has been confirmed after following the sample quality criteria established by Lunne et al. (2006) (section F, Appendix), which indicates a general poor quality for our samples (Table 5.4.3). A continuous profile of σ'_p was obtained following a constant $N_{\sigma t}$ equal to 5 (section B, Appendix).

The general trend delineated by the OCR profiles decreases more or less uniformly from OCR > 4 near the surface to lower values at greater depths (Figs. 5.4.10a and 5.4.10b). It appears that OCR = 1, typically related to normally consolidated sediments, has no significance for our data, since we observe that the depth of normal consolidation is transitional from overconsolidated to underconsolidated.

Table 5.4.4. Final section lengths of KS14-KS16-KS18 cores after sampling for geotechnical and sedimentological laboratory tests.

Sediment core	Core Section	Depth (cm)
KS14	S1	0-86
	S2	91-165
	S3	165-184
	S4	190-280
	S5	310-380
	S6	380-481
	S7	481-582
	S8	612-668
KS16	S1	0-89
	S2	94-166
	S3	166-230
	S4	260-360
	S5	360-430
	S6	460-560
	S7	560-627
KS18	S1	0-95
	S2	100-195
	S3	195-265
	S4	295-395
	S5	395-465
	S6	495-595
	S7	595-665
	S8	695-765

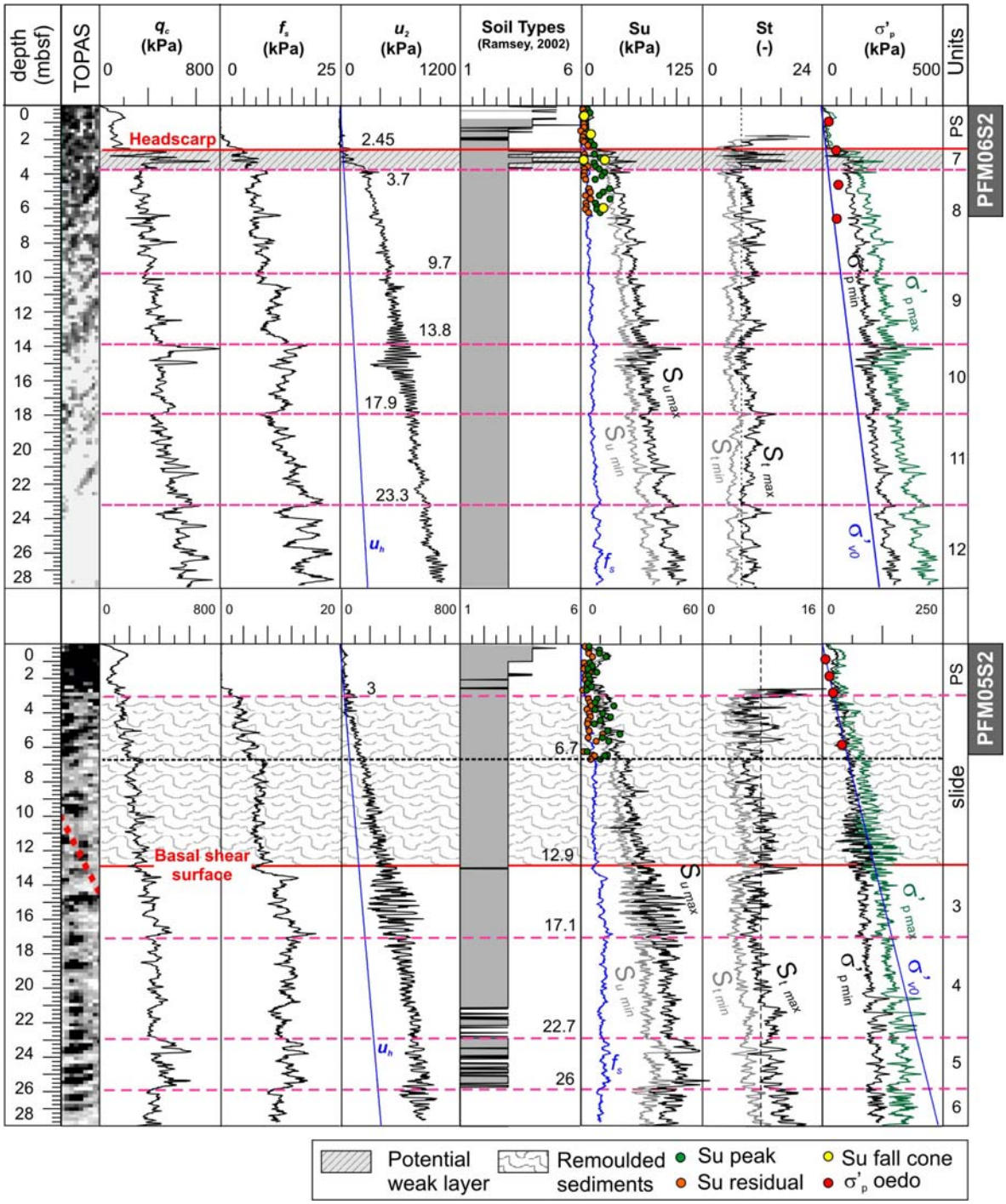

Figure 5.4.7. CPTU profiles in partially remoulded sequences at PFM06S2 and PFM05S2sites. See caption of Figure 5.4.4 for acronyms significance.

This transition of OCR=1 is found generally between 6.6-13.25 m except at PFM06S5 site, in which it is found at 4.7 mbsf (Fig. 5.4.10b). OCR > 4 at the first 1.2 mbsf at both distal and headscarp sites is related to the apparent (pseudo) overconsolidation that occurs in all surface marine sediments due to high inter-particle bonding and cementation (Silva and Jordan, 1984).

Below the apparent overconsolidation depth (1.2 mbsf), OCR > 4 below the shear surface in PFM06S2 (Brown line in Fig. 5.4.10b) corresponds to the removal of 9.5 m of

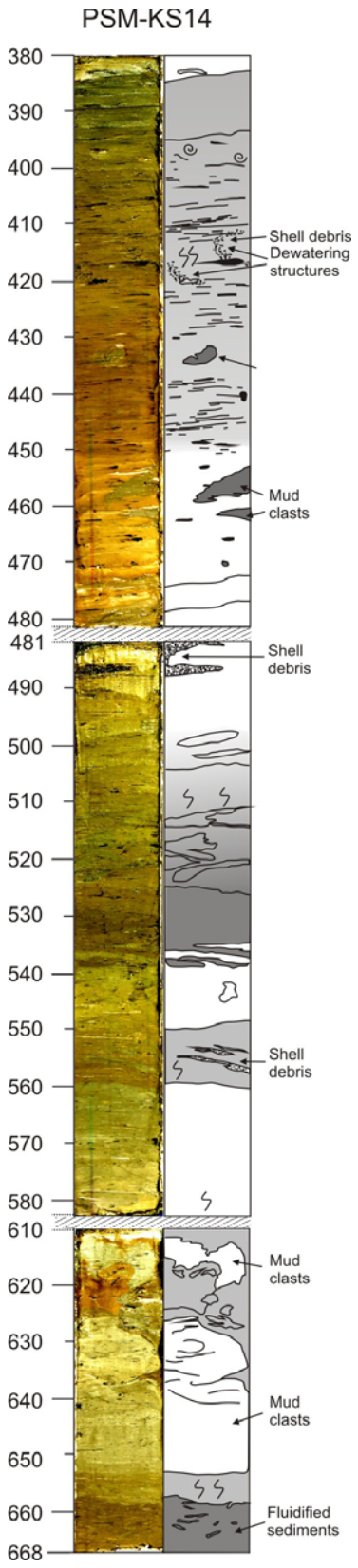

Figure 5.4.8. KS14 core photo showing depth increasing degree of deformation in the remolded sections S6-S7-S8. Colours where modified for interpreting structures and do not correspond to real colours.

sediment. Similarly, OCR > 1 peaks below the basal shear surface in PFM06S3, PFM06S4 and PFM06S5 sites informs about the removal of 11.5, 6.1 and 2.2 m of sediment, respectively (section C, Appendix). OCR > 2 within remoulded sediments in PFM06S3 and PFM06S5 sites (green and blue curves, respectively, in Fig. 5.4.10b) correspond to 3 and 2.3 m, respectively. Table 5.4.4. provides the corresponding depth intervals for the OCR peaks used in the erosion calculation.

5.4.4.4. Overpressure ratio

OCR < 1 informs about the existence of underconsolidated material, which means the existence of excess pore pressure (section D, Appendix) (Fig. 5.4.10). The ratio of overpressure (λ^*) at underconsolidated sites is shown in Figure 5.4.11 (section E, Appendix).

At site PFM06S1, λ^* is constant within values $0.3 < \lambda^* < 0.5$ whereas at sites PFM05S1 and PFM05S2, it increases with depth up to values > 0.5. In remoulded sediments, λ^* appears concentrated at the central part of the slide mass and it decreases down to values < 0.3 close to the slide base. At the headscarp area, remoulded sediments emerge locally overpressurized at PFM06S5 site with $\lambda^* > 0.6$ that increase with depth up to values 1. In contrast, at site PFM06S4, overpressure only appears below the shear surface with $\lambda^* < 0.3$. From this information

Site	Depth interval (m)	Mean OCR range	Mean erosion (m)	Sediment unit
PFM06S2	2.45-3.7	> 4	9.5	7
PFM06S3	3.1-4.2	> 2	3	Remoulded sediments
	11.16-11.36	> 1	11.5	8
PFM06S4	13.05-13.4	> 1	6.1	8
PFM06S5	1.8-2.4	> 2	2.3	Remoulded sediments
	10.8-11	> 1	2.2	8

Table 5.4.4. Values of headscarp erosion calculated from overconsolidationr atios (see section C, Appendix).

we assume that the overpressure is found slightly closer to the seafloor to the headscarp (Fig. 5.4.11). This is shown by overpressure ratios (λ^*) in unit 2 at reference sites PFM06S1 and PFM05S1 (Fig. 5.4.11). At both sites, λ^* increases up to 0.4 from unit 2 to 4. However, whereas at site PFM06S1 λ^* seems to remain constant (~0.4) from unit 4 down to unit 8, at PFM05S1 site λ^* increases with depth (0.3 to 0.6) from units 2 to 6.

Overpressure depicted by λ^* below the depth range of 6.6-13.25 mbsf (Fig. 5.4.11) is further supported by CPTU derived normalized undrained shear strengths (Su/σ'_{v0}) <0.25 (grey fringes in Fig. 5.4.11), which are attributed to underconsolidated sediments as proposed by Skempton (see in Terzaghi et al., 1996). As mentioned, underconsolidated sediments can be considered indicators of overpressurized sediments.

5.4.4.5. Pore pressure from piezometer

Figure 5.4.12 shows the dissipation of the pore pressure generated by the piezometer insertion. Since fully dissipation was not reached after 4h of readings, we obtained the in situ pore fluid pressure (u_0, also named equilibrium pore pressure) from the extrapolation of the final portion of the 1/t and 1/√t decay curves, according to Davis et al. (1991) and Flemings et al. (2008), respectively.

Extraplated u_0 values are lower than the hydrostatic and represent the 30 % of the effective stress at PFM06S1 (Pz2-10). In contrast, measures at PFM06S2 (Pz2-11) are lower than hydrostatic when following the 1/√t method and higher when following the 1/t. In general, both methods provide higher values of u_0 at PZ2-11 site (Table 5.4.3). In situ pore pressures following the 1/t extrapolation are lower than hydrostatic ones at sites PFM06S1 (PZ2-10) and PFM06S2 (PZ2-11). In contrast, from 1/√t method at pressure captors 2 and 3, u_0 are higher than hydrostatic. Taking into account that the 1/t method tends to overestimate the in situ pressure and 1/√t to underestimate (Flemings et al., 2008), we assume that at least, the upper 6.75 m of the Sedimentary sequence are characterized by in situ pressures equivalent to hydrostatic. This is further supported by the continuous P-wave profiles analyzed by the core logger and the laboratory P-wave attenuation measurements used onboard (Fig. 5.4.5)

5.4.5.Discussion

5.4.5.1. Current overpressure

We relate λ^* distribution with a higher (or more active) overpressure at the distal region. We relate lower λ^* values (0.1-0.3) at undisturbed units below the shear surface at PFM05S3 and PFM06S4 to overpressure reduction, i.e. dissipation, generated by the slide.

So far, the inexistence of overpressure at headscarp PFM06S2 and PFM06S3 sites characterized by sediment erosion (OCR > 1, Fig. 5.4.10) suggests that overpressure is locally dissipated. We relate overpressure dissipation to the local sediment removal at headscarp area.

Strong variations of u_2 are observed in all CPTU sites (blue curves, Fig. 5.4.11). We relate this particular u_2 signal to changes in CPTU filter saturation that could be due to:

(i) operational/technical error or, to some extend,

(ii) to the existence of gas bubbles within the sediment.

We assume that in the first case, if the signal was an artifact, it might have been more similar between different sites, namely having similar depth distribution and showing similar thickness.

Since we did not found any of these evidences and, moreover, we found the u_2

signal coincident with the apparition of overpressure (Fig. 5.4.11), we consider these signals to be related to gas bubbles. The existence of gas bubbles would be the explanation to account for the measured overpressure. These gas bubbles seem to be more scarce in sediment units 3-4 (PFM06S1 site) at headscarp areas; in unit 3 at PFM05S2 site and the base of unit 2 at PFM05S1.

5.4.5.2. Fluid escape evidences and preconditioning factors

The acoustic wipe-out observed from 1.02 to 1.06 s twtt in the seismic profile Marinada -3 (Fig. 5.4.3) (Lastras et al., 2004) seems to be connected to a gas source through a migration path that roughly coincides with the headscarp area of the older slide located underneath the Ana (Costa et al., 2009). Bright spots observed in 3D seismic reflection profiles suggest the existence of a deep discontinuous lens of gas-bearing sand (Costa et al., 2009) that could account for the observed overpressures.

The presence of methane at time of Ana slide formation has been inferred from $\delta^{13}C$ analysis in benthic foraminifera *Hyalinea balthica* and *Uvigerina peregrina* assemblages in core KS16, at site PFM06S2 (Panieri et al., 2009). Results show increasing $\delta^{13}C$ with depth, suggesting that gas seepage was active in the past, ca. 63 kyr BP. Continuous profiles of P-wave velocity in KS14-KS16-KS18 cores inform about non gas-saturated sediments in the upper meters of the sequence, according to Lee (2004). Therefore, we asume that upper sediments indicate that the studied sedimentary sequence was likely deposited under overpressure conditions due to gas release from a deep source. Such overpressure seems to have dissipated for the upper meters, likely in relation to the slide erosion.

The basal shear surface appears as a continuous horizon concordant with the underlying unit 8 (Fig. 5.4.3). We relate this to the existence of a mechanical discontinuity in which contrasted undrained shear strengths (Su) occur, with higher Su in unit 8 compared to 7 (Fig. 5.4.4). Higher sensitivity (St), with peak values higher than 16 means unit 7 has higher capacity of loosing strength and thus would indicate that unit 7 could have acted as a weak layer (Fig. 5.4.4). The contrast between low q_c values at the base of unit 6 and high q_c in the upper meter of unit 7 results in a decreased Su at this boundary further suggests the existence of another mechanical boundary atop of the weak layer. Furthermore, positive resistance peaks indicate a relative coarser grain size and likely relative higher permeability in unit 7, thus suggesting that gas seepage from deep sources would have been preferentially accumulated in this unit. Resulting reduced effective stress would increase the likelihood of unit 7 to lose its strength and fail.

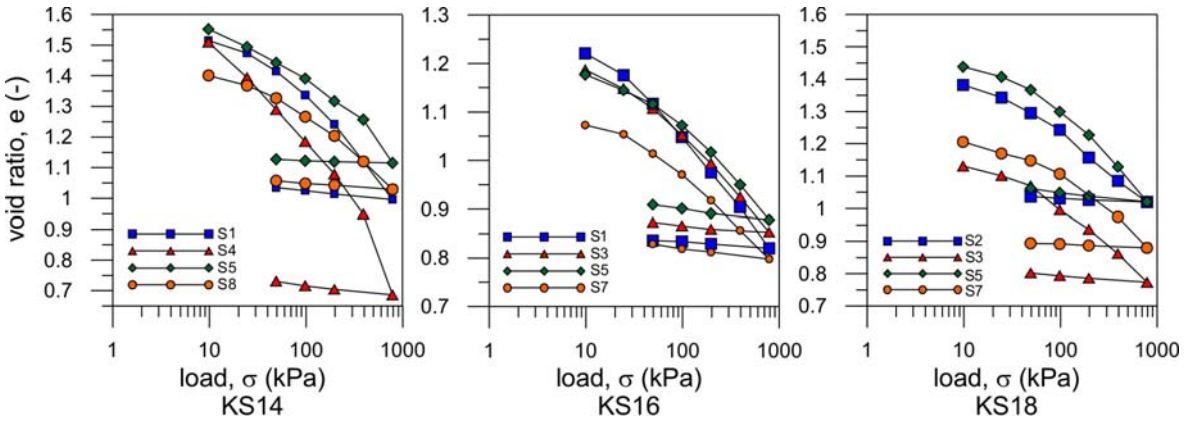

Figure 5.4.9. One-dimensional consolidation curves obtained from oedometer tests made in sections of KS14-KS16-KS18 cores. Corresponding depths for core sections are provided in Table 5.4.5.

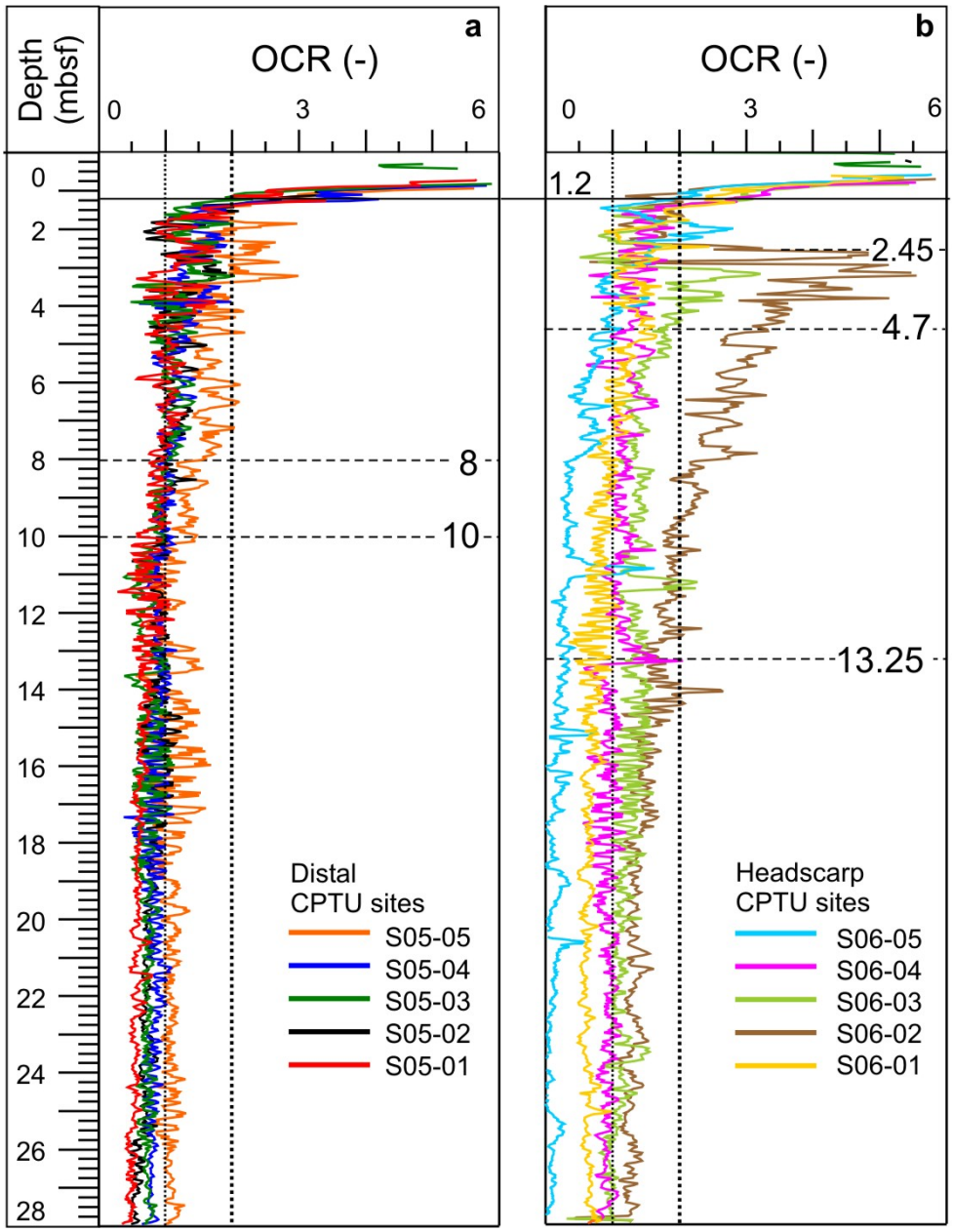

Figure 5.4.10. a: OCR profiles at distal sites showing the depth range (8-10 mbsf) in which overconsolidated sediments turn to underconsolidated and the interval in which OCR > 2 are related to equivalent erosion of 1 m. b: OCR profiles at headscarp sites. Transition from overconsolidated to underconsolidated sediments at PFM06S5 site occurs at 4.7 mbsf and at 13.25 at PFM06S4 site. Overconsolidated intervals at PFM06S5, PFM06S3 and PFM06S2 sites correspond to erosion values of 0.6, 3 and 9.6 m, respectively. Apparent overconsolidated sediments are found at the first 1.2 m in all sites.

5.4.5.3. Sources of overpressure

Due to the inexistence of permanent rivers on the Balearic Islands, rapid sedimentation cannot account for observed pore pressures in excess. Consequently, the absence of significative terrestrial sediment input results in the lack of organic matter to generate gasr. On the other hand, dissociation of hydrates during temperature or pressure changes, particularly during sea-level lowstands, could explain overpressure, as in glacial margins (Lee et al., 2007) but no bottom-simulating reflector is identifiable in seismic reflection profiles. Furthermore, western Mediterranean environmental conditions

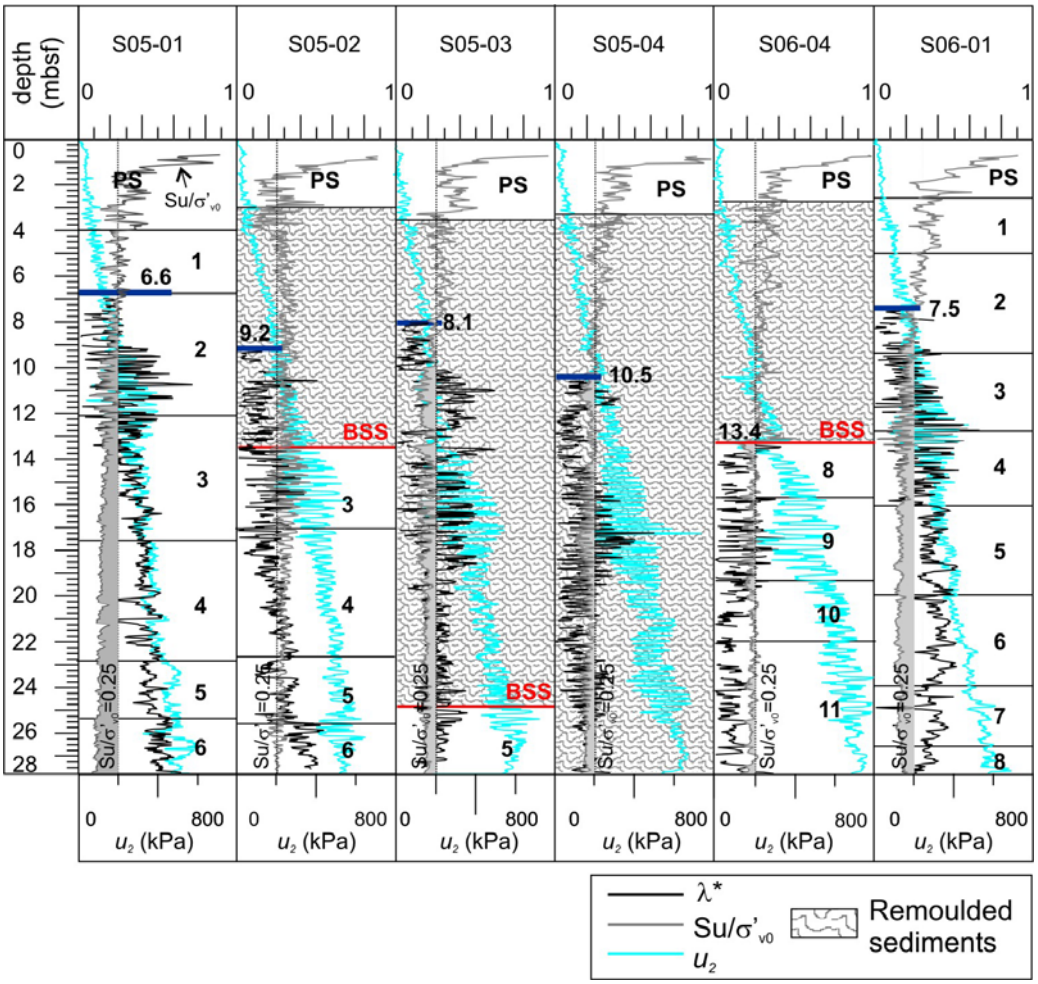

Figure 5.4.11. Overpressure ratio (λ*, black), excess pore pressure u_2 (blue) and normalised undrained shear strength < 0.25 (Su/σ'_{v0}, grey) profiles aligned through the Marinada-3 profile (location in Fig. 5.4.2). This correlation shows the agreement between the u_2 peaks associated to losses in saturation due to gas bubbles with underconsolidated sediments inferred from $Su/\sigma'_{v0} < 0.25$ (grey areas) and the estimated overpressure below the depth range of 6.6-13.25 mbsf. BSS, basal shear surface.

prevent their formation (Kvenvolden, 2000).

Another mechanism able to create overpressure is submarine groundwater discharge (SGD) (Hill, 2003; Burnett et al., 2006). Although examples of freshwater springs are generally found close to the coast, there are a few cases of seeps in quite distant sites off coast (e.g. >200 km at water depths of 600 m, Judd and Hovland, 2007). Based on the lack of clear evidences about the existence of significant SGD at Ana slide's location, we interpret our results in relation with gas charging caused by the expulsion of hydrothermal gases and water. Slide occurrence could be related to active faulting and associated activity related to thermogenic and/or hydrothermal settings, as suggested by Acosta et al. (2002, 2004).

Approximated age for Ana slide occurrence is ~ 55 kyr cal BP. This coincides with the end of the glacial MIS4. Low sea-level conditions at this time could have played a relevant role enhancing gas seepage because of reduced hydrostatic pressure building up pore pressure and consequently decreasing shear strength by dropping effective stress. Taking into account that this deep source of gas likely is the result of a general geological setting, at some extent, Nuna, Jersi and Joan slides, located further north, could have also

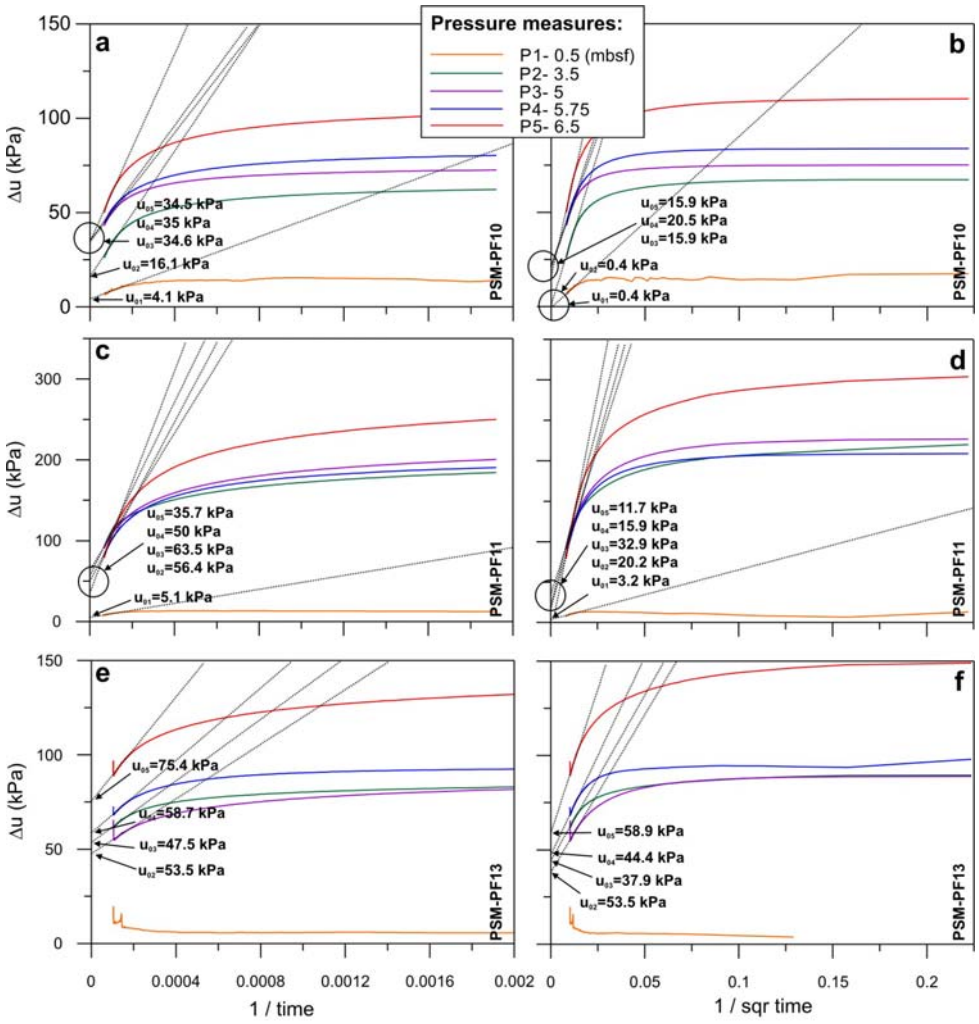

Figure 5.4.12. Piezometer curves at Pz2-10, Pz2-11 and Pz2-13 sites (location in Fig. 5.4.2) at pressure captors P1 to P5 at 0.5, 3.5, 5, 5.75, 6.75 mbsf, respectively. Equilibrium pressures (u_{0x}) are obtained from the extrapolation of the measured excess pore pressure Δu following the 1/time method of Davis et al. (1990) and the inverse of the square time following Flemings et al. (2008). Line colours correspond to colour pressure captors (see pressure measures at the top legend).

been triggered by gas charging related overpressures, according to their common slide plane (Lastras et al., 2004). Imprints of overpressures related to sea level changes have been found in sedimentary sequences of the upper slope in the Gulf of Lions, where overpressurized coarse grain-size layers were found to be linked to gas-exsolution processes during low sea level lowering (Lafuerza et al., 2009).

5.4.5.4. Geotechnical approach

If free gas exists, partial saturation in the sediments might be expected, If sediments are not fully saturated, calculation of vertical effective stress is not only dependent of hydrostatic pressure but also of soil saturation, since the existence of gas generates a matrix suction that decreases effective stress (Fredlund and Rajardjo, 1993). Consequently, the effective stress in the studied sediment could be lower than considered. However, marine clayey soils are characterized by very low matrix suctions

(capillary pressure) even for volumetric water content of 0.6 (60%) (Mitchell and Soga, 2005). Assuming that water saturation is higher than 60% in the Ana slide sediments (Fig. 5.4.5) we consider that capillary pressure can be neglected and that gas exists in the form of bubbles, from unit 3 up to 28 m at each site. Therefore, our sediment can be considered as fully saturated in terms of soil behaviour and thus, calculations of the effective stress properly hypothesized following hydrostatic conditions

5.4.6. Conclusions

CPTU profiles run in the Ana slide show the existence of current overpressures (with ratio between 0.3-0.4) within the undisturbed sedimentary sequence and remoulded sediments of the distal region. In contrast, headscarp CPTU sites show overconsolidated sediments related to slide erosion, which demonstrates that excess pore pressures were dissipated after sliding by overburden removal. We infer the presence of gas bubbles preferentially accumulated in unit 7, which is weaker than underlying unit 8 (sensitivity values >16), and is a preconditioning factor for sliding. According to the regional setting, gas charging of hydrothermal origin seems to be the most plausible explanation to account for the observed overpressure. Higher overpressures could have occurred at time of Ana slide event (55 kyr cal BP) by enhanced gas exsolution by low sea level conditions at the end of MIS 4.

Acknowledgements

We thank IFREMER team and crew of NO Atalante for its support during the PRISME 2007 cruise. This work has been founded by the CONSOLIDER 2010-GRACCIE project (Ref. CSD2007-00067), the HERMIONE project, EC contract no 226354-HERMIONE, funded by the European Commission's Seventh Framework Programme and a Generalitat de Catalunya grant for exellence research groups to GRC Geociencies Marines (Ref. 2009 SGR 1305). The publication reflects only the views of the authors; the EC is not liable for any use that may be made of this paper.

Appendix

A. CPTU derived parameters

$Q_t = (q_t-\sigma_v)/\sigma'_v$ [1]

$q_t = q_c+u_2\cdot(1-a)$ [2]

$q_{net} = (q_t-\sigma_v)$ [3]

$FR = (f_s/q_c) \cdot 100$ [4]

$Bq = (u_2-u_0)/(q_t-\sigma_v)$ [5]

where u_0 is the equilibrium pressure, σ_v the vertical effective stress, equal to $(z\cdot\gamma)$, σ'_v the vertical effective stress, $\sigma'_v = [(z\cdot\gamma))-(z\cdot\gamma w)]$, where z is depth, γ the total unit weight and γ_w the water unit weight.

B. Overconsolidation based on CPTU data

The relationship established between preconsolidation pressure (σ'_p) and the vertical effective stress σ'_v, namely the overconsolidation ratio (OCR), is expressed as follows:

$OCR = \sigma'_p / \sigma'_{v0}$ [6]

$\sigma'_p = (q_t - \sigma_{v0}) / N_{\sigma t}$ [7]

where σ'_{v0} is the effective vertical stress, σ_{v0} the total vertical stress, $N_{\sigma t}$ an adimensional cone factor.

Preconsolidation pressure and overconsolidation ratio (OCR) have been calculated following the constant value of 3.4 for the parameter $N_{\sigma t}$ following Demers and Leroueil (2002). Results obtained suggest 3.4 overestimates the OCR since it provides overconsolidated associated to erosion higher than the inferred from bathymetry description.

The lack of accurate laboratory σ'_p values does not allow to define a continuous profile of $N_{\sigma t}$ (see Lafuerza et al., 2009). Upper value of σ'_p following published range of 2-5 (Lunne et al., 1997) has proven to be the best in avoiding OCR overestimation and thus the most appropiate for estimating σ'_p.

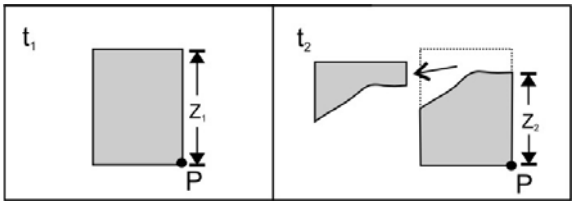

Figure C.1. Overburden removal in a point (P) buried at z_1 at initial time t_1 after sliding at t_2 in which burial becomes z_2. Eorsion would correspond to the difference between z_1 and z_2.

C. Erosion involved in the headscarp area

The effective stress (σ'_v) at point P (Fig. C.1):

$$\sigma'_v (t_i) = (\gamma_s \cdot z_i) - (\gamma_w \cdot z_i) \quad [8]$$

at t_1 σ'_v is maximum, i.e. $\sigma'_v = \sigma'_p$
σ'_p is the preconsoliation stress
at t_2 σ'_v is reduced by erosion (σ'_p = OCR/σ'_v)

After sliding (t_2):

$$z_1 \cdot (\gamma_s - \gamma_w) = OCR \cdot z_2 \cdot (\gamma_s - \gamma_w) \quad [9]$$
$$z_1 = OCR \cdot z_2 \quad [10]$$
$$\text{erosion (e)} = z_1 - z_2 = (OCR \cdot z_2) - z_2 \quad [7]$$
$$e = \Sigma n\, [(OCR \cdot z_2) - (z_2)] / n \quad [11]$$

D. Overpressure ratio based on CPTU data

$$\lambda^* = (\Delta u - u_h) / (\sigma_{vo} - u_h) \quad [12]$$
$$\Delta u = \sigma'_{v0} - \sigma'_p \quad [13]$$

where Δu is the excess pore pressure, u_h is the hydrostatic pressure and σ_{v0} the total vertical stress and σ'_p the preconsolidation pressure. We used σ'_p derived from CPTU data (section B, Appendix).

E. Piezometer interpretation

The interpretation of the in situ pressure from piezometer is often carried out through an empirical linear extrapolation based on the gradient of the last part of the data. Published works (Davis et al., 1991; Urgeles et al., 2000) suggest that 1/t extrapolation provides an accurate estimate of in situ pressure for sediments that dissipated the 90% of the initial pressure, whereas there are publications (Long et al., 2007) that suggest that 1/t overestimates u_0. In order to solve likely overestimations we have compared both methods: 1/t and 1/√t, according to Flemings et al. (2008).

F. Sample quality evaluation from oedometer curves

Lunne et al. (1997) evaluated which parameters were most systematically influenced by sample disturbance. The conclusion was that the change in pore volume relative to the initial pore volume $\Delta e/e_0$ was more systematically influenced. The proposed criteria quantified by the $\Delta e/e_0$ value are summarized in the following Table F.1. These criteria were established for marine clays with plasticity index 6-43%, water contents 20-67%, 1≤OCR≤4 and depths 0-25 mbsf. Data presented in this article is within these ranges.

	Sample quality category			
OCR	Very good to excellent	Good to fair	Poor	Very poor
1-2	<0.04	0.04-0.07	0.07-0.14	>0.14
2-4	<0.03	0.03-0.05	0.05-0.10	>0.10

Table F.1. Criteria for evaluation of simple disturbance as quantified by the value of $\Delta e/e_0$ (Lunne et al., 2006).

5.5. Climate and sea-level imprints of a Quaternary sedimentary succession of the Nile Deep Sea Fan from in situ and laboratory testing

S. Lafuerza (1), M. Canals (1), M. Galavazi (2)

(1) GRC Geociències Marines, Departament d'Estratigrafia, Paleontologia i Geociències Marines, Universitat de Barcelona, Spain
(2) Fugro Engineers B.V., The Netherlands

Abstract

Piezocone tests (CPTU), downhole natural gamma /neutron logs and laboratory measurements are used to characterize 192 m of Quaternary sediments drilled in the western province of the Nile Deep Sea Fan at 755 m water depth. The drilled succession is constituted by a lower hemipelagic sequence (LS), an intermediate sequence formed by stacked mass-wasting deposits (IS), and an overlying hemipelagic sequence (US). These sequences are formed by three different sediment types, A, B and C, which have been interpreted in terms of clay assemblages from literature sources. Based on climatic interpretation of the clay assemblages, we find the occurrence of mass-wasting deposits in the IS concurrent with a sea level lowstand related climate change characterized by aridity followed by an early sea level rise associated to more humid conditions.

Kew words: CPTU, downhole logs, laboratory tests, Nile Deep Sea Fan, mass-wasting deposits

Article per sotmetre a Geo-Marine Letters.

5.5.1. Introduction

The western province of the Nile Deep Sea Fan (NDSF) (Fig. 1a) is an emerging gas and condensate province (Dalla et al., 1997; Wigger et al., 1997; Badri et al., 2000; Abdel Aal et a., 2001; Vandré et al., 2007) characterized by abundant tectonically controlled fluid migration (Abdel Aal et al., 2001; Loncke et al., 2004 and 2006) and mass wasting processes (Neuwton et al., 2004; Mascle et al. 2006; Garziglia et al., 2008; Loncke et al., 2009). Slope instability configure this area as a geohazard scenario where numerous site characterizations and mitigation interventions have been carried out to reduce uncertainty, project time and costs for engineering designs (Evans et al., 2007; Moore et al., 2007).

The present work aims at relating sediment properties measured in a deep borehole drilled in the western province of the NDSF with climate and sea-level imprints. The drilled site records mass-wasting deposits embedded within two hemipelagic Plio-Quaternary sequences that are characterized after piezocone, natural gamma/neutron logs and laboratory data. Data were awarded by Fugro Engineers B.V. and British Petroleum (BP) to University of Barcelona in the frame of a joint research collaborative project.

5.5.2. Methods

In situ piezocone tests (CPTU), well logs and sediment coring were performed at site BH1 down to 192 mbsf. This site is 755 m water depth on the middle slope nearby the Rosetta canyon (Fig. 5.5.1a). The upper 78 meters of sediments are of Quaternary age according to AMS radiocarbon datings and optically stimulated luminescence (OSL) measurements at 26 and 42 mbsf (Fugro Limited, 2004, unpublished).

The parameters derived from CPTU data such as the undrained shear strength (Su, calculated from N_k equal to 15), the overconsolidation ratio (OCR = σ'_p/σ'_{v0}) obtained from the

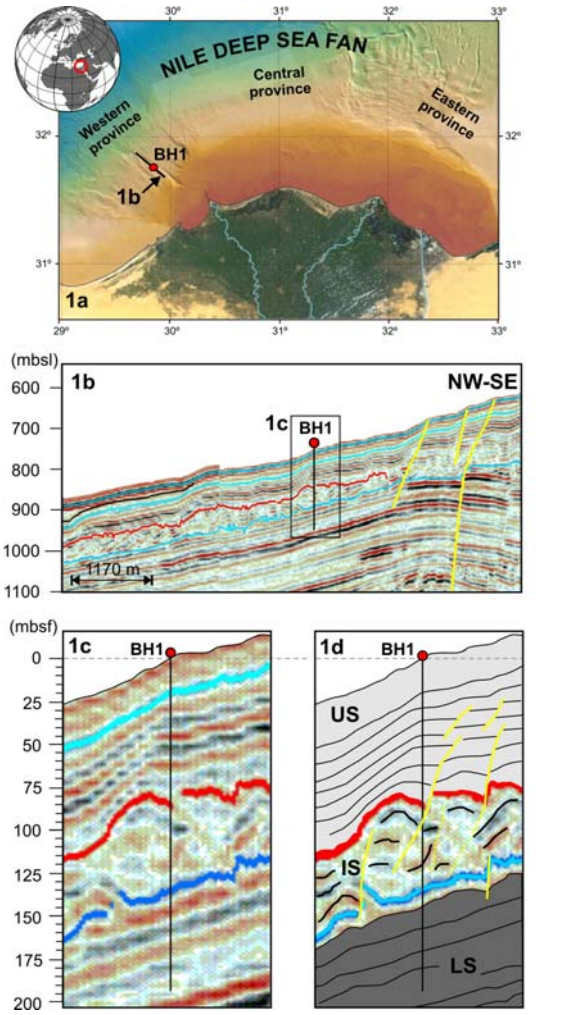

Figure 5.5.1. a, Location of borehole BH1 at 754.5 m water depth on the middle slope nearby the Rosetta canyon, in the western province of the Nile Deep Sea Fan; b, NW-SE seismic reflection profile crossing BH1; c, detail of seismic facies in BH1, d, main sedimentary sequences at BH1: lower sequence (LS), intermediate sequence made of stacked mass-wasting deposits (IS), and upper sequence (US).

preconsolidation pressure (σ'_p; from $N_{\sigma t}$ equal to 3.4) and the current vertical effective stress (σ'_{v0}) together with the normalized Su (Su/σ'_{v0}) have been considered to assess the stress history of the sediments and the identification of mechanical discontinuities. CPTU interpretation is described in detail in Lunne et al. (1997) and Lafuerza et al. (2009). Laboratory tests were carried out on selected sediment samples and consisted of grain size, water content (wc), Atterberg limits (wl, wp) and derived plasticity and liquidity indexes (Ip, Il), undrained shear strength (Su), precon-

solidation pressure (σ'_p) and organic matter (OM) and sulphate contents. Su values obtained by unconsolidated undrained triaxial (UU), fall cone (FC), lab vane (LV), torvane (TV) and pocket penetrometer (PP) tests are compared with continuous Su profiles calculated from in situ CPTU data. The plasticity index (Ip) was used to obtain a reference normalized Su profile for normally consolidated sediments following: $Su/\sigma'_{v0} = 0.0037 \cdot Ip + 0.11$ (Craig, 2005).

From well logging run in open and cased hole, we have utilised natural gamma (NG) and neutron logs run in-hole due to borehole instability. NG and neutron logs have been interpreted considering a boundary value of 20 CPS and dividing them into sections with neutron values higher or lower than 200 API-N, respectively (for further details, see Doveton, 1995).

5.5.3. Results and Discussion

The drilled succession is made of three main sequences: a lower hemipelagic sequence LS, from borehole bottom at 192 to 136 mbsf; an intermediate sequence formed by stacked mass-wasting deposits IS, 136 to 78 mbsf; and an overlying hemipelagic sequence US, 78 mbsf to borehole top (Figs. 5.5.1b-d). Changes in physical properties allowed subdividing each sequence into several units (Figs. 5.5.2 and 5.5.3).

5.5.3.1. Sediment types after well log data

The entire succession is constituted by three sediment types, named A, B and C, which have been established from NG and neutron logs (Fig. 5.5.2 and Table 5.5.1). Since the whole succession is clay-dominated (> 65%, Figs. 5.5.3a) and typical slope clayey sediments from the eastern Mediterranean have about 50-80% of smectite, 15-40% kaolinite and 0-15% illite (Venkatarathnam and Ryan, 1971), we assume that sediments types A, B and C are constituted by different proportions in these three clay minerals.

Sediment type	NG (CPS)	Neutron (API-N)
A	< 20	> 200
B	< 20	< 200
C	> 20	< 200

Table 5.5.1. Sediment types interpreted from natural gamma (NG) and neutron logs.

The Nile smectite is transformed into illite as burial progresses (Sandler and Herut, 2000). The product of this reaction is then a K-rich illite/smectite assemblage, which exhibits high levels of radioactivity. Hence, high natural gamma (NG) values should correspond to high K contents and, therefore, to higher proportions of transformed smectite, i.e. illite/smectite. Consequently, we consider that NG > 20 CPS in sediment type B is associated to relatively higher illite/smectite contents, while NG < 20 CPS in sediment types A and C corresponds to clays with higher content of non-transformed smectite (Fig. 5.5.2).

Following previous works on clay assemblages from the Nile (Stanley and Liyanage, 1986; Stanley and Wingerath, 1996), we infer that lower smectite contents in type A sediments correspond to a kaolinite-rich smectite assemblage, which is in agreement with low radioactivity depicted by NG < 20 CPS (Fig. 5.5.2).

The hydrogen index (HI) from neutron logs usually relates to the hydrogen content from porosity water, but it could also relate to hydrogen enclosed in clay's structure (Doveton, 1995). Although a general depth decreasing trend of neutron and water content is observed (Fig. 5.5.2), we attribute neutron log variations to the enclosed hydrogen in clays. Accordingly, > 200 API-N neutron values could be used to separate clay minerals with lower and higher hydrogen content. Since their swelling behaviour allows smectites to incorporate water molecules in their structure by increasing their volume, neutron values < 200 API-N in type B and C sediments (Fig. 5.5.2) are indicative of smectite dominance whereas neutron values > 200 API-N in type A correspond to smectite-depleted clays.

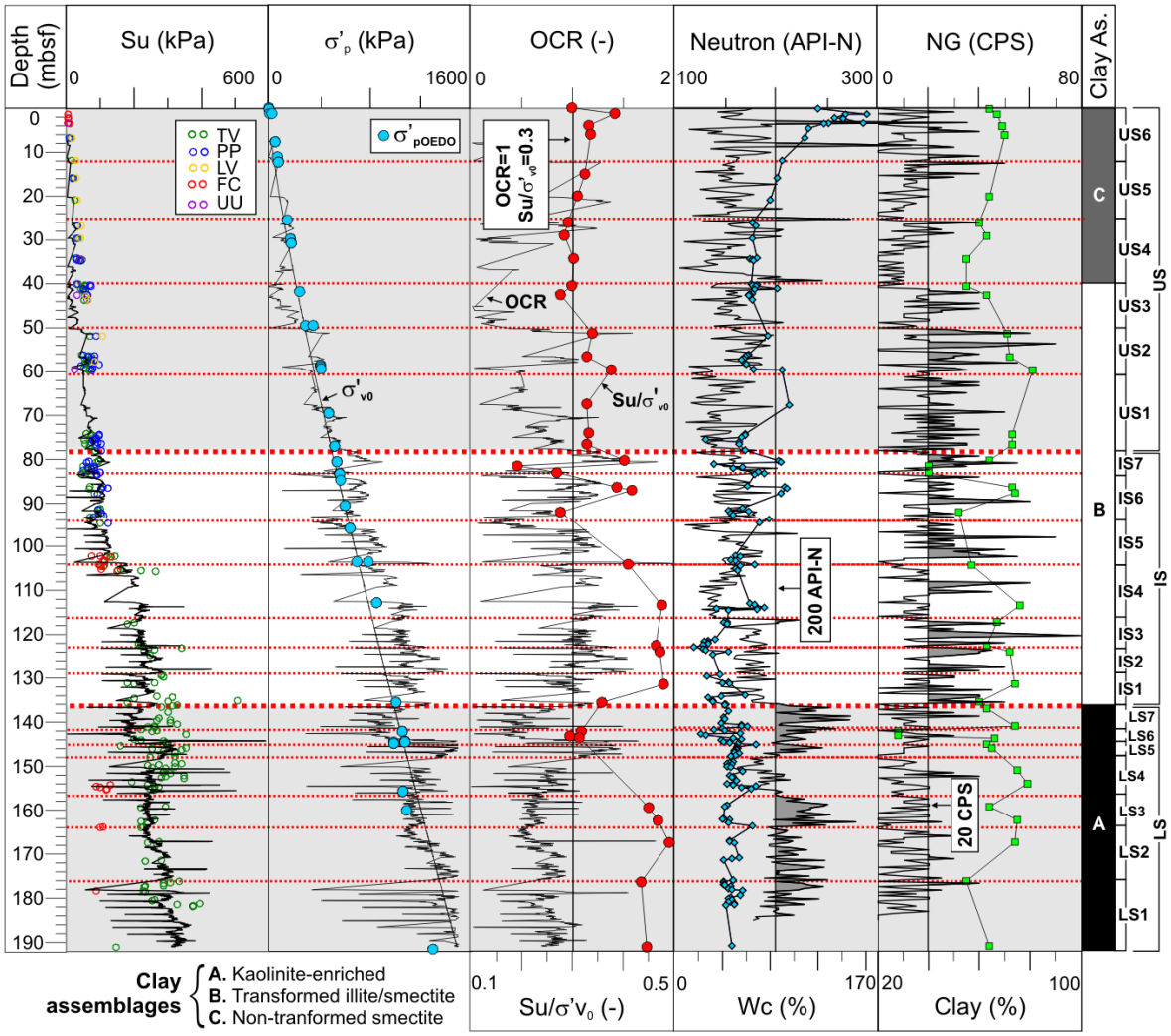

Figure 5.5.2. In situ measurements at BH1. Su has been estimated from a value of the parameter Nk equal to 15, which was considered the best approach for correlating with laboratory measurements of Su. Laboratory tests used for Su measurements are unconsolidated undrained triaxial test (UU), fall cone (FC), lab vane (LV), torvane (TV) and pocket penetrometer (PP). Preconsolidation pressure s'p versus effective stress σ'_{v0}. σ'_p values derived from CPTU data (σ'_{pCPTU}) are plotted with σ'_p measured from oedometer tests (σ'_{pOEDO}), thus providing the overconsolidation ratio (OCR). Normal consolidation is interpreted when OCR = 1; underconsolidation when OCR < 1 and overconsolidation when OCR > 1. OCR is compared to normalized Su (Su/σ'_{v0}), which is 0.3 in normally consolidated sediments. Water and clay contents are plotted together with the neutron and natural gamma profiles, respectively. Sequence boundary and unit subdivisions are depicted by red dotted lines. Clay assemblages and sequence's subunits are also indicated.

5.5.3.2. Geotechnical properties from CPTU and laboratory measurements

LS sediments are slightly underconsolidated with overconsolidation ratios (OCR) ~ 0.85 in units LS1 to LS4 and LS6-LS7, and slightly overconsolidated in LS5, with OCR ~ 1.3 (Fig. 5.5.2). Normalized undrained shear strength (Su/s'v0) is in opposition to OCR in LS (Fig. 5.5.2). OCR > 1 in LS5 likely corresponds to an apparent overconsolidation caused by high undrained shear strength (Su) and strong particle bonding due to abundant organic compounds as shown by OM > 3% (Fig. 5.5.3a), according to Kopf et al (1998). σ'_{v0} - σ'_p points to an excess pore pressure ~ 200 kPa that could account to relative low resistance in LS6-LS7 (Fig. 5.5.2). We relate underconsolidation ($\sigma'_p < \sigma'_{v0}$ and OCR < 1) in units LS1-LS4 and LS6-LS7 (Fig. 5.5.2) to excess pore pressure, according to similar results obtained in the Gulf of Lion (Lafuerza et al., 2009).

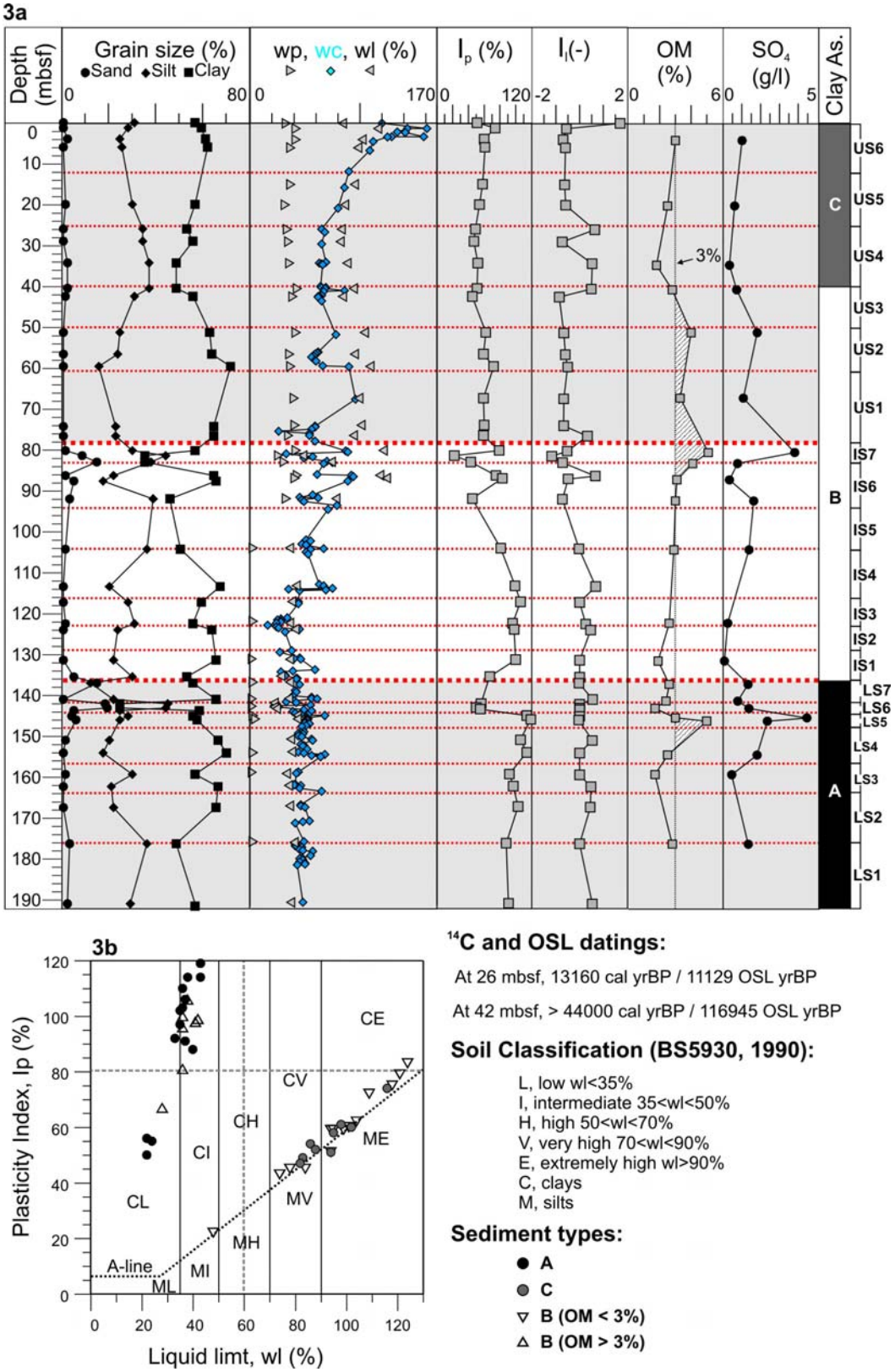

Figure 5.5.3. Laboratory-obtained sedimentary properties in BH1. 3a, Grain size, water content (wc) with plastic and liquid limits (wp and wl, respectively), plasticity and liquidity indexes (Ip and Il, respectively), organic matter content (OM) and sulphate content (SO4); sequence boundaries and unit subdivisions are depicted by dotted red lines, ^{14}C and OSL ages at 24 and 42 mbsf are indicated; 3b, BS5930 soil classification of the three sediment types in BH1 based on their liquid limit and plasticity index; the A-line represents the boundary between clays (above, C) and silts (below, M).

Overpressure is typically found in river dominated margins with high sediment input (Lee et al., 2007) as is the case for the Nile margin. A tentative sedimentation rate of 15cm·kyr^{-1} results from available range of radiocarbon/ OSL datings of 116945 and ~12000 yrBP at 42 and 26 mbsf, respectively (Fig. 5.5.3a-b), which is indicative of moderate sediment influx during the deposition of the upper sequence. Considering that the US is normally consolidated (Su/σ'_{v0} ~ 0.3, Fig. 5.5.2), we assume that higher sedimentation rates could prevail during the deposition of the generally underconsolidated LS.

However, overpressure in LS1-LS4 and LS6-LS7 can be also associated to gas charging as inferred from gas bubbles and expansive behaviour recognized during visual description of the sediment cores (Fugro Limited 2004, unpublished data). Based on our own data and also on recent publications from the study area (Garziglia et al., 2008; Loncke et al., 2009), both arguments are considered trustworthy.

IS sediments are slightly overconsolidated (OCR > 1) from unit IS1 to IS7 as demonstrated by general $\sigma'_p > \sigma'_{v0}$ and the dominance of $Su/\sigma'_{v0} > 0.3$ values (Fig. 5.5.2). Variable OCRs > 1 in IS (Fig. 5.5.2) are likely associated to variable degrees of erosion of the mass-wasting deposits. The OCR < 1 value above the boundary IS5-IS6 at 94 mbsf could be attributed to local overpressure related to fluid circulation through the fault identified at this depth (Fig. 5.5.1d). The consolidation state cannot be determined precisely in the upper sequence US due to discontinuous CPTU profiling (Fig. 5.5.2). Nevertheless, reference Su/ s'v0 values around 0.3 (red dots in OCR curve, Fig. 5.5.2) confirm normal consolidation.

Following BS5930 (1999) soil classification chart (Fig. 5.5.3b) we hypothesize that plasticity depends on sediment type and OM content. Smectitic clays in sediment type C display very high plasticity (CV-CE, Fig. 5.5.3b), whereas plasticity is reduced substantially in low smectitic clays, such as the kaolinite-enriched sediment type A (CL-CI, Fig. 5.5.3b). The plasticity of type B, is similar to sediment type A when OM < 3% and to C when OM > 3% (Fig. 5.5.3a). We attribute to the fault cutting the sedimentary succession at 94 mbsf (Fig. 5.5.1d) the plasticity contrasts between IS5 (OM < 3%) and IS7 (OM > 3%). This boundary also coincides with contrasted Su values (Fig. 5.5.3a). Similarly, the change from sediment type B to C at 40 mbsf (Fig. 5.5.2), which coincides with a shift from OM > 3% to OM < 3% (Fig. 5.5.3a) may involve a significant variation in the mechanical behaviour of the sediments at this depth. The most prominent mechanical discontinuity, located at 136 mbsf, is characterized by a decrease in Su and plasticity and an increase in sand content (5-23%, Fig. 5.5.3a), which coincides with the change from sediment type A to B. Therefore, (potential) mechanical discontinuities are most likely to appear associated to boundaries where changes in the sediment type and OM content generate plasticity contrasts.

5.5.3.3. Climate and sea-level imprints on sediment properties

Smectites in the Eastern Mediterranean result from increased fluvial erosion and terrigenous input during high rainfall periods (Cita et al., 1977). In contrast, kaolinite prevails during arid periods when aeolian transportation increases and rainfall weakens (Foucault and Mélières, 2000). Although kaolinite is globally considered a product of tropical weathering (Robert and Chamley, 1987; Bolle and Adatte, 2000), alternations of kaolinite and smectite in the Eastern Mediterranean are associated to arid and humid conditions, respectively (Hassold et al., 2003). Therefore, the changes from sediment type A to B and from B to C may represent a shift from drier to wetter environmental conditions in the Nile watershed.

According to Santiesteban et al. (2004), OM > 3% could correspond to ~1.5% content of organic carbon (Corg). Taking into account that sapropels in the Eastern Mediterranean developed during the time intervals with no

vertical mixing of the water masses due to enhanced fresh river input, and considering also that Corg contents in sapropel-bearing intervals from the Eastern Mediterranean Sea range from 2-12% (Kopf et al., 1998), we hypothesize that OM > 3% from IS6 to US3 correspond to wetter conditions and enhanced Nile runoff. These conditions prevailed during the upper mass-wasting period (unit IS6 and IS7) and the deposition of the overlying hemipelagic units US1 to US3. OM < 3% in type C sediments could represent the return to a lower Nile runoff.

Therefore, following Tzedakis (2007) it could be hypothesized that the accumulation of the lower hemipelagic sequence LS occurred during a relative low sea level period dominated by aridity in the Nile watershed and high sediment supply to the deep-sea fan (see previous sections). Wetter watershed conditions inferred from the properties of sediment type B suggest that the overlying sequence of mass-wasting deposits IS likely developed at the beginning of a sea-level rise and preceeding a period of enhanced Nile runoff, as interpreted from OM > 3% in the IS6-US3 interval (Fig. 5.5.3a).

5.5.4. Conclusions

Available geophysical and geotechnical data from a 192 m deep borehole drilled at 755 m of water depth in the western province of the Nile Deep Sea Fan have penetrated a thick sediment package made of stacked mass-wasting deposits embedded into two hemipelagic sequences. Natural gamma and neutron logs allowed to detect changes in the clay mineral composition of three sediment types, named A, B and C, considering the formation conditions and the distribution of smectite, kaolinite and illite in the Nile Cone from literature sources.

Comparison among clay assemblages in A, B and C and geotechnical properties obtained from CPTU and laboratory measurements reveal that sedimentary successions in river dominated areas with high organic matter input, such as the Nile margin, can lead to (potential) mechanical discontinuities at boundaries where changes in sediment type and organic matter content generate plasticity contrasts and decreases in undrained shear strength.

Furthermore, the climatic interpretation of Nile-sourced clays and significant changes in geotechnical properties, allow us to hypothesize that mass-wasting deposition occurred during a transition from lowstand to highstand conditions, but mostly during the early sea-level rise, coinciding with a shift from arid to more humid climate conditions. Unfortunately, the lack of a significant number of absolute datings precludes the establishment of a more precise chronostratigraphy.

Acknowledgements

This work has been possible thanks to Fugro Engineers B.V. and BP released the data here presented and allowed their publication. We thank E. Tervoort for his help and the technical staff from Fugro Engineers B.V. who contributed in different ways to this research. Foundings for UB researchers has been provided by the CONSOLIDER 2010-GRACCIE project (Ref. CSD2007-00067), the EU HERMIONE RTD project (Ref. 226354) and a Generalitat de Catalunya grant for exellence research groups to GRC Geociencies Marines (Ref. 2009 SGR 1305).